



Politecnico di Bari

Repository Istituzionale dei Prodotti della Ricerca del Politecnico di Bari

Quantum enabled wireless communication networks

This is a post print of the following article

Original Citation:

Quantum enabled wireless communication networks / Mushtaq, Muhammad Tauseef. - ELETTRONICO. - (2025).

Availability:

This version is available at <http://hdl.handle.net/11589/296380> since: 2026-01-27

Published version

DOI:

Publisher: Politecnico di Bari

Terms of use:

(Article begins on next page)



Politecnico
di Bari

DEPARTMENT OF ELECTRICAL AND INFORMATION
ENGINEERING
ELECTRICAL AND INFORMATION ENGINEERING
Ph.D. Program
SSD: ING-INF/03– Telecommunications
Final Dissertation

Quantum Enabled Wireless Communication Networks

by

MUSHTAQ MUHAMMAD TAUSEEF:

Supervisors:

Prof Nicola Cordeschi

Prof. Luigi Alfredo Grieco

Coordinator of Ph.D. Program:

Prof. Mario Carpentieri

Course n°38, 01/11/2022-31/10/2025



LIBERATORIA PER L'ARCHIVIAZIONE DELLA TESI DI DOTTORATO

Al Magnifico Rettore
del Politecnico di Bari

Il sottoscritto Mushtaq Muhammad Tauseef nato/a Jhelum, Pakistan il 01/04/1991 residente a Bari in via Giuseppe Fanelli 228/T e-mail tauseefghouri@gmail.com iscritto al 3° anno di Corso di Dottorato di Ricerca in Corso di Dottorato di Ricerca in Electrical and Information Engineering ciclo XVIII ed essendo stato ammesso a sostenere l'esame finale con la prevista discussione della tesi dal titolo:

Quantum Enabled Wireless Communication Networks
DICHIARA

- 1) di essere consapevole che, ai sensi del D.P.R. n. 445 del 28.12.2000, le dichiarazioni mendaci, la falsità negli atti e l'uso di atti falsi sono puniti ai sensi del codice penale e delle Leggi speciali in materia, e che nel caso ricorressero dette ipotesi, decade fin dall'inizio e senza necessità di nessuna formalità dai benefici conseguenti al provvedimento emanato sulla base di tali dichiarazioni;
- 2) di essere iscritto al Corso di Dottorato di ricerca Electrical and Information Engineering ciclo XVIII, corso attivato ai sensi del "Regolamento dei Corsi di Dottorato di ricerca del Politecnico di Bari", emanato con D.R. n.286 del 01.07.2013;
- 3) di essere pienamente a conoscenza delle disposizioni contenute nel predetto Regolamento in merito alla procedura di deposito, pubblicazione e autoarchiviazione della tesi di dottorato nell'Archivio Istituzionale ad accesso aperto alla letteratura scientifica;
- 4) di essere consapevole che attraverso l'autoarchiviazione delle tesi nell'Archivio Istituzionale ad accesso aperto alla letteratura scientifica del Politecnico di Bari (IRIS-POLIBA), l'Ateneo archiverà e renderà consultabile in rete (nel rispetto della Policy di Ateneo di cui al D.R. 642 del 13.11.2015) il testo completo della tesi di dottorato, fatta salva la possibilità di sottoscrizione di apposite licenze per le relative condizioni di utilizzo (di cui al sito <http://www.creativecommons.it/Licenze>), e fatte salve, altresì, le eventuali esigenze di "embargo", legate a strette considerazioni sulla tutelabilità e sfruttamento industriale/commerciale dei contenuti della tesi, da rappresentarsi mediante compilazione e sottoscrizione del modulo in calce (Richiesta di embargo);
- 5) che la tesi da depositare in IRIS-POLIBA, in formato digitale (PDF/A) sarà del tutto identica a quelle **consegnate**/inviata/da inviarsi ai componenti della commissione per l'esame finale e a qualsiasi altra copia depositata presso gli Uffici del Politecnico di Bari in forma cartacea o digitale, ovvero a quella da discutere in sede di esame finale, a quella da depositare, a cura dell'Ateneo, presso le Biblioteche Nazionali Centrali di Roma e Firenze e presso tutti gli Uffici competenti per legge al momento del deposito stesso, e che di conseguenza va esclusa qualsiasi responsabilità del Politecnico di Bari per quanto riguarda eventuali errori, imprecisioni o omissioni nei contenuti della tesi;
- 6) che il contenuto e l'organizzazione della tesi è opera originale realizzata dal sottoscritto e non compromette in alcun modo i diritti di terzi, ivi compresi quelli relativi alla sicurezza dei dati personali; che pertanto il Politecnico di Bari ed i suoi funzionari sono in ogni caso esenti da responsabilità di qualsivoglia natura: civile, amministrativa e penale e saranno dal sottoscritto tenuti indenni da qualsiasi richiesta o rivendicazione da parte di terzi;
- 7) che il contenuto della tesi non infrange in alcun modo il diritto d'Autore né gli obblighi connessi alla salvaguardia di diritti morali od economici di altri autori o di altri aventi diritto, sia per testi, immagini, foto, tabelle, o altre parti di cui la tesi è composta.

Luogo e data Bari, 27/10/2025

Firma _____

Il/La sottoscritto, con l'autoarchiviazione della propria tesi di dottorato nell'Archivio Istituzionale ad accesso aperto del Politecnico di Bari (POLIBA-IRIS), pur mantenendo su di essa tutti i diritti d'autore, morali ed economici, ai sensi della normativa vigente (Legge 633/1941 e ss.mm.ii.),

CONCEDE

- al Politecnico di Bari il permesso di trasferire l'opera su qualsiasi supporto e di convertirla in qualsiasi formato al fine di una corretta conservazione nel tempo. Il Politecnico di Bari garantisce che non verrà effettuata alcuna modifica al contenuto e alla struttura dell'opera.
- al Politecnico di Bari la possibilità di riprodurre l'opera in più di una copia per fini di sicurezza, back-up e conservazione.

Luogo e data Bari, 27/10/2025

Firma _____



Politecnico
di Bari

DEPARTMENT OF ELECTRICAL AND INFORMATION
ENGINEERING
ELECTRICAL AND INFORMATION ENGINEERING
Ph.D. Program
SSD: ING-INF/03– Telecommunications
Final Dissertation

Quantum Enabled Wireless Communication Networks

by

MUSHTAQ MUHAMMAD TAUSEEF:

Supervisors:

Prof Nicola Cordeschi

Prof. Luigi Alfredo Grieco

Coordinator of Ph.D. Program:

Prof. Mario Carpentieri

Course n°38, 01/11/2022-31/10/2025

POLITECNICO DI BARI

Abstract

Department of Electrical and Information Engineering

Doctor of Philosophy

Quantum Enabled Wireless Communication Networks

by Muhammad Tauseef MUSHTAQ

Efficient resource allocation to enhance network performance for ultra-reliable and low-latency type communication (URLLC) is a major consideration since the development of the Internet of Things. Recent advancements, especially in Massive Machine Type Communication (mMTC), now demand goal-oriented data delivery. Coupled with those mentioned earlier, goal-oriented communication dictates a data-driven approach to meet the current demands. In addition to classical communication, quantum communication also requires low latency and efficient resource allocation since memory decoherence and fidelity remain feasible for shorter periods. Therefore, this work proposes two Reinforcement Learning-based strategies to meet the requirements of each type of network.

Contents

List of Figures	xii
List of Tables	xiii
Scientific Contributions	1
Introduction to Classical and Quantum Networks	3
0.1 Wireless Powered Sensor Networks for mMTC	3
0.2 The Quantum Internet	3
0.3 Thesis Contribution	3
0.4 Thesis Organization	3
1 Introduction to applications of RL on massive and long haul connectivity	5
1.1 PD-NOMA and Goal Oriented Communication	8
1.2 Global Quantum Internet	8
1.3 Thesis Contributions	11
2 Distributed Q-Learning for Age of Information Optimization	17
2.1 Introduction	17
2.2 System Model	19
2.2.1 Network Deployment	19
2.2.2 Channel Model and CSI-aware PD-NOMA	20
2.2.3 κ -Factor-aware Discrete Channel grading	21
2.2.4 Energy Harvesting Model	22
2.2.5 Age of Information	23
2.3 Markov Decision Process Formulation	24
2.3.1 Optimization Problem Formulation	25
2.4 PD-NOMA SIC with REARLY-K slot-wise decoding	26
2.4.1 Slot-wise (REARLY- k) decoding with immediate inter-slot IC	26
2.5 Results and Discussion	26
3 A PPO-Based PD-NOMA Scheduling Methodology for Age of Information Minimization	33
3.1 Introduction	33
3.2 System Model	34
3.2.1 Energy Harvesting Model	38
3.2.2 Age of Information	39
3.3 Partially Observable Markov Decision Process	39
3.3.1 Proximal Policy Optimization (PPO)	41
3.4 Numerical Results	42

4	Maximizing Entanglement Rate with Latency Constraint for Global Quantum Internet using LEO Satellites	47
4.1	Introduction	47
4.2	BACKGROUND	49
4.2.1	Entanglement Generation	49
4.2.2	Entanglement Swapping	52
4.2.3	Noise	53
4.2.4	Fidelity Management and Purification-Swapping Model	55
4.2.5	Assumptions	57
4.3	SYSTEM MODEL	59
4.3.1	Latency Considerations	62
4.4	Segment-Aware Entanglement Distribution Protocol	64
4.4.1	Segment-Aware Method Description	66
4.5	Protocol Design Insights	67
4.5.1	Link-Level Fidelity After Purification	68
4.5.2	Purification Success Probability and Generation Requirements	68
4.5.3	Cumulative End-to-End Success Probability	68
4.6	System Model and Problem Formulation	69
4.6.1	Geometric and Channel Model	69
4.6.2	Entanglement Generation and Swapping	69
4.6.3	Markov Decision Process Definition	70
4.6.4	Optimization Objective	71
4.6.5	Discussion	71
4.7	Scheduling Implications	71
4.8	Flow of PPO-Based Entanglement Scheduling	71
4.9	Results and Discussion	72
	Conclusions and Future Works	77
	Bibliography	78

List of Figures

1.1	IRSA and Multi Packet Reception (MPR)	7
1.2	PD-NOMA as Multi Packet Reception for access enhancement	9
1.3	Idea of Channel, and Energy Efficient Decision making in resource access for massive access	10
2.1	Bipartite Representation of SIC process with PD-NOMA	19
2.2	Frame Structure of IRSA with Energy Harvesting	20
2.3	Average Reward per Episode for Power Level $M = 10, k = \{2, 3, 4, 5\}$	28
2.4	Average energy consumption convergence towards optimal as the frames I progress, $N = 5, M = 10$	28
2.5	Average \bar{A} when total number of power levels $K \{2, 3, 4, 5\}$	29
2.6	Average energy consumption with power levels $N = 5, k = \{2, 3, 4, 5\}$	29
2.7	Comaprison of EE-IL with random access and energy-based greedy algorithm.	30
2.8	Optimal Replica Access Probabilities for $M = 10, k = 2, 3, 4, 5$	30
2.9	Optimal Replica Access Probabilities for $M = 12, k = 2, 3, 4, 5$	31
2.10	Optimal Replica Access Probabilities for $M = 15, k = 2, 3, 4, 5$	31
2.11	PD-NOMA independent-learner Q-learning: state \rightarrow masked action (ℓ, k) \rightarrow SIC & AoI update \rightarrow reward & Q-update; loop over time horizon.	32
3.1	Caption	33
3.2	Frame structure of slot-based scheduling	34
3.3	AoI evolution with scheduling	35
3.4	Energy harvesting and usage	35
3.5	Reward convergence vs. episodes, $N = 15, \gamma_{th} = -5$ dB.	43
3.6	Average AoI vs. $M, N = 15, \gamma_{th} = -5$ dB.	44
3.7	Average AoI vs. $\gamma_{th}, M = 60, N = 15$	44
3.8	Example of policy converging to greedy strategy under good conditions with $\gamma_{th} = -20$ dB	45
4.1	Schematic representation of the ebit distribution protocol.	50
4.2	Schematic representation of the parallel swapping proecess.	52
4.3	(a) Resulting fidelity vs. purification rounds. (b) Purification success probability vs. initial fidelity.	56
4.4	Quantum Intra-Subnetwork	59
4.5	Segment-aware HQIN protocol. Phase 1: entanglement generation and path selection. Phase 2: fidelity-latency trade-off evaluation and purification. Phase 3: entanglement swapping to establish end-to-end entanglement.	65
4.6	Slant range $d(\beta(t))$ with respect to the elevation angle, zenith angle $\theta(t)$, and local horizon at a Quantum Ground Station (QGS) for satellite-based entanglement distribution.	70
4.7	PPO update is triggered <i>only</i> when the rollout buffer reaches a threshold; per-step Experience is always accumulated, independent of the target/window condition.	73

4.8	Sum of Rewards when a single source target pair request	74
4.9	Sum of Rewards when a single source target pair request	74
4.10	Sum of Rewards for multiple source pair requests for the schedule	74
4.11	Sum of Rewards for multiple source pair requests for the schedule	75
4.12	Reward for scheduled satellite's angles	75

List of Tables

1.1	Review of Related Works	12
1.2	Summary of Related Works on Scheduling for AoI minimization	13
1.3	Review of Related Works (PD–NOMA / IRSA / ALOHA, AoI-centric)	14
1.4	State of the Art and Their Contributions	15
2.1	Symbol Notation	18
2.2	Simulation Parameters	27
3.1	Simulation and Training Parameters	43
4.1	Abbreviations	49
4.2	Notation Summary	60

Scientific Contributions

All the scientific contributions produced during the doctoral course are listed below.

International Conferences:

- c1 M. T. Mushtaq, N. Cordeschi, G. Boggia, L. A. Grieco, "Optimized Scheduling of Packets with Deep Sensing Irregular Slotted Aloha Influenced by Channel Knowledge for Wireless-Powered IoT Networks", September 2023, IEEE International Conference on Information and Communication Technologies for Disaster Management. (Best Paper Award)
- c2 M. T. Mushtaq, Veronico Giuseppe, N. Cordeschi, G. Boggia, L. A. Grieco, "Simultaneous WET and WIT with Q-learning for wireless bridge sensors network", June 2024, IABMAS 2024, Copenhagen, Denmark.
- c3 Pohudina, O., Tauseef, M.M., Sivo, A., Cordeschi, N., Grieco, L.A. (2025), "Localization of Things Simulation in Smart Warehouses Applications Based on UWB Technology" In: Lytvynov, O., Pavlikov, V., Krytskyi, D. (eds) Integrated Computer Technologies in Mechanical Engineering - 2024. ICTM 2024, Springer, Cham.

Under Review:

- c4 M. T. Mushtaq, N. Cordeschi, G. Boggia, L. A. Grieco, "A PPO-Based PD-NOMA Scheduling Methodology for Age of Information Minimization", Submitted to IEEE ICC 2026.

Introduction to Classical and Quantum Networks

- 0.1 Wireless Powered Sensor Networks for massive Machine-Type Communication (mMTC)**
- 0.2 The Quantum Internet**
- 0.3 Thesis Contribution**
- 0.4 Thesis Organization**

Chapter 1

Introduction to applications of Reinforcement Learning (RL) on massive and long haul connectivity

The proliferation of Internet of Things (IoT) and mMTC networks has intensified the demand for scalable, energy-efficient wireless communication. In such systems, a central Access Point (AP) must reliably and promptly collect data from numerous low-power Machine-Type Communication Device (MTCD), all while minimizing computational overhead and supporting green, goal-oriented communication [1]. These requirements are particularly stringent in dynamic environments such as medical monitoring, industrial digital twins, and Vehicular-to-everything (V2X) applications [2], which align with the 6G vision of ultra-reliable, low-latency, massive connectivity [3].

Efficient Medium Access Control (MAC) is a central challenge in such dense deployments, where multiple MTCD contend for shared wireless resources. Random access protocols, especially slotted ALOHA variants like Irregular Repetition Slotted ALOHA (IRSA), are favored for their simplicity and scalability. By combining multi-replica transmissions with Successive Interference Cancellation (SIC), IRSA achieves notable throughput gains [4]. However, most existing IRSA-based schemes overlook data freshness and assume ideal energy availability, thereby limiting their relevance in energy-constrained IoT scenarios. Figure 1.1 shows the evolution of IRSA as the access strategy to maximize the connectivity.

The literature on massive IoT and mMTC connectivity can be broadly categorized into two access paradigms: scheduling-based and random access. Scheduling-based techniques such as Time Division Multiple Access (TDMA) [5] and Frequency Division Multiple Access (FDMA) [6] offer deterministic coordination but are limited in scalability under dense deployments. In contrast, random access protocols, including Coded Slotted Aloha (CSA) [7] and IRSA [4], enable scalable, contention-based communication. IRSA, in particular, exploits multi-replica transmission and SIC to enhance decoding performance. Significant enhancements to IRSA have been proposed through the integration of energy-awareness [8], [9], [10], [11], feedback mechanisms [8], [12], and Channel State Information (CSI)-aware decision-making [13], [14]. Parallel to IRSA developments, Non-Orthogonal Multiple Access (NOMA), especially Power Domain Non-Orthogonal Multiple Access (PD-NOMA), has been explored for its potential to support ultra-dense mMTC scenarios [15], [16], [17], [18], [19]. In PD-NOMA, transmission power is assigned based on CSI to satisfy Signal-to-Interference-plus-Noise Ratio (SINR) constraints [18], while maintaining a random access pattern. Beyond protocol design, recent efforts focus on optimizing traffic load and degree distributions for improved throughput and energy efficiency, particularly in Energy Harvesting (EH)-enabled settings. These include both analytical approaches [17] and model-free RL methods capable of operating under partial observability and stochastic energy arrivals [5], [20], [21], [22], [23]. In addition to classical metrics such as throughput and energy efficiency, recent studies have emphasized information-centric metrics. These include Age of Information (AoI) [24], Age

of Incorrect Information (AoII) [25], Value of Information (VoI) [5], and Query Version Age of Information (QVAOI) [26], which better capture information freshness, accuracy, and context relevance. In this context, open issues come from recent CSI-based schemes [13], [14] that employ thresholding to exclude devices experiencing poor channel conditions, thereby improving average throughput but potentially worsening AoI due to deferred transmissions from suppressed devices.

Table 1.1 summarizes the representative works across various criteria: access schemes, performance metrics, energy models, and algorithmic strategies. Key contributions are reviewed below.

- *IRSA-based approaches*: numerous works have extended IRSA to accommodate EH and maximize performance. For example, [20] combines RL with IRSA under AP-assisted EH, while [7], [8] investigate ambient EH with closed-form access strategies. These studies improve throughput and energy use but often overlook timeliness metrics such as AoI.
- *ALOHA and scheduling-based access*: slotted ALOHA under EH constraints has been explored in [10], [11], [18], [25], [27], [28], with some works targeting AoII minimization. Structured access methods, including scheduling and decision-theoretic control, are presented in [5], [22], [23], [29]. Notably, [5] proposes an Markov Decision Process (MDP)-based policy that optimizes VoI, and [23] addresses AoI-aware access under EH using constrained MDPs.
- *AoI and AoII optimization*: timeliness-focused access control is examined in [24], [30], where degree optimization in IRSA minimizes AoI. Extensions to AoII are explored in [11], [25] through analytical and MDP frameworks. However, most of these works either assume ideal channels or do not account for capture-aware decoding in IRSA.
- *Learning with EH*: learning-based solutions tailored to EH environments appear in [20], [21], [31]. For instance, [21] develops a fast Q-learning approach for IRSA, while [31] derives analytical slot access policies for EH-ALOHA. Despite their strengths, these works generally neglect information freshness and channel effects.

Although prior studies have advanced IRSA, AoI, and EH-aware access, few frameworks address these jointly with realistic assumptions, such as nonlinear energy harvesting, finite battery capacity, fading channels, and capture effects. Table 1.1 provides the summary for scheduling and random access-based strategies adopted to maximize connectivity and enable goal-oriented communication. Notably, CSI-based access control in [13], [14] halts transmissions from low-CSI devices entirely, which can inadvertently increase AoI. Our proposed approach instead integrates both CSI and battery state into a unified access strategy that dynamically adjusts replica counts without excluding devices. Moreover, the interplay between centralized and decentralized RL-based access under realistic mMTC conditions remains an open problem, which we aim to address in this work.

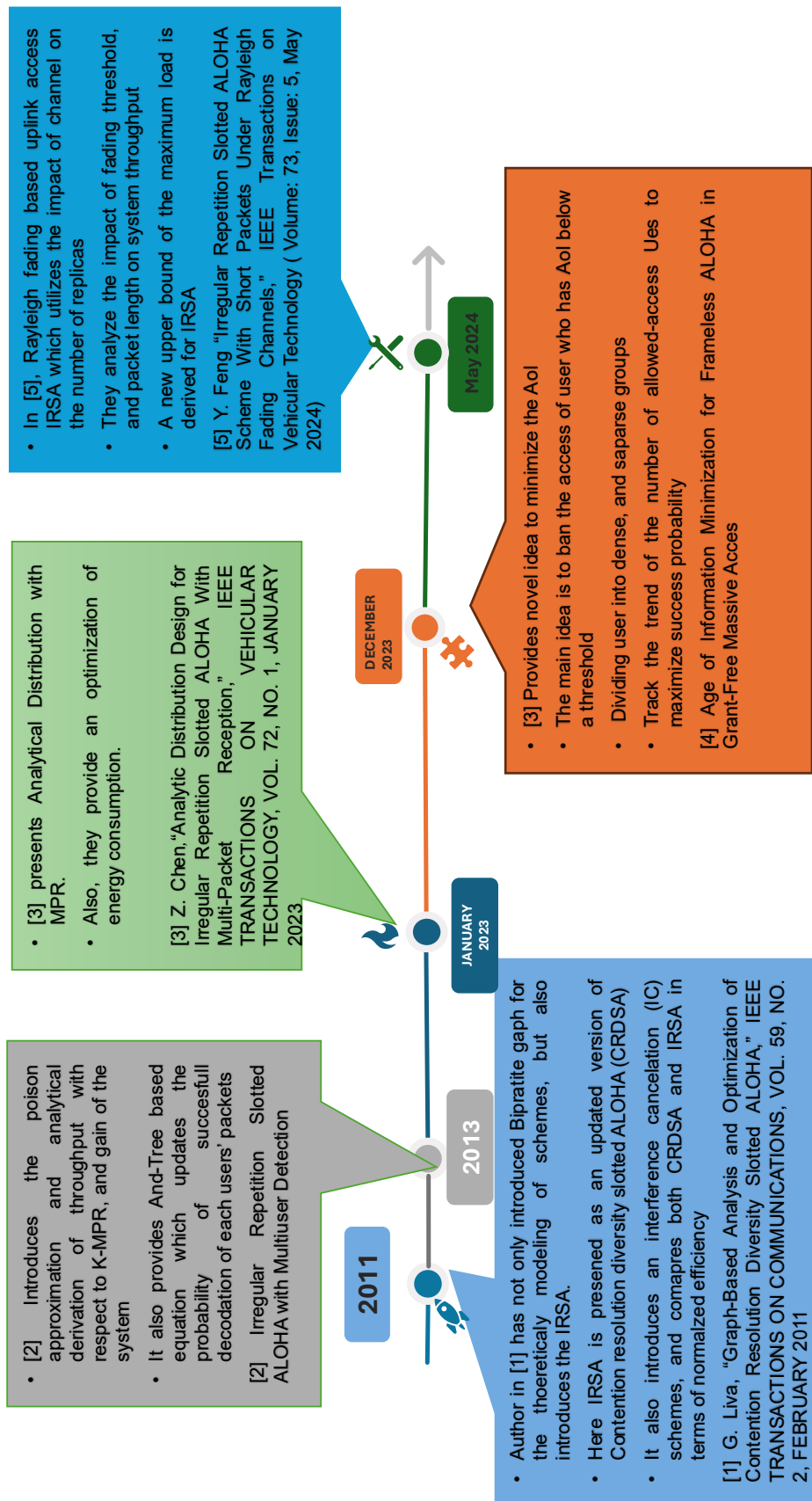


FIGURE 1.1: IRSA and Multi Packet Reception (MPR)

1.1 PD-NOMA and Goal Oriented Communication

Goal-oriented communication has emerged as a key paradigm in wireless IoT networks, where numerous devices and sensors continuously generate status updates. The primary objective is not to transmit all available data, but to ensure that the information delivered is both timely and relevant for decision-making, often supported by mMTC, and Mobile Edge Computing (MEC) architectures [48], [49].

Maintaining low AoI is particularly challenging in large-scale IoT networks due to scarce spectrum, energy limitations, heterogeneous device capabilities, and time-varying channel conditions [50]. In particular, energy-constrained devices require protocols with minimal signaling overhead and lightweight communication strategies [51].

Several works have studied AoI optimization through scheduling, resource allocation, and trajectory design [24], [33], [34]. Several threshold-based strategies have also been under consideration to control the limited access of devices, which helps in avoiding channel congestion [35]. However, these AoI-driven works generally assume ideal or unconstrained energy availability. Conversely, other studies focus on energy harvesting and efficient power management in IoT networks [29], [36], but do not consider information freshness as a performance objective. More recently, grant-based and grant-free access schemes combined with PD-NOMA, and RL have shown vast potential for improved spectral and energy efficiency [37], [38], [39], [40]. Specifically, [39] considers a two-level PD-NOMA scheme where a two-layer deep transfer learning decision is made slot by slot to choose higher and lower power level users. Figure 1.2 provides the summary of the evolution of PD-NOMA as Multi-Packet Reception (MPR) to enhance connectivity, while Table 1.3 addresses the application of PD-NOMA for AoI minimization in the existing literature.

Existing literature treats AoI optimization as a resource allocation problem; in general, policies do not learn decoding failures due to insufficient energy, inter-cell interference, and channel impact. Moreover, the likelihood that a status update is not successfully delivered within its allocated frame is rarely considered, despite its direct effect on information freshness. To the best of the authors' knowledge, no prior work jointly addresses AoI, energy harvesting impact mitigation by networks using a simple yet practical two-level PD-NOMA framework with minimal feedback signaling. In essence, the available energy, CSI, and efficient access strategy provide the foundation of massive connectivity, and we summarize the work of this part of the thesis in Figure 1.3.

1.2 Global Quantum Internet

The final part of the thesis involves providing scheduling solutions to global quantum internet connectivity through Low Earth Orbiting (LEO) satellites. There is a growing interest in various aspects of quantum networks and quantum communication, with particular emphasis on maximizing network throughput by addressing factors such as entangled photon distribution, routing, decoherence, fidelity, and quantum memory [52], [53], [54], [55].

Recent studies show significant advancements across both theoretical and practical dimensions. Kimble [56] highlights the critical role of quantum interconnects for enabling long-distance entanglement distribution and proposes architectures based on light-matter interactions to support scalable quantum networking. Cacciapuoti et al. [57] focus on quantum teleportation as the primary communication primitive, introducing an integrated model that combines quantum and classical channels while addressing decoherence challenges. Bacciotini et al. [58] propose a quantum network architecture inspired by classical internet principles, incorporating congestion control and queuing mechanisms to sustain fidelity and throughput despite quantum memory decoherence. [59] develops QuISP, a large-scale quantum network

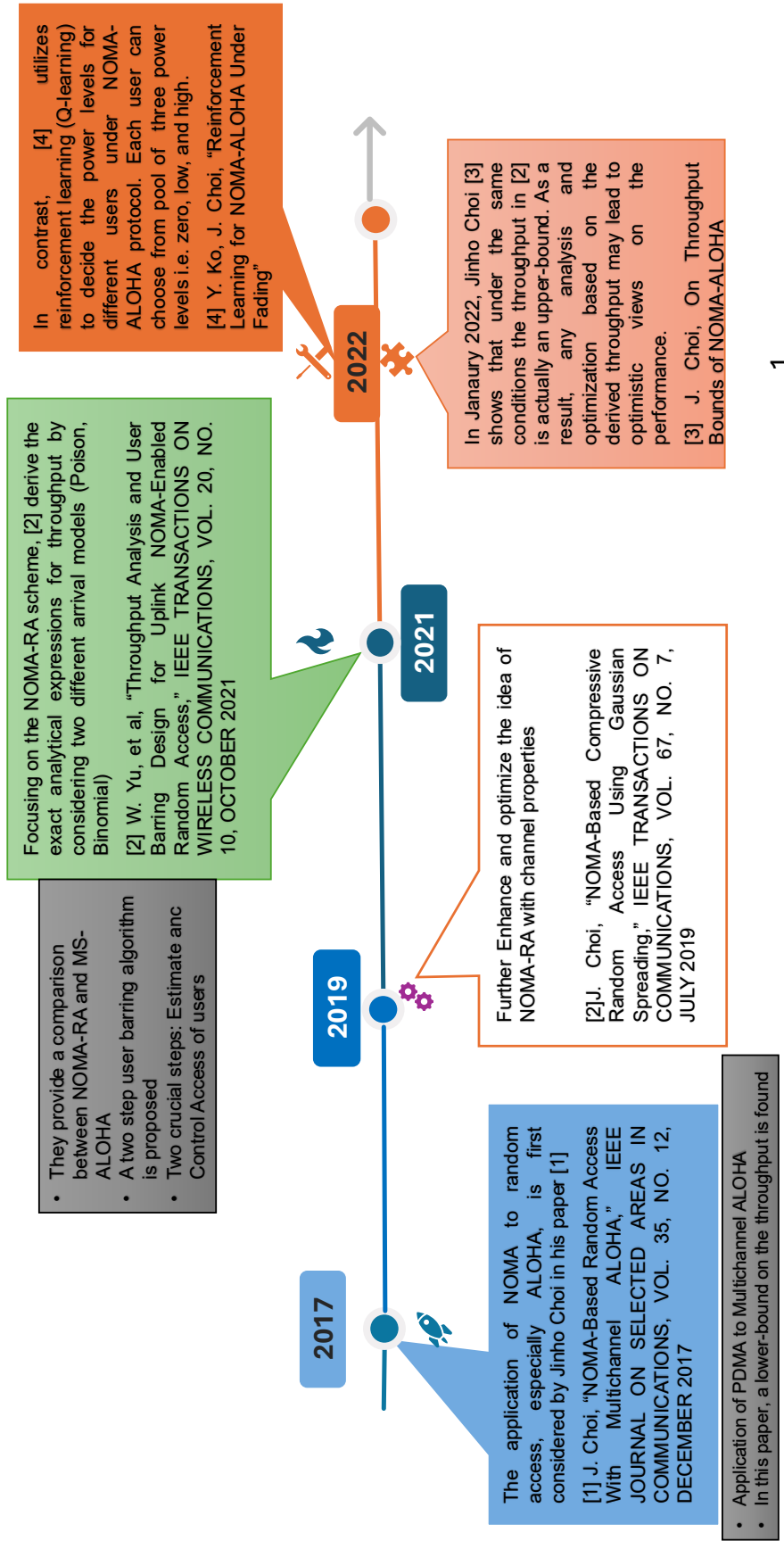


FIGURE 1.2: PD-NOMA as Multi Packet Reception for access enhancement

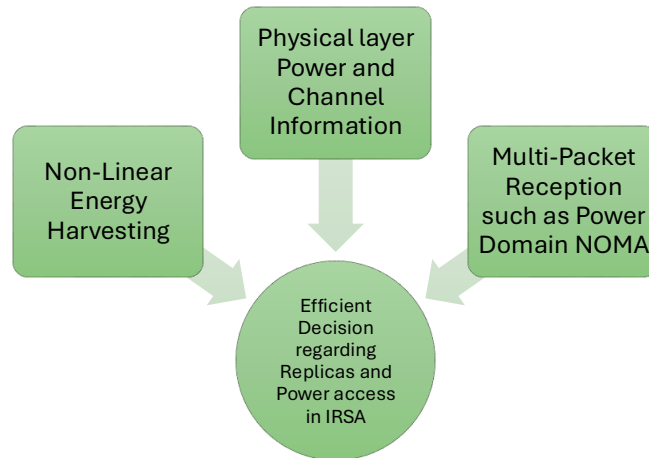


FIGURE 1.3: Idea of Channel, and Energy Efficient Decision making in resource access for massive access

simulator designed for protocol development and performance evaluation under realistic noise and network dynamics.

While early efforts focused on developing individual quantum subnetworks, achieving a global quantum internet requires the interconnection of quantum subnetworks across geographically distant locations.

By transmitting entangled photons through free-space satellite channels, these systems circumvent fiber attenuation losses, enabling high-fidelity entanglement distribution over thousands of kilometers. Pioneering demonstrations of satellite-mediated quantum communication and long-distance entanglement [60], [61] represent critical milestones toward scalable and practical quantum internet architectures.

Despite these advancements, satellite-based quantum links introduce new challenges that must be addressed to achieve reliable global quantum connectivity. Increased latency due to both distance and limited satellite communication windows, along with degradation of ebit coherence from atmospheric loss and alignment issues, remain significant obstacles [62], [63].

To address these challenges, recent studies have explored alternative entanglement generation models and optimization strategies for satellite-based quantum networks. On-demand strategies aim to reduce latency by dynamically selecting optimal paths, whereas pre-allocated models provide redundancy and robustness by generating multiple entangled links in advance, albeit at the cost of higher resource consumption. These two paradigms reflect a fundamental trade-off between real-time responsiveness and network resilience. To further minimize latency while preserving fidelity, several works have investigated optimal stopping strategies for entanglement generation [64], informing more efficient entanglement swapping and scheduling protocols.

Addressing the broader fidelity–latency trade-off, Sidhu et al. [65] provide a comprehensive overview of global quantum internet developments. Fittipaldi et al. [66] propose dynamic scheduling frameworks that account for memory and fiber losses, offering scalable network design strategies. Williams et al. [67] focus on maximizing satellite–ground connections, laying the foundation for time-slot-based coordination to manage latency. Similarly, Chang et al. [68] introduce a greedy entanglement scheduling strategy over defined time windows, while Mukhopadhyay et al. [69] emphasize the role of purification and decoherence in hybrid

networks, both crucial for maintaining fidelity under realistic operational conditions. Table 1.4 provides a summary of current trends in quantum internet.

With the availability of thousands of LEO all over the earth, which can provide sufficient entanglement rate, we aim to produce an efficient scheduling algorithm that chooses a satellite based on its characteristics, such as slant range, angle with respect to the ground station, and atmospheric link budget. The choice is made throughout the communication, and the goal is to maximize the long-term entanglement rate with a latency constraint.

1.3 Thesis Contributions

This thesis aims to provide RL based solutions to the problems of massive connectivity for mMTC, and long-haul connectivity to provide quantum connectivity across the globe through LEO satellites. The chapter 2 provides a Q-learning-based solution to PD-NOMA based IRSA, where the aim is to minimize network average AoI by optimizing the packet replicas and power assignment. While IRSA provides an excellent solution and encourages distributed decisions, the multiple replicas and high collision chances among users due to non-coordination can result in precious energy being lost by the sensors. Therefore, Chapter 3 provides an efficient Proximal Policy Optimization (PPO) scheduling algorithm. The algorithm requires minimal broadcast-based feedback to schedule devices while also providing an energy-efficient power allocation strategy. We extend our PPO based scheduling strategy towards the satellite selection policy to provide efficient global quantum internet in Chapter 4. Finally, the findings of the thesis work are concluded along with possible future suggestions.

TABLE 1.1: Review of Related Works

Papers	Year	Access Methods			Metrics			Energy Harvesting (EH)			Solution Approach			
		IRSA	SA	Scheduling	AoI	AoII	Vol	TP	EE	Ambient	AP	Analytical	MDP	RL
[20]	2021	✓						✓			✓			✓
[32]	2023	✓			✓						✓			
[7]	2023	✓					✓	✓		✓				
[8]	2023	✓						✓						
[30]	2023	✓											✓	
[5]	2023			✓										✓
[31]	2019	✓					✓			✓				
[21]	2020	✓					✓							✓
[29]	2024			✓			✓						✓	
[24]	2021	✓			✓								✓	
[9]	2022	✓						✓					✓	
[18]	2022		✓				✓							✓
[10]	2023		✓					✓		✓				
[25]	2024		✓			✓		✓					✓	
[11]	2025		✓					✓		✓			✓	
[27]	2025	✓			✓					✓				
[28]	2025		✓							✓			✓	
[22]	2022			✓						✓				✓
[23]	2024			✓						✓				✓
This Work	-	✓			✓			✓			✓			✓

TABLE 1.2: Summary of Related Works on Scheduling for Aol minimization

Papers	Year	System Focus			Performance Metrics		Learning / Access	
		Scheduling	Energy Model	PD-NOMA	Aol	EE		Threshold
[33]	2022	✓			✓			✓
[34]	2021	✓			✓			
[24]	2021	✓			✓		✓	
[35]	2019				✓		✓	
[36]	2023		✓			✓		
[29]	2024	✓	✓			✓		
[37]	2019				✓	✓		
[38]	2023				✓	✓		✓
[39]	2024	✓			✓	✓		✓
[40]	2024				✓	✓		✓
This Work	-	✓	✓	✓	✓	✓		✓

TABLE 1.3: Review of Related Works (PD-NOMA / IRSA / ALOHA, AoI-centric)

Papers	Year	Access Methods			Metrics					Energy Harvesting (EH)		Solution Approach		
		IRSA	SA	Scheduling	AoI	AoII	Vol	TP	EE	Ambient	AP	Analytical	MDP	RL
[32]	2023	✓			✓								✓	
[24]	2021	✓			✓								✓	
[41]	2022		✓		✓								✓	
[42]	2021		✓		✓								✓	
[28]	2025		✓		✓						✓		✓	
[43]	2017		✓				✓						✓	
[44]	2022		✓				✓							✓
[45]	2024		✓		✓								✓	
[7]	2023		✓				✓	✓					✓	
[8]	2023		✓					✓					✓	
[30]	2023		✓			✓							✓	
[5]	2023			✓			✓							✓
[31]	2019		✓				✓	✓					✓	
[21]	2020		✓				✓	✓					✓	
[29]	2024			✓			✓	✓					✓	
[20]	2022		✓				✓	✓					✓	
[9]	2022		✓				✓	✓					✓	
[18]	2022		✓				✓	✓					✓	
[10]	2023		✓				✓	✓					✓	
[25]	2024		✓				✓	✓					✓	
[11]	2025		✓				✓	✓					✓	
[27]	2025		✓				✓	✓					✓	
[22]	2022				✓									✓
[23]	2024				✓			✓						✓
[46]	2022				✓			✓						✓
[47]	2024				✓			✓						✓

TABLE 1.4: State of the Art and Their Contributions

Papers (Year)	Latency	Fidelity	Entanglement Distribution	Network Deployment	Dynamic	Protocol Optimization Level
[70] (2025)	✓	✓		Single	✓	Purification
[53] (2024)	✓	✓	✓	Single		Generation
[71] (2024)		✓	✓	Single		Entanglement
[72] (2018)			✓	Single	✓	Entanglement
[73] (2024)			✓	Hybrid	✓	Throughput
[68] (2024)			✓	Hybrid	✓	Entanglement
[74] (2024)			✓	Hybrid	✓	Entanglement

Chapter 2

Distributed Q-Learning for Age of Information Optimization

Efficient Random Access (RA) is critical for supporting massive connectivity in low-power sensor networks. However, the stochastic nature of EH and time-varying wireless channels limits the performance of static, model-based RA schemes, particularly in applications requiring timely, goal-oriented updates. This chapter proposes an online RA framework based on reinforcement learning for distributed, energy-aware decision-making. A Hybrid Access Point (HAP) with energy harvesting capability is assumed, equipped with decoding mechanisms based on the capture effect and SIC. Two RL-based variants of IRSA are developed: the Energy Efficient Independent Learner (EE-IL). These schemes exploit instantaneous Channel State Information and residual energy to optimize transmission strategies. The proposed approach minimizes the AoI while adapting to real-time system dynamics.

2.1 Introduction

While classical metrics such as throughput and delay have guided MAC design, emerging applications increasingly require timely, task-relevant information. In this context, the AoI metric has emerged as a more suitable indicator of information freshness [75]. Ensuring low AoI under energy limitations, sporadic traffic, and fading channels necessitates adaptive, efficient access policies. Recent efforts have incorporated AoI-aware random access mechanisms [23], [24] and EH constraints [11], [27], [31]. Furthermore, [28] emphasizes the importance of the capture effect in improving SIC, advocating its deliberate control. However, current models often treat AoI, CSI, and energy harvesting independently, relying on fixed, model-based policies that lack adaptability and overlook real-time channel or battery dynamics.

To address these limitations, this chapter proposes a model-free Q-learning framework for AoI-aware, energy-harvesting IRSA. A reinforcement learning strategy EE-IL is developed. It is a decentralized scheme where each MTCD adapts its transmission policy using local energy and channel feedback, requiring only periodic broadcasts from the Hybrid Access Point (HAP).

The proposed model captures nonlinear energy harvesting, finite battery capacity, and time-correlated fading, which is modeled as a finite-state Markov process. A composite reward function balances AoI minimization with sustainable energy usage. A dynamic degree distribution mechanism is proposed, allowing each MTCD to adapt its transmission strategy based on local energy and channel state, enabling AoI- and energy-aware random access. A convergence-aware learning framework is introduced, supporting stable offline execution with reduced retraining frequency, thereby enhancing efficiency in dynamic environments.

TABLE 2.1: Symbol Notation

Symbol	Description
M	Number MTCDs in the system
N	Number of available slots per frame
\mathbb{M}	Set of all MTCDs in the system
\mathbb{N}	Set of slots
Λ_ℓ	Probability of transmitting ℓ replicas
$\Lambda(x)$	Polynomial distribution of replicas
G	Normalized channel load, $G = M/N$
$\Omega^{(i)}$	configuration of replicas for frame i
π	Complete access policy for replicas
P_m	Transmitted power of m -th MTCD
P_{hap}	Transmitted power for Wireless Energy Transmission (WET)
$h_m^{(i)}$	complex channel coefficient between m and the HAP
$\gamma_m^{(i)}$	Channel power-gain of m th MTCD
d_m	Distance between m and HAP
$\Upsilon(\cdot)$	Power gain grading function
v_j	j -th channel gain threshold power
$\mathcal{T}_n^{(i)}$	set of transmitting MTCD in the n -th slot
$\omega_m^{(i)}$	energy storage of m -th MTCD
E_m	Harvested energy for m -th MTCD
$\zeta_m^{(i)}$	number of available transmission units for m -th MTCD
$A_m^{(i)}(n)$	Instantaneous AoI of the m -th MTCD at slot n
\bar{A}	System Age of Information
$a_{m,i}$	Action taken by MTCD m at iteration i
$s_{m,i}$	State of MTCD m at iteration i
$r_{m,i}$	Reward obtained by MTCD m at iteration i
$\zeta_{m,i}$	Battery level of MTCD m at iteration i
$Q(s, a)$	Q-table
ϵ	Exploration probability in ϵ -greedy policy
F	Frame matrix tracking decoded packets
I	Total number of iterations (frames) per test
T	Total number of test runs
ω	Raw battery level
z	Unit of battery required to send one replica

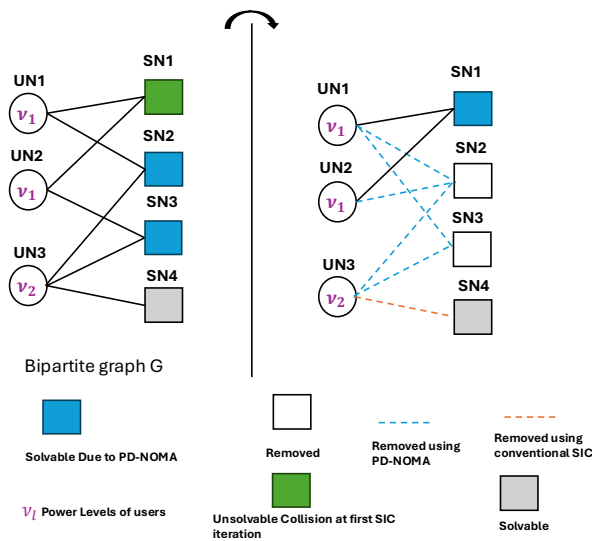


FIGURE 2.1: Bipartite Representation of SIC process with PD-NOMA

2.2 System Model

This section describes the system model, encompassing the network topology, wireless channel characteristics, and the non-linear energy harvesting model. The PD-NOMA is incorporated into the communication model as MPR. Additionally, we introduce the discretization of both the wireless channel and the battery state, which is crucial for constructing the Q-table in the learning algorithm. The definition of AoI, along with the data sampling procedure, is also provided. For a complete description of the notation used throughout the chapter, refer to Table 2.1.

2.2.1 Network Deployment

We consider a wireless network comprising a set of M MTCDs, denoted by $\mathbb{M} = \{m \mid m = 1, 2, \dots, M\}$, which are densely deployed to monitor environmental conditions and periodically transmit time-stamped status updates to a HAP. The HAP operates in half-duplex mode and supports both Wireless Information Transmission (WIT) and WET. While uplink data transmissions are carried out during WIT, idle slots within the same period are utilized for downlink WET, enabling energy replenishment of MTCD batteries via a wireless EH mechanism. Fig. 2.2 illustrates the overall frame structure and the corresponding access behavior. Time is divided into discrete frames indexed by the set $\mathcal{I} = \{i \mid i = 0, 1, \dots, I - 1\}$. Each frame consists of N time slots indexed by the set $\mathbb{N} = \{n \mid n = 0, 1, \dots, N - 1\}$. Medium access is governed by the IRSA protocol. In each frame, every MTCD transmits one or more replicas of its data packet, where the number of replicas is drawn from a predefined distribution $\Lambda = \{\Lambda_\ell\}$, with Λ_ℓ denoting the probability of transmitting ℓ replicas. The selected replicas are independently assigned to slots chosen uniformly, under the constraint that no device transmits more than one replica in the same slot.

The transmission schedule of all MTCDs in a generic frame $i \in \mathcal{I}$ is captured by the binary matrix $F^i \in \{0, 1\}^{M \times N}$, where

$$F_{m,n}^{(i)} = \begin{cases} 1, & \text{if MTCD } u_m \text{ selects slot } n, \\ 0, & \text{otherwise.} \end{cases}$$

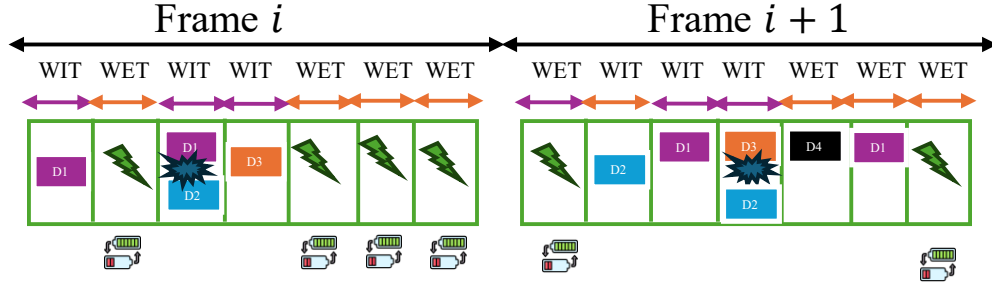


FIGURE 2.2: Frame Structure of IRSA with Energy Harvesting

The number of replicas selected by each MTCD is governed by a node-perspective polynomial Probability Density Function (PDF), given by:

$$\Lambda(x) = \sum_{\ell} \Lambda_{\ell} x^{\ell}, \quad (2.1)$$

The configuration of replicas for the frame i is denoted by the set $\Omega^{(i)} = \{\ell_1^{(i)}, \ell_2^{(i)}, \dots, \ell_m^{(i)}, \dots, \ell_M^{(i)}\}$, where $\ell_m^{(i)} \in \{0, \dots, W\}$ indicates the number of replicas selected by the m -th MTCD in frame i . Where W is the maximum allowed replicas. The complete access policy over the horizon of I frames is represented by the sequence $\pi = \{\Omega^{(0)}, \Omega^{(1)}, \dots, \Omega^{(i)}, \dots, \Omega^{(I-1)}\}$.

The objective of this work is to determine the optimal policy π from the space of admissible policies Π that minimizes the overall network AoI, subject to energy availability constraints at each MTCD. Since the traffic load may vary, we evaluate the optimal policy under different network traffic conditions. The normalized traffic load, also referred to as the traffic gain [76], is defined as:

$$G = \frac{M}{N}, \quad (2.2)$$

which quantifies the average number of contending MTCDs per slot within a MAC frame.

2.2.2 Channel Model and CSI-aware PD-NOMA

The received signal at the n -th slot of the i -th frame is modeled as:

$$y_n^{(i)} = \sum_{m=1}^M h_m^{(i)} \sqrt{P_k} \cdot F_{m,n}^{(i)} + w_n^{(i)}, \quad (2.3)$$

where P_k is the transmit power of the m -th MTCD. MTCD m chooses a power level P_k from a given L levels defined as $P_1 > \dots, P_k, \dots > P_L > 0$ (P_1 and P_L are the highest and lowest power levels respectively a MTCD can choose). $h_m^{(i)}$ is the corresponding channel coefficient (assumed constant over frame i), $F_{m,n}^{(i)} \in \{0, 1\}$ indicates whether device m transmits a replica in slot n of frame i , and $w_n^{(i)} \sim \mathcal{CN}(0, 1)$ denotes the additive white Gaussian noise (Additive White Gaussian Noise (AWGN)). The wireless channel is modeled using Rician fading, capturing both Line of Sight (LOS) and scattered components [77]. Following the standard Rician distribution, the corresponding Rician K -factor is defined as:

$$\kappa = \frac{\nu^2}{2\sigma^2}, \quad (2.4)$$

which quantifies the power ratio between the deterministic and scattered components. The complex channel coefficient between MTCD m and the HAP in frame i is given by:

$$h_m^{(i)} = \sqrt{\frac{\kappa}{\kappa+1}} + \sqrt{\frac{1}{\kappa+1}} \tilde{h}_m^{(i)}, \quad \tilde{h}_m^{(i)} \sim \mathcal{CN}(0, 1). \quad (2.5)$$

The corresponding distance-dependent channel power gain is expressed as:

$$\gamma_m^{(i)} = D \cdot |h_m^{(i)}|^2, \quad (2.6)$$

where the path loss D is defined as

$$D = \beta (d_m^{(i)})^{-2} \quad (2.7)$$

Here, β is the path gain at a reference distance of 1 meter, $d_m^{(i)}$ denotes the distance between MTCD m and the HAP during frame i . The distance $d_m^{(i)}$ is assumed to be uniformly distributed within $[d_{\min}, d_{\max}]$. The system operates in a Time Division Duplex (TDD) mode with block fading, where channel reciprocity holds. We assume perfect CSI is available at the MTCD via pilot signaling.

Let $\gamma_{th} > 0$ be the threshold per-stage SINR (e.g., $\gamma_{th} = 2^R - 1$ for rate R) to satisfy the decoding criteria (conditioned within a slot that only one MTCD has chosen a specific power level), and unit variance noise w_n^i . Following the NOMA-IRSA design [78], MTCD m chooses the *received* power targets from available $\{\mu_k\}_{k=1}^L$ levels. The levels are specified as follows.

$$\mu_k = \gamma_{th} \left(1 + \sum_{j>k} \mu_j \right), \quad k = L, L-1, \dots, 1. \quad (2.8)$$

Starting from the lowest level L (no lower-level interference), we obtain

$$\mu_L = \gamma_{th}, \quad \mu_{L-1} = \gamma_{th}(1 + \mu_L) = \gamma_{th}(1 + \gamma_{th}), \quad (2.9)$$

and is generally defined as,

$$\mu_k = \gamma_{th} (1 + \gamma_{th})^{L-k}, \quad k = 1, 2, \dots, L. \quad (2.10)$$

Given a MTCD u with instantaneous (linear) channel power gain γ_m , the *transmit* power that realizes level k is

$$P_{u,k}^{\text{tx}} = \frac{\mu_k}{\gamma_m} = \frac{\gamma_{th}}{\gamma_m} (1 + \gamma_{th})^{L-k}, \quad (2.11)$$

subject to $P_{u,k}^{\text{tx}} \leq P_{\max}$ and battery/energy-feasibility constraints. SIC would be able to decode an MTCD m sending its replica with power μ_k in a slot n if no other MTCD has the replica with the same μ_k power level.

2.2.3 κ -Factor-aware Discrete Channel grading

We assume that the distance between HAP and MTCD varies slowly, such that path loss can be treated as constant for many frames and defined as $D = \beta (d_m^{(i)})^{-2}$. Whereas the Rician fading part of the channel $Z(K) = |h_m^{(i)}|^2$, the normalized Rician power with $\mathbb{E}[Z | K] = 1$ and Cumulative Distributive Function (CDF)

$$F_Z(z; K) = 1 - \mathbb{Q}_1(\sqrt{2\kappa}, \sqrt{2(1+\kappa)z}), \quad (2.12)$$

where $\mathbb{Q}_1(\cdot, \cdot)$ is the Marcum- \mathbb{Q}_1 function.

Therefore, the overall channel is a scaled version of Rician fading with a constant path loss exponent scaling and power gain: is given as $\gamma_{th} = D \cdot Z(K)$.

The channel bin used in the RL state will be derived from γ_{th} via quantiles that are κ -aware and distance-aware. We start with by fixing the number of channel grades/bins $V \in \mathbb{Z}_{\geq 2}$. For a given κ , define the normalized quintiles $\{z_v(\kappa)\}_{v=1}^{V-1}$ as the solutions of

$$F_Z(z_v(\kappa); \kappa) = \frac{v}{V}, \quad v = 1, \dots, V-1. \quad (2.13)$$

Interpretation: for this κ , each interval $(z_{v-1}(\kappa), z_v(\kappa)]$ contains exactly $1/V$ of the probability mass of Z . This step is *independent of distance* and produces K -aware, normalized thresholds.

Conditioned on (D, κ) , the CDF of γ_{th} is a scaled version of F_Z :

$$F_{\gamma_{th}|D, \kappa}(x) = \Pr(DZ \leq x \mid D, \kappa) = \Pr(Z \leq x/D \mid \kappa) = F_Z(x/D; \kappa). \quad (2.14)$$

The v/V quantile of γ_{th} given (D, κ) , denoted $r_v(D, \kappa)$, satisfies

$$F_{\gamma_{th}|D, \kappa}(r_v(D, \kappa)) = \frac{v}{V} \iff F_Z(r_v(D, \kappa)/D; \kappa) = \frac{v}{V}. \quad (2.15)$$

Thus,

$$t_v(D, \kappa) = D z_v(\kappa), \quad v = 1, \dots, V-1. \quad (2.16)$$

Hence, the absolute thresholds for γ_{th} are the κ -aware normalized Rician quintiles, scaled by the current slowly varying distance-dependent path loss D .

Given the measured instantaneous gain γ_{th} (from the pilot) and the MTCD currently experience CSI with parameters (D, κ) :

$$t_v(D, \kappa) = V z_v(K), \quad v = 1, \dots, V-1, \quad (2.17)$$

$$v = 1 + \sum_{v=1}^{V-1} \mathbf{1}\{\gamma_{th} > t_v(D, \kappa)\} \in \{1, \dots, V\}. \quad (2.18)$$

Equivalently, c is the unique index such that $r_{c-1}(D, \kappa) < \gamma_{th} \leq r_c(D, \kappa)$ satisfying the condition

$$\Pr\{r = v \mid D, \kappa\} = \frac{1}{V}, \quad v = 1, \dots, V, \quad (2.19)$$

2.2.4 Energy Harvesting Model

We assume that MTCDs are uniformly distributed around the HAP in a clustered topology. During a given frame, the HAP observes each slot as one of the following:

- (i) *Singleton slot:* only one MTCD transmits and is successfully decoded.
- (ii) *Collision slot:* multiple MTCDs transmit; decoding is attempted via SIC following the IRSA protocol.
- (iii) *Idle slot:* no transmissions occur; the slot is available for WET.

Whenever an idle slot is detected, the HAP broadcasts energy to perform WET. The MTCDs are always in energy receiving mode whenever they are not transmitting.

We adopt the nonlinear energy harvesting model from [36]. The energy harvested by MTC m is denoted by E_m and is given by:

$$E_m = \frac{\alpha_0 P_{\text{hap}} \delta \gamma_m^{(i)}}{\alpha_1 P_{\text{hap}} \gamma_m^{(i)} + \alpha_1}, \quad (2.20)$$

where P_{hap} is the transmit power of the HAP, δ is the energy transfer duration (equal to the slot duration), and $\alpha_0 = 0.826$, $\alpha_1 = 0.399$ are constants modeling the nonlinear energy conversion efficiency.

At the beginning of each frame i , each MTC m selects a transmission degree $\ell_m^{(i)}$, and transmit with power $P_{u,k}^{\text{tx}}$, hence consuming $\ell_m^{(i)} P_{u,k}^{\text{tx}} \delta$ Joules of energy to send $\ell_m^{(i)}$ replicas. Harvested energy from idle slots is added during the frame.

The continuous battery level $\omega_m^{(i)} \in \{0, \omega_{\text{max}}\}$ can be defined as at the end of frame i is updated as:

$$\omega_m^{(i)} = \left(\omega_m^{(i-1)} - \ell_m^{(i)} P_{u,k}^{\text{tx}} \delta \right) + \sum_{n=1}^N \phi_n^{(i)} E_m, \quad (2.21)$$

where $\phi_{m,n}^{(i)} \in \{0, 1\}$ indicates whether slot n was idle for WET during frame i . while the discrete battery state can be defined as

$$\zeta_m^{(i)} = \left\lfloor \left(\frac{\omega_m^{(i)}}{\omega_{\text{max}}} \right) B \right\rfloor \in \{0, 1, \dots, B\} \quad (2.22)$$

Here ω_{max} is the maximum battery capacity of MTC.

2.2.5 Age of Information

The primary objective of this work is to ensure timely and fresh data collection from MTCs. To quantify data freshness, we employ the AoI metric, which measures the time elapsed since the most recent successfully received update was generated. The AoI can guide both centralized decision-making at the HAP and decentralized policies at individual MTCs.

We define the instantaneous AoI of the m -th MTC at slot t of frame i as $A_m^{(i)}(t)$, where $t = 1 \rightarrow T$ is the time horizon under consideration divided into discrete slots of equal length. At the beginning of the operation, the initial age is set as $A_m^{(1)}(0) = 0$ for all m . In the absence of a successful update, the AoI increases linearly with time. The evolution of the age is described as:

$$A_m(t) = \begin{cases} A_m(t-1) + 1, & \text{if } m \text{ is not recovered in } t, \\ R_m^{(i)} - O_m^{(i)} + 1, & \text{if } m \text{ is recovered in } t, \end{cases} \quad (2.23)$$

where $O_m^{(i)}$ denotes the slot in which the first replica of the packet was transmitted in frame i (i.e., the generation time), and $R_m^{(i)}$ denotes the slot in which the packet was successfully decoded in frame i . Note that the second condition can become true only if the policy allows MTC m to transmit in frame i , and in case of no transmission, AoI increases by N during a frame. This model adheres to the *GT* paradigm, where the update is associated with the time of the first transmission attempt.

Recovery of a packet can occur in three ways: immediately in a singleton slot, through the capture effect, or subsequently via SIC. We adopt the *REARLY- k* decoding policy [24], which prioritizes early recovery using the capture effect before proceeding with SIC.

The long-term time-averaged AoI for device m is defined as:

$$\bar{A}_m = \lim_{T \rightarrow \infty} \frac{1}{T} \sum_{i=1}^T A_m(i), \quad (2.24)$$

The system-wide average AoI is then computed as:

$$\bar{A} = \frac{1}{M} \sum_{m=1}^M \bar{A}_m. \quad (2.25)$$

At the end of each frame i , the combined instantaneous AoI across all users is represented by the vector:

$$A^{(i)} = [A_1^{(i)}(N), A_2^{(i)}(N), \dots, A_M^{(i)}(N)], \quad (2.26)$$

which captures the final age values of all M devices in that frame.

2.3 Markov Decision Process Formulation

In RA-based mMTC, MTCDs operate in a decentralized manner with coordination from the HAP. Their access strategy is governed by a probability distribution $\Lambda(x)$, which determines the number of packet replicas each device transmits. We model the packet replication control problem as a MDP to dynamically optimize this distribution for minimizing the AoI. The MDP is formalized by the tuple $\mathcal{M} = (\mathcal{S}, \mathcal{A}, P_t, r)$, consisting of the state space \mathcal{S} , action space \mathcal{A} , transition probability function P_t , and reward r .

State: To enable CSI and battery-aware decision-making, we define the state of the m -th MTCD at the beginning of frame i updated during the broadcasting phase between frame $i-1$ and i . The state remains constant throughout the frame, as we consider block-fading and energy harvested during the current frame does not affect the decision of replica selection.

At the start of frame i , MTCD m observes its AoI, discrete CSI, and battery,

$$s_m^{(i)} = (\zeta_m^{(i)}, v_m^{(i)}), \quad (2.27)$$

where $A_m^{Ind}(N)$ indicate whether the AoI of MTCD violates a threshold τ .

denotes the discrete battery level, and $v_m^{(i)}$ is the channel grade determined using the method described in Section 2.2.3. The joint state of all MTCDs at frame i is denoted by $\mathbb{S}^{(i)} = \{s_1^{(i)}, s_2^{(i)}, \dots, s_M^{(i)}\}$.

Action: The action taken by the m -th MTCD in the i -th frame is defined as $a_m^{(i)} = \pi(s_m^{(i)}) \in \{0, \dots, \zeta_{\max}\}$, representing the number of replicas transmitted, and the PD-NOMA power level subject to available energy. The set of actions for all MTCD in frame i is denoted by $\mathbb{A}^{(i)} = \{a_1^{(i)}, a_2^{(i)}, \dots, a_M^{(i)}\}$. Where individual $a_M^{(i)} = (l, P_k)$.

Masked Q-learning with Feasibility Indicator

Since a threshold γ_{th} must be satisfied while selecting any power level, each MTCD's Q table must be updated for every CSI update and given feasible/possible choices of actions. To ensure that only energy and CSI feasible actions are considered, we introduce an indicator function for user u :

$$\mathbb{1}_m(\ell, k | s) = \begin{cases} 1, & \text{if } \ell \cdot u_{m,k} \leq \omega_u, \\ 0, & \text{otherwise,} \end{cases} \quad (2.28)$$

where $u_{m,k} = \left\lceil \frac{P_{u,k}^{\text{tx}} \delta}{E_0} \right\rceil$ is the discrete energy cost (in units of E_0) for transmitting one replica at power level k .

The feasible action set for state s is then

$$\mathcal{A}(s) = \{(\ell, k) : \mathbb{1}_u(\ell, k | s) = 1\}. \quad (2.29)$$

Reward:

The reward for each device m in frame i is defined as

$$r_m^i = -w_a A_m^i(N) - w_E E_m^i, \quad (2.30)$$

where $E_m^i = \ell_m^{(i)} P_{u,k}^{\text{tx}} \delta$ is the energy cost of the device during the frame, and $A_m^i(N)$ is the AoI at the end of the frame i . The weights w_a , and w_E decide how much importance each objective gets.

2.3.1 Optimization Problem Formulation

We consider a wireless-powered mMTC system with M MTCDs transmitting status updates over N time slots per frame, across I frames in total. Each device $m \in \{1, \dots, M\}$ selects the number of replicas ℓ_m to transmit and the corresponding transmission power P_m^{tx} , which is associated with one of the available PD-NOMA power levels μ_k . The goal is to minimize the network-wide average Age of Information (AoI) and total energy consumption while satisfying transmit power and battery constraints.

$$\begin{aligned} \min_{\pi \in \{\ell_m, P_m^{\text{tx}}\}} \quad & \frac{1}{MIN} \sum_{i=1}^I \sum_{n=1}^N \sum_{m=1}^M A_m(i, n) + \sum_{m=1}^M E_m \\ \text{s.t.} \quad & P_m^{\text{tx}} = \frac{\mu_k}{\gamma_m}, \quad \forall m, \\ & P_m^{\text{tx}} \leq P_{\max}, \quad \forall m, \\ & \ell_m e_{m,k} \leq B_m, \quad \forall m, \\ & 1 \leq \ell_m \leq \ell_{\max}, \quad P_m^{\text{tx}} \geq 0, \quad \forall m. \end{aligned} \quad (2.31)$$

Here, $A_m(i, n)$ denotes the instantaneous AoI of device m in slot n of frame i , and E_m is its total energy consumption. The transmission power P_m^{tx} depends on the selected NOMA power coefficient μ_k and the channel gain γ_m . The constraint $\ell_m e_{m,k} \leq B_m$ ensures that the total transmission energy per frame does not exceed the available battery energy B_m . The objective thus minimizes the combined cost of average AoI and energy usage by jointly determining the optimal number of replicas ℓ_m and transmit power levels P_m^{tx} .

Accordingly, the Q-learning update rule is modified as

$$Q(s, a) \leftarrow (1 - \eta) Q(s, a) + \rho \left[r + \eta \cdot \max_{a' \in \mathcal{A}(s')} Q(s', a') \right], \quad (2.32)$$

where $a = (\ell, k)$ is the chosen action, r is the received reward, s' is the next state, η is the learning rate, and ρ is the discount factor. The Q-table $Q(s, a) \in \mathbb{R}^{B.V \times W.L}$ represents the Q-values of taking each action. Figure 2.11 shows the complete flow of EE-IL.

2.4 PD-NOMA SIC with REARLY-K slot-wise decoding

For a fixed target decoding threshold $\gamma_{th} > 0$, and design received targets $\{\mu_k\}_{k=1}^L$ to realize the SIC order. A level- k packet in slot n is *intra-slot decodable* if and only if

$$\mathbf{c}_n \in \mathcal{D}(k; \gamma_{th}) \triangleq \begin{cases} \text{(i) } c_{n,j} = 0 \quad \forall j < k & \text{(all stronger levels already removed),} \\ \text{(ii) } c_{n,k} = 1 & \text{(singleton at the target level),} \\ \text{(iii) } \frac{\mu_k}{N_0 + \sum_{j>k} c_{n,j} \mu_j} \geq \gamma_{th} & \text{(thresholded weaker-interference budget).} \end{cases} \quad (2.33)$$

Condition (i)–(ii) match the *type- k decodable set* in IRSA+NOMA; (iii) enforces a per-level SINR threshold so that decodes only occur when the residual mixture is physically admissible. The classical IRSA+NOMA decodable patterns are recovered as special cases of (2.33) by the appropriate choice of $\{\mu_k\}$ and γ_{th} .

Same-level collisions. If $c_{n,k} \geq 2$, (2.33)(ii) fails; the slot is *temporarily* undecodable at level k . Such collisions are resolved only after inter-slot cancellations reduce $c_{n,k}$ to 1, at which point (2.33)(iii) is re-checked.

2.4.1 Slot-wise (REARLY- k) decoding with immediate inter-slot IC

We decode greedily *per slot* (earliest slots first for AoI) and propagate cancellations across the frame in real time.

Algorithm 1 Slot-wise SIC with Cross-slot IC (REARLY- k)

- 1: Initialize the decoded-user set $\mathcal{U}_{dec} \leftarrow \emptyset$; build \mathbf{c}_n for all n from buffered observations.
 - 2: **for** $n = 1, 2, \dots, N$ **do**
 - 3: **Cancel known users:** subtract all $u \in \mathcal{U}_{dec}$ present in slot n ; update \mathbf{c}_n .
 - 4: **repeat**
 - 5: **if** $\exists k$ with $\mathbf{c}_n \in \mathcal{D}(k; \gamma_{th})$ **then**
 - 6: Decode the unique level- k packet (CRC check); let the user be u^* ; add u^* to \mathcal{U}_{dec} .
 - 7: **Intra-slot IC:** subtract u^* from slot n .
 - 8: **Inter-slot IC:** using replica pointers, subtract u^* from all other slots where it appears; update each affected $\mathbf{c}_{n'}$.
 - 9: **else**
 - 10: **Stop** intra-slot SIC at n (no k passes (2.33)).
 - 11: **end if**
 - 12: **until** no k satisfies (2.33) in slot n
 - 13: **Optional look-back:** enqueue any earlier slot that just became decodable after cancellations.
 - 14: **end for**
-

2.5 Results and Discussion

In this section, we analyze the performance of our two algorithms and compare them with benchmark policies. The hyperparameters of Q-learning and other fixed parameters are given in Table 2.2. We detail and analyze the learning and performance enhancement through several metrics presented in the subsections below.

Figure 2.3 proves the convergence of Q-learning based EE-IL by showing reward maximization for different power levels. As one can expect, the lower power level choice of $k = 2$ provides suboptimal performance, while as power levels increase with $k = 3, 4, 5$, we can observe more efficient reward maximization. However, the gap between maximization becomes smaller as the energy constraint effect becomes more evident. Even though more power levels provide more freedom, it also requires a significant transmission power gap to successfully decode the packet, which becomes challenging to achieve for low-energy sensors.

While the reward maximization proves AoI convergence, Figure 2.4 shows the learning of EE-IL to optimize its energy consumption during the frame iterations. The figure shows that lower $k = 2, 3$ consume on average 0.045 Joules of energy, while the higher power level $k = 4, 5$ consume 0.055 Joules on average, while optimized. The energy trend shows as the reward converges, energy consumption, which was initially increasing trend also converges to the optimal point.

To further prove the efficient utilization of PD-NOMA, Figure 2.6 provides evidence that even for higher $G > 2$, the more levels play a crucial role in reducing the Average Age of Information (AAoI). While Figure 2.7 shows the importance of CSI and battery-aware learning when compared with a random replica, as well as power selection (Random strategy) and an energy-based greedy policy, which maximizes energy utilization. The superior performance of the proposed EE-IL is evident here.

The aim of the proposed EE-IL is to find an optimal policy that, under certain traffic load conditions and under certain available freedom of choice, aims at minimizing AoI and optimizing the energy utilization. We show different optimized access policies for varying traffic loads $m = \{10, 12, 15\}$ with fixed $N = 5$. We can observe that as the power level availability increases, policies shift towards fewer replicas, aiming to achieve energy efficiency.

TABLE 2.2: Simulation Parameters

Parameter	Value	Description
η	0.0001	Learning Rate
ρ	0.99	Discount Factor
ϵ	0.2	Initial Prob. of Exploration
T	1000	Number of test episodes
i	25000	Epochs in one test episode
τ	10	Update frequency of Eq. ??
d	[1, 12] meters	MTCD and HAP distance
κ	12	Rician Factor
δ	1 ms	Time duration single slot
P	46dBm	HAP Tx Power
M	{10, 12, 15}	MTCDs

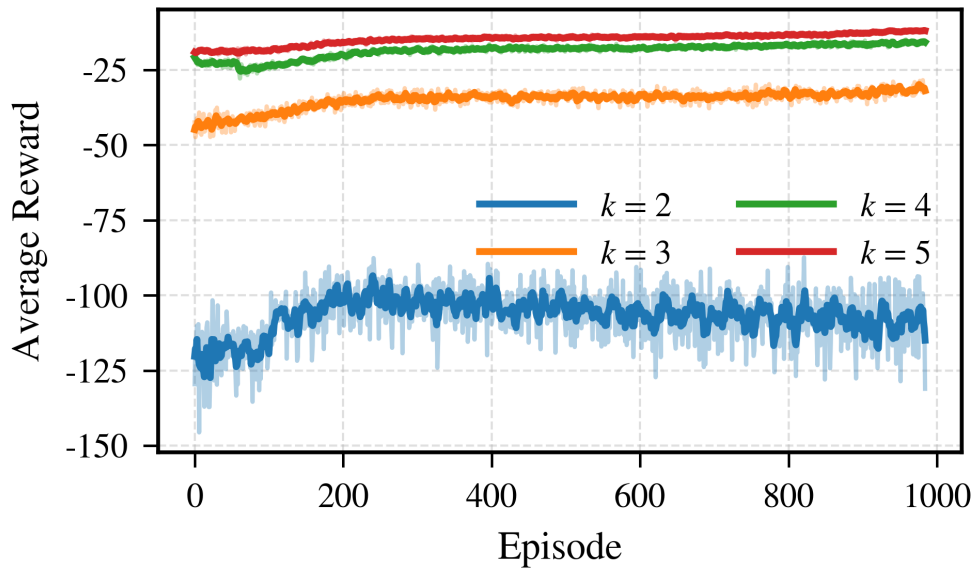


FIGURE 2.3: Average Reward per Episode for Power Level $M = 10$, $k = \{2, 3, 4, 5\}$

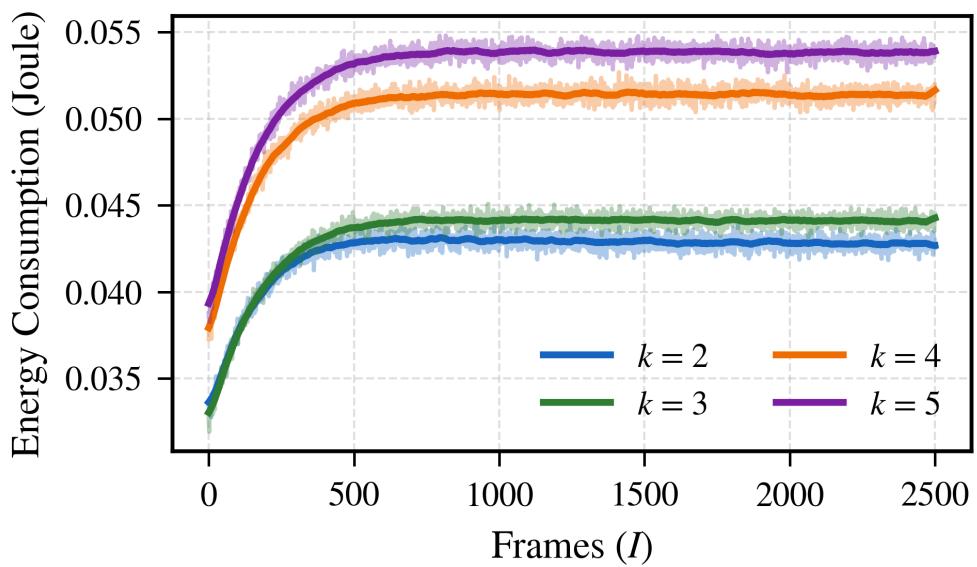


FIGURE 2.4: Average energy consumption convergence towards optimal as the frames I progress, $N = 5$, $M = 10$

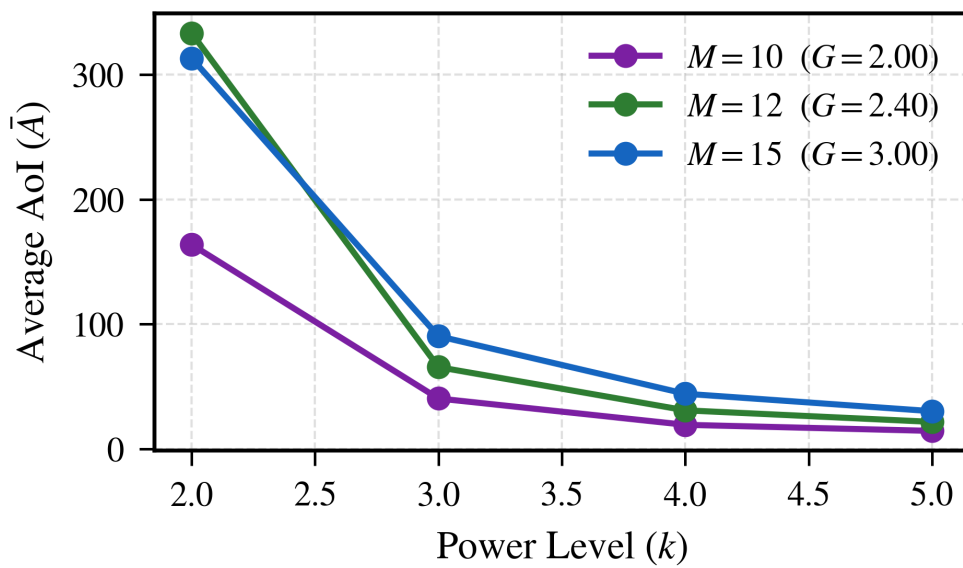


FIGURE 2.5: Average \bar{A} when total number of power levels $K \in \{2, 3, 4, 5\}$.

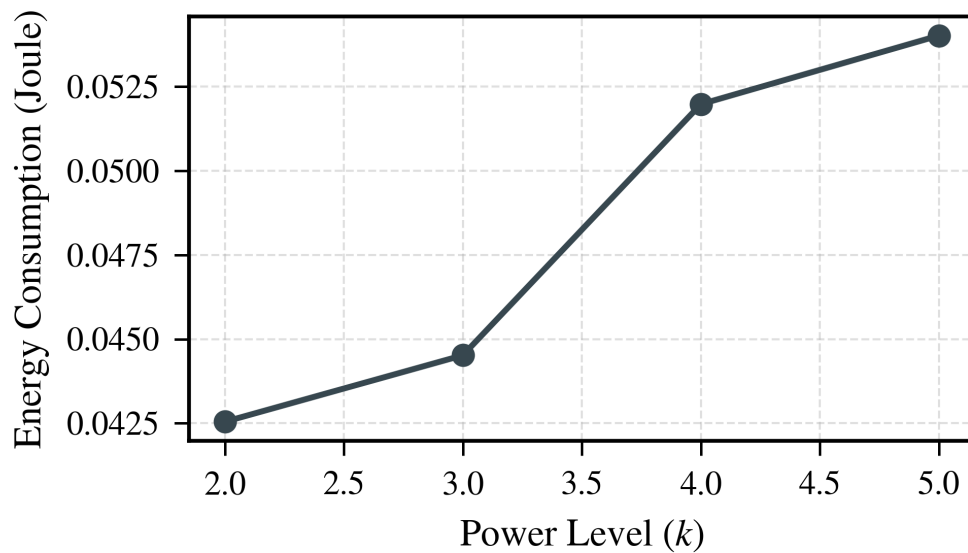


FIGURE 2.6: Average energy consumption with power levels $N = 5$, $k \in \{2, 3, 4, 5\}$

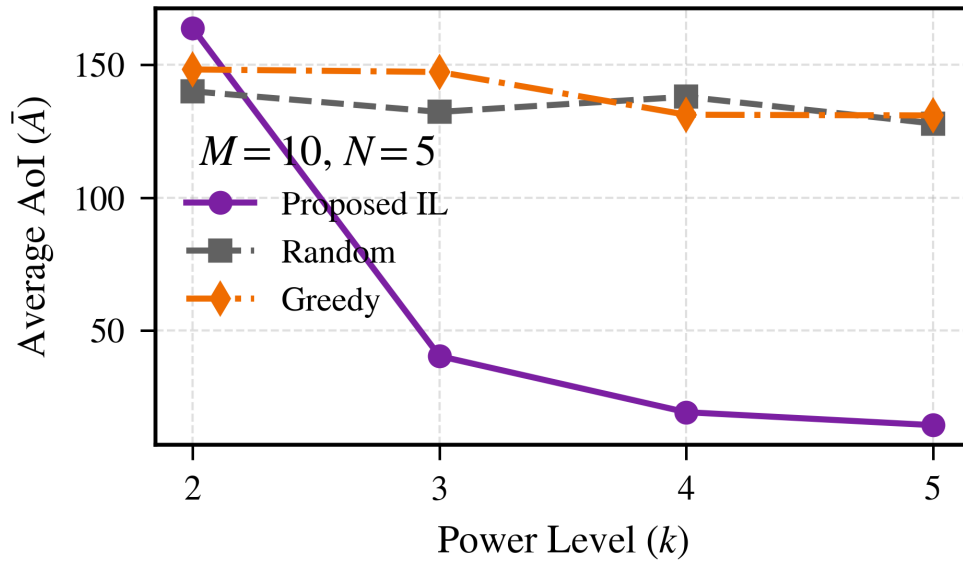


FIGURE 2.7: Comparison of EE-IL with random access and energy-based greedy algorithm.

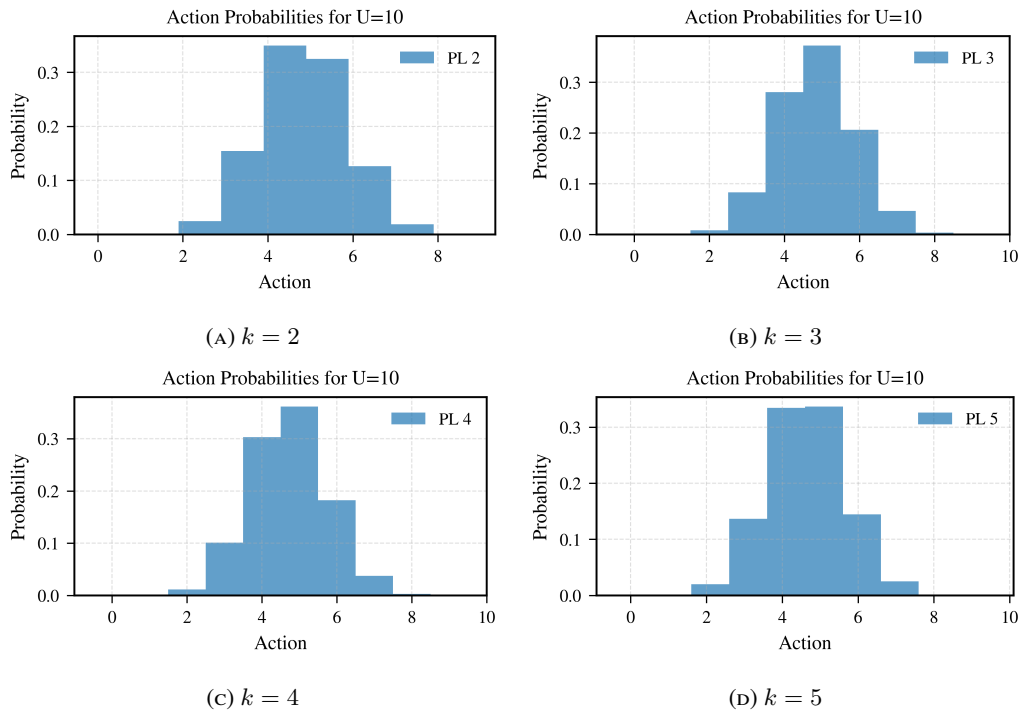


FIGURE 2.8: Optimal Replica Access Probabilities for $M=10, k=2, 3, 4, 5$

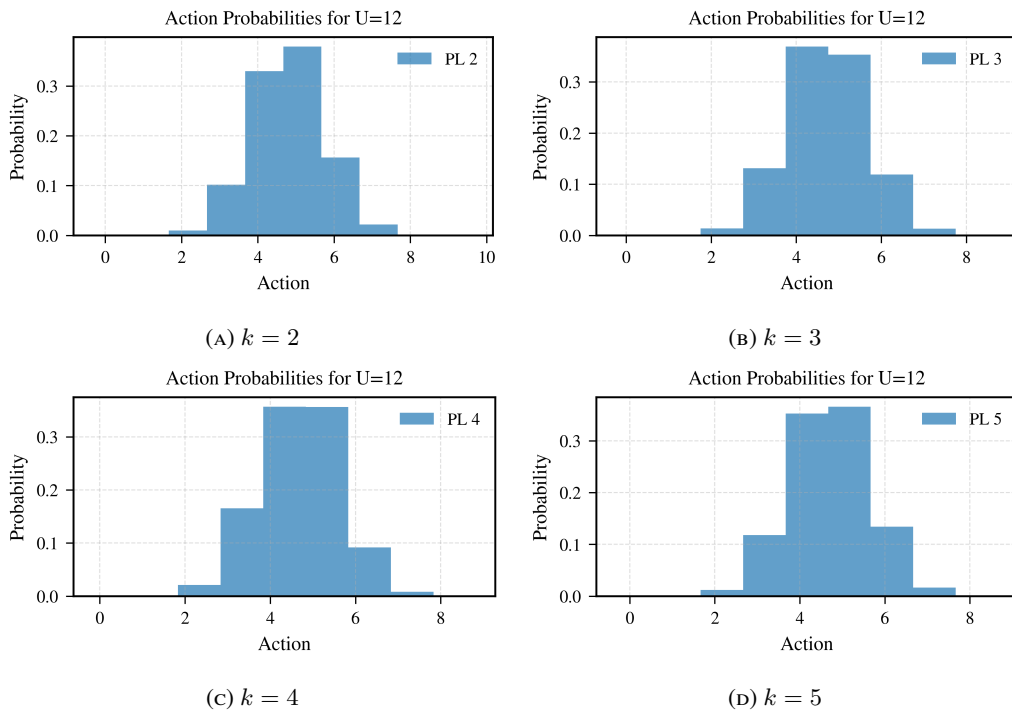


FIGURE 2.9: Optimal Replica Access Probabilities for $M = 12, k = 2, 3, 4, 5$

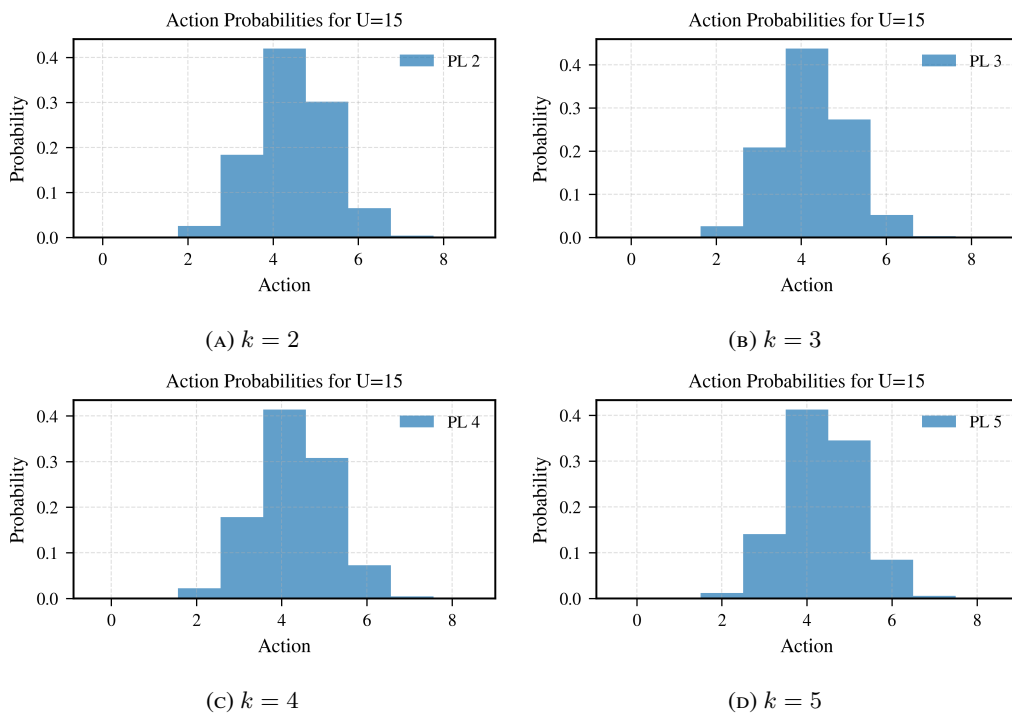


FIGURE 2.10: Optimal Replica Access Probabilities for $M = 15, k = 2, 3, 4, 5$

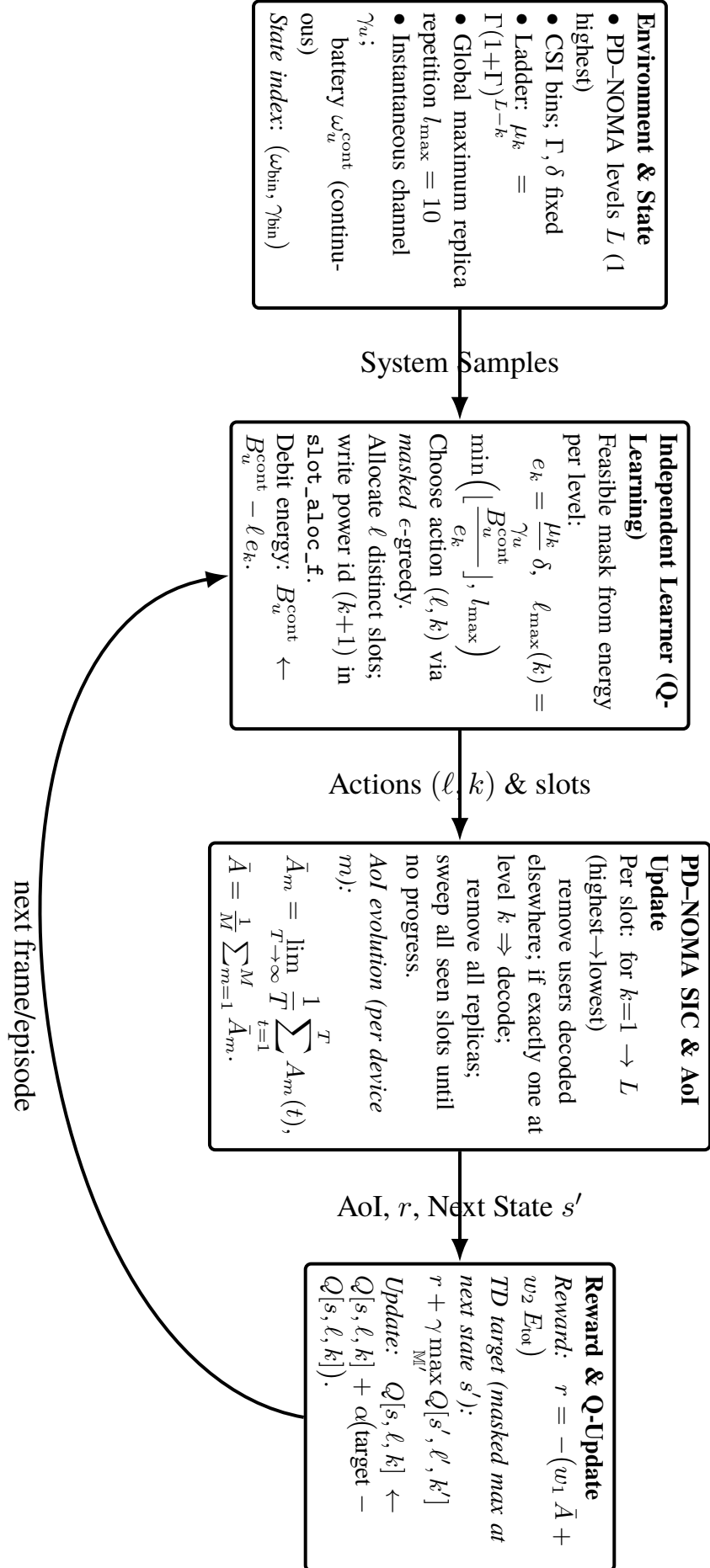


FIGURE 2.11: PD-NOMA independent-learner Q-learning: state \rightarrow masked action $(\ell, k) \rightarrow$ SIC & AoI update \rightarrow reward & Q-update; loop over time horizon.

Chapter 3

A PPO-Based PD-NOMA Scheduling Methodology for Age of Information Minimization

The ever-increasing number of devices, particularly for mMTC, demands intelligent resource allocation designs. In this chapter, each frame schedules a subset of total users and assigns power levels using the energy-efficient PD-NOMA scheme, maintaining fresh updates to minimize AoI. Moreover, we design a Partially Observable Markov Decision Process (POMDP) slot allocation policy that learns to identify devices with better success probability and schedules accordingly. The combination of both strategies maintains a steady AAoI for severe traffic gain and harsh channel conditions. Particularly, our adopted policy maintains the percentage of AAoI increases to only 12.54% when exposed to a higher traffic load. The proposed PPO algorithm maintains a steady AAoI of 108 slots at 0dB PD-NOMA decoding threshold, which is only a 4 times increase versus the 20dB increase in PD-NOMA threshold. The proposed PPO demonstrates that an efficient learning policy, coupled with minimal feedback and partial observability, can achieve scalable and stable AAoI for massive access.

3.1 Introduction

The main contribution of this chapter addresses these gaps with the following key contributions:

- We propose a lightweight scheduling framework for hybrid energy-information transfer that explicitly incorporates a sleep-scheduled two-level PD-NOMA setting.

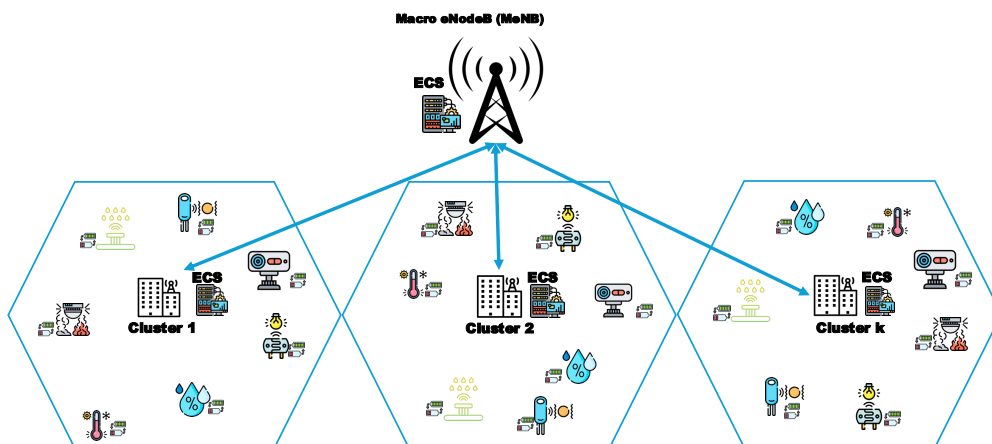


FIGURE 3.1: Caption

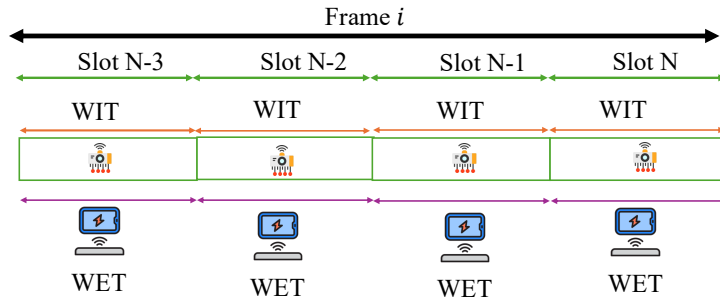


FIGURE 3.2: Frame structure of slot-based scheduling

- We make distance from the access point groups of devices, which encourages energy efficiency and enhances the successful decoding probability of distant devices.
- Our feedback design accounts for the energy-constrained nature of devices and ensures a minimum-feedback algorithm that guarantees information freshness while also considering physical layer limitations such as the coverage threshold of the access point, inter-cell interference, and energy harvesting.
- We integrate RL into the framework to adaptively optimize scheduling policies under dynamic network conditions, enabling scalable and energy-efficient operation without requiring explicit system modeling. Our policy further enhances the success probability of PD-NOMA's by intelligently allocating resources and provides the freshest data from all devices.

3.2 System Model

We consider an mMTC scenario where we divide MTCs into clusters to retrieve fresh updates. We define a set of K clusters where each cluster $k \in \{1, 2, \dots, K\}$ has a cluster head node called HAPs which is responsible for WET to sensors in the downlink and WIT in the uplink transmission. Each cluster k has radius D_{\max} and consists of M MTCs that rely on energy harvesting from HAP to transmit data. The total M MTCs in a cluster k labeled as $u_{m,k}$ belong to the set $\mathbb{U}_k = \{u_{1,k}, \dots, u_{m,k}, \dots, u_{M,k}\}$, such that $|\mathbb{U}_k| = M$. This set represents the unique ID assigned to each user, which remains unchanged regardless of whether the user is active or not. All clusters operate with a frame-based uplink transmission consisting of N slots where a slot $n \in \{1, \dots, n, \dots, N\}$. We assume that clusters are clock-synchronized with each other, so that slots start and end simultaneously. All MTCs have equal priority for data updates. A broadcast feedback signal is transmitted between the frames. The broadcast contains information about scheduled users for the next frame. We also assume that during the broadcast, HAPs transmit a designated pilot, which helps each MTCs perfectly estimate their respective CSIs $h_{m,k}^i$ and distance $d_{m,k} \in \{D_{\min}, D_{\max}\}$ from the HAP. The small-scale fading $h_{m,k}^i$ is modeled as Rician fading give as

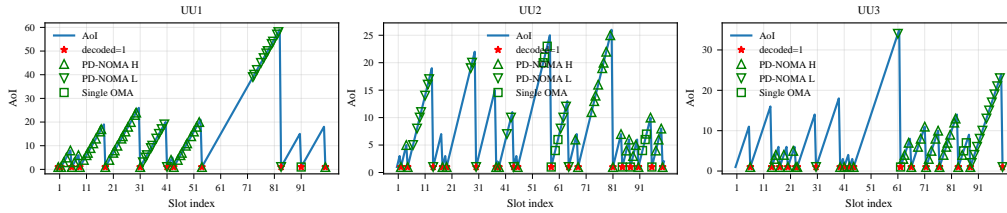


FIGURE 3.3: AoI evolution with scheduling

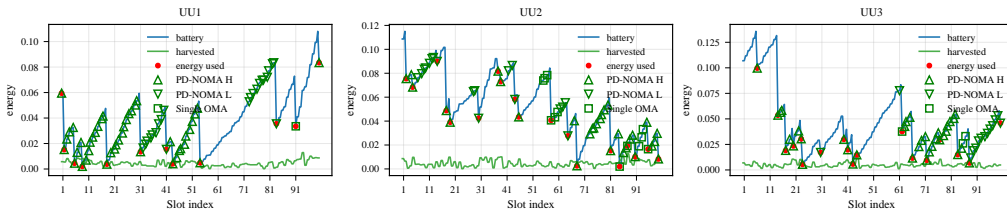


FIGURE 3.4: Energy harvesting and usage

$$h_{m,k}^i = \sqrt{\frac{\kappa}{\kappa+1}} + \sqrt{\frac{1}{\kappa+1}} \tilde{s} \in \mathcal{C}, \quad (3.1)$$

where κ is the Rician factor, and $\tilde{s} \sim \mathcal{CN}(0, 1)$ is a complex normal random variable with zero mean and unit variance. We also model large-scale fading as stretch exponential path loss (SEPL) [79] which is given as $e^{-\alpha_c d_{m,k}^{\beta_c}}$, where α_c and β_c are small adjustable parameters of SEPL model. Therefore, each MTC can compute its combined large and small-scale fading channel power

$$\gamma_{m,k}^i = e^{-\alpha_c d_{m,k}^{\beta_c}} |h_{m,k}^i|^2 \quad (3.2)$$

Each MTC transmits in PD-NOMA mode and must be assigned a differentiable power level $v \in \{v_H, v_L\}$ necessary for HAP to decode the superimposed signals. Where v_H represents the higher and v_L the lower power level, respectively. The power levels are designed to satisfy,

$$v_H = \gamma_{\text{th}}(1 + \gamma_{\text{th}}), \quad (3.3)$$

and γ_{th} is the SINR threshold the MTC must satisfy for the successful SIC decoding. Therefore, $u_{m,k}$ adjust its power as

$$P_{m,k}^i = \frac{v}{\gamma_{m,k}^i} \quad (3.4)$$

to match the desired $v \in \{v_L, v_H\}$. We assume that users are slowly moving, and therefore, their distances are updated at HAP after successful packet transmission and will remain the same until the next successful update.

The massive nature of mMTC and next-generation ultra-reliable and low-latency communication (xURLLC) suggests operating in a higher traffic gain $M > N$ regime. Under these conditions, it is clear that not all users can send their packets in each frame; therefore, the number of users allowed in each frame must be limited. To facilitate efficient scheduling, the MTCs are divided into two groups based on the distance from the HAP. Following [43], we impose a distance threshold τ such that a MTC $u_{m,k}$ belonging to k th cluster identifies as near or far device defined as

$$\mathbb{U}_k^{\text{near}} = \{u_{m,k} \mid d_{m,k} \leq \tau\} \quad (3.5)$$

and

$$\mathbb{U}_k^{\text{far}} = \{u_{m,k} \mid d_{m,k} > \tau\} \quad (3.6)$$

Here $\mathbb{U}_k^{\text{near}}$ is the set containing users which are near and $\mathbb{U}_k^{\text{far}}$ contains far users and they satisfy following conditions:

$$\mathbb{U}_k^{\text{near}} \cap \mathbb{U}_k^{\text{far}} = \emptyset, \quad \mathbb{U}_k^{\text{near}} \cup \mathbb{U}_k^{\text{far}} = \mathbb{U}_k. \quad (3.7)$$

A MTCD $u_{m,k} \in \mathbb{U}_{a,k}^{i,\text{near}}$ would transmit with power level v_H and v_L is assigned to $u_{m,k} \in \mathbb{U}_{a,k}^{i,\text{near}}$. The threshold τ is chosen to balance groups on average:

$$\mathbb{E}[|\mathbb{U}_k^{i,\text{near}}|] = \mathbb{E}[|\mathbb{U}_k^{i,\text{far}}|] \approx \frac{M}{2}, \quad (3.8)$$

which for uniform placement yields $\tau = (D_{\min} + D_{\max})/\sqrt{2}$.

Algorithm 2 Drop-and-Add MTCDs After Each Frame

Require: Allowed user sets $\mathbb{U}_{a,k}^{i,\text{near/far}}$, not-allowed user sets $\mathbb{U}_n^{i,\text{near/far}}$, and successfully decoded user sets $\mathbb{U}_s^{i,\text{near/far}}$

Ensure: Updated allowed & not-allowed user sets $\mathbb{U}_{a,k}^{i+1,\text{near/far}}$, $\mathbb{U}_n^{i+1,\text{near/far}}$, and pairing matrix $\mathbf{U}_{i+1,k}^{\text{pair}}$

- 1: $M_d^{i,\text{near/far}} \leftarrow |\mathbb{U}_s^{i,\text{near/far}}|$ ▷ Number of successful users to drop
- 2: **if** $M_d^{i,\text{near/far}} \neq 0$ **then**
- 3: $\mathbb{U}_{\text{drop}}^{i,\text{near/far}} \leftarrow \mathbb{U}_s^{i,\text{near/far}}$
- 4: $M_d^{i,\text{near/far}} \leftarrow |\mathbb{U}_s^{i,\text{near/far}}|$ ▷ Successful users this frame
- 5: $M_{\text{rep}}^{i,\text{near/far}} \leftarrow \min(|\mathbb{U}_n^{i,\text{near/far}}|, M_d^{i,\text{near/far}})$ ▷ Replace only what we can add
- 6: **if** $M_{\text{rep}}^{i,\text{near/far}} > 0$ **then**
- 7: Select $\mathbb{U}_{\text{drop}}^{i,\text{near/far}} \subseteq \mathbb{U}_s^{i,\text{near/far}}$ with $|\mathbb{U}_{\text{drop}}^{i,\text{near/far}}| = M_{\text{rep}}^{i,\text{near/far}}$ ▷ e.g., those with smallest current AoI
- 8: Select $\mathbb{U}_{\text{new}}^{i,\text{near/far}} \subseteq \mathbb{U}_n^{i,\text{near/far}}$ with $|\mathbb{U}_{\text{new}}^{i,\text{near/far}}| = M_{\text{rep}}^{i,\text{near/far}}$ ▷ e.g., highest AoI first (or all if fewer)
- 9: $\mathbb{U}_{a,k}^{i+1,\text{near/far}} \leftarrow (\mathbb{U}_{a,k}^{i,\text{near/far}} \setminus \mathbb{U}_{\text{drop}}^{i,\text{near/far}}) \cup \mathbb{U}_{\text{new}}^{i,\text{near/far}}$
- 10: $\mathbb{U}_n^{i+1,\text{near/far}} \leftarrow (\mathbb{U}_n^{i,\text{near/far}} \setminus \mathbb{U}_{\text{new}}^{i,\text{near/far}}) \cup \mathbb{U}_{\text{drop}}^{i,\text{near/far}}$
- 11: **else**
- 12: $\mathbb{U}_{a,k}^{i+1,\text{near/far}} \leftarrow \mathbb{U}_{a,k}^{i,\text{near/far}}$; $\mathbb{U}_n^{i+1,\text{near/far}} \leftarrow \mathbb{U}_n^{i,\text{near/far}}$
- 13: **end if**
- 14: **else**
- 15: Keep $\mathbb{U}_{a,k}^{i+1,\text{near/far}} = \mathbb{U}_{a,k}^{i,\text{near/far}}$
- 16: Keep $\mathbb{U}_n^{i+1,\text{near/far}} = \mathbb{U}_n^{i,\text{near/far}}$
- 17: **end if**
- 18: Combine updated near and far sets:
 $\mathbf{U}_{i+1,k}^{\text{pair}} \leftarrow$ pairwise matrix of near–far users
- 19: **if** $|\mathbb{U}_{a,k}^{i+1,\text{near/far}}| < N$ **then**
- 20: Fill vacant entries of $\mathbf{U}_{i+1,k}^{\text{pair}}$ with zeros
- 21: **end if**

In the i th frame, a MTCD $u_{m,k}$ remains silent unless the scheduler assigns a slot to it, constituting allowed and not allowed devices in far and near sets. So, the total number of allowed users in a frame can be defined as $M_a \leq 2N$ and $M_a < M$. Let $\mathbb{U}_{a,k}^{i,\text{near}} \subset \mathbb{U}_k^{\text{near}}$ and $\mathbb{U}_{a,k}^{i,\text{far}} \subset \mathbb{U}_k^{\text{far}}$ denote the sets of **allowed near-MTCD IDs** and **allowed far-MTCD IDs** in frame i , respectively, such that $|\mathbb{U}_{a,k}^{i,\text{near}}| + |\mathbb{U}_{a,k}^{i,\text{far}}| \leq M_a$. The number of user IDs that are not allowed to access this frame $M_n = M - M_a$, are collected in two sets of near and far users, such that $\mathbb{U}_n^{i,\text{near}} = \mathbb{U}_k \setminus \mathbb{U}_{a,k}^{i,\text{near}}$, and $\mathbb{U}_n^{i,\text{far}} = \mathbb{U}_k \setminus \mathbb{U}_{a,k}^{i,\text{far}}$; the sets of **not allowed far and near users**. A matrix $\mathbf{U}_{i,k}^{\text{pair}} \in \mathbb{Z}^{N \times 2}$ contains pairs of near and far MTCD, each assigned v_H and v_H levels respectively. Each row $j \in 1, \dots, J$, with $J = N$ contains a pair vector $\mathbf{u}_{j,k}^{\text{pair}}$. The transmission sequence of each user pair directly influences its AoI. This way ensures that each slot receives a packet from the two sets of far and near MTCDs. At the end of each frame i , we broadcast the information of allowed users, not allowed users, and their assigned power levels as a vector of tuples $\mathbf{f}_k^i \in \mathbb{Z}^{M_a}$ where each tuple contains a user id $u_{m,k}$, a slot assigned to that user $s_{m_a,k}^i \in \{0, 1, \dots, N\}$ in current frame i , with $s_{m_a,k} = 0$ indicating that no slot is assigned or MTCD considers itself as not allowed user. We can define \mathbf{f}_k^i as

$$\mathbf{f}_k^i = \{(u_{1,k}, s_{1,k}^i, v), \dots, (u_{m,k}, s_{m,k}^i, v), \dots, (u_{M,k}, s_{M,k}^i, v)\}. \quad (3.9)$$

A received signal in slot $s_{m,k}^i$ of cluster k is subject to interference from the signal transmitted in the same slot from other clusters $\forall l \neq k \in \{1, 2, \dots, K\}$ i.e. $s_{m,k}^i = s_{m,l}^i$, therefore MTCD's interference is caused by the user of other clusters which are assigned same slot. Additionally, in a slot $s_{m,k}^i$, a user $u_{m_a,k} \in \mathbb{U}_{a,k}^{i,\text{near}}$ assigned v_H also receives a signal from a user $u_{m'_a,k} \in \mathbb{U}_{a,k}^{i,\text{far}}$ with power v_L . We define the desired superimposed signal at slot $s_{m,k}$ of frame i , at HAP of cluster k as

$$y_d^i(s_{m,k}^i) = \sqrt{P_{m,k}^i} x_{m,k}^i h_{m,k}^i + \sqrt{P_{m',k}^i} x_{m',k}^i h_{m',k}^i, \quad (3.10)$$

where $x_{m,k}^i$ and $x_{m',k}^i$ are signals of users $u_{m_a,k}$, and $u_{m'_a,k}$ respectively. The interference experienced by the desired signal is from slot $s_{m,l}^i = s_{m,k}^i$, from is given as

$$\mathcal{I}_l(s_{m,k}^i) = \sum \sqrt{P_{m,l}^i} x_{m,l}^i h_{m,l}^i + \sum \sqrt{P_{m',l}^i} x_{m',l}^i h_{m',l}^i, \forall \quad (3.11)$$

while the final received signal for decoding at slot $s_{m,k}$ of HAP k subject to interference \mathcal{I}_l and noise $w_{m,k}^i$ is given as

$$y_{m,k}^i(s_{m,k}^i) = y_d^i(s_{m,k}^i) + \mathcal{I}_l(s_{m,k}^i) + w_{m,k}^i. \quad (3.12)$$

We perform SIC following the standard PD-NOMA principle: the user with higher power is decoded first, subtracted from the combined signal, revealing the lower-power user. Since $u_{m,k}$ is assigned v_H , the SINR of the higher-power MTCD is

$$\text{SINR}_{m,k}^i = \frac{v_H}{v_L + \mathcal{I}_l + w_{m,k}^i}. \quad (3.13)$$

To achieve successful decoding, the SINR must satisfy $\text{SINR}_{m,k}^i \geq \gamma_{\text{th}}$. After decoding, the higher user's contribution is canceled, and the SINR of the lower-power MTCD $u_{m',k}$ is expressed as

$$\text{SINR}_{m',k}^i = \frac{v_L}{\mathcal{I}_l + w_{m,k}^i}. \quad (3.14)$$

Similarly, successful decoding requires $\text{SINR}_{m',k}^i \geq \gamma_{\text{th}}$. Once the complete frame is received and successfully decoded users are identified, the total number of successful user IDs $M_s^{i,\text{far}}$, $M_s^{i,\text{near}}$ from $\mathbb{U}_{a,k}^{i,\text{near}}$ and $\mathbb{U}_{a,k}^{i,\text{far}}$ in the particular frame " i " belongs to the sets $\mathbb{U}_s^{i,\text{near}} \subseteq \mathbb{U}_a^{i,\text{near}}$, $\mathbb{U}_s^{i,\text{far}} \subseteq \mathbb{U}_a^{i,\text{far}}$. We drop all successful MTCDs from the current frame and store them in $\mathbb{U}_n^{i,\text{far}}$, and $\mathbb{U}_n^{i,\text{near}}$ depending on their updated respective distances. Finally, to satisfy $|\mathbb{U}_{a,k}^{i,\text{near}}| + |\mathbb{U}_{a,k}^{i,\text{far}}| \leq M_a$, sets are updated and MTCDs from previously $\mathbb{U}_n^{i,\text{far}}$, and $\mathbb{U}_n^{i,\text{near}}$ sets are included in the $\mathbb{U}_a^{i,\text{near}}$, and $\mathbb{U}_a^{i,\text{far}}$ to be scheduled in next frame. The newly constituted sets are paired as far and near users to form a matrix $\mathbf{U}_{i,k}^{\text{pair}} \in \mathbb{Z}^{N \times 2}$. This ensures perfect SIC decoding in uplink, subject to SINR threshold and battery condition. The scheme also considers the low-energy nature of far users, who are further away from the harvesting source, ensuring lower battery outage. Although enough users are available in both groups to make pairs, in case the number of users in one group falls short of N , $\mathbf{U}_{i,k}^{\text{pair}}$ is assigned a zero at unfulfilled places. Algorithm 2 summarizes the method of user updates. Figure 3.3 shows a complete flow of assigned users and their successful/unsuccessful updates.

3.2.1 Energy Harvesting Model

Define MTCD's battery in each frame $\omega_{m,k}^i$, we recharge each of them using a nonlinear energy harvesting model [36]. We adopt a WET model [39] where the user harvests energy

through WET in each slot of duration δ_{wet} via a dedicated channel, except for their corresponding transmission scheduled slot. Therefore, given the channel gain and the transmission power of HAP P_{HAP} , the general representation of the non-linear energy harvesting model is given as

$$E_{m,k}^i(n) = \frac{\alpha_0 P_{\text{HAP}} \delta_{\text{wet}} \gamma_{m,k}^i}{\alpha_1 P_{\text{HAP}} \gamma_{m,k}^i + \alpha_1}, \quad (3.15)$$

where α_1, α_0 are energy harvesting model parameters. Each user receives energy from HAP in its dedicated slot before UL transmission. We define indicator functions to define MTCD's battery evolution, indicating that it has sufficient energy, and SINR for transmission as

$$\mathcal{D}_{m,k}^A(i) = \mathbb{1} \left\{ n = s_{m,a,k}^i, \text{SINR}_{m,k}^i \geq \gamma_{\text{th}}, \omega_{m,k}^i \geq P_{m,k}^i \delta_{\text{wit}} \right\}. \quad (3.16)$$

All MTCDs harvest energy throughout the slots except the slot they are scheduled. Given that each MTCD has a maximum battery capacity ω_{max} , the energy consumption model can be given as

$$\omega_{m,k}^i(n) = \begin{cases} \min\{\omega_{m,k}^i(n) - P_{m,k}^i \delta_{\text{wit}}, \omega_{\text{max}}\}, & \mathcal{D}_{m,k}^A(i) = 1, \\ \min\{\omega_{m,k}^{i-1} + E_{m,k}^i, \omega_{\text{max}}\}, & \mathcal{D}_{m,k}^A(i) = 0, \end{cases} \quad (3.17)$$

Where ω_{max} is the maximum battery capacity of MTCD. Figure 3.4 shows the complete energy harvesting and consumption flow of devices.

3.2.2 Age of Information

We denote the current AOI of the $u_{m,k}$ user ID in the i -th frame at n th slot as $A_{m,k}^i(n)$. The AoI keeps on increasing until the user attempts its uplink transmission and is recovered by successful SIC while also satisfying the conditions $\text{SINR}_{m,k}^i \geq \gamma_{\text{th}}$, and $\omega_{m,k}^i \geq P_{m,k}^i \delta$. Therefore, the AoI indicator function can be defined as

The definition of AOI can be presented as

$$A_{m,k}^i(n) = \begin{cases} 1 & \text{if } \mathcal{D}_{m,k}^A(i) = 1 \\ A_{m,k}^i(n-1) + 1, & \text{if } \mathcal{D}_{m,k}^A(i) = 0. \end{cases} \quad (3.18)$$

We can define for the total frames I , each with N slots, and over a time horizon $T = I.N$ the AAOI of the m th user is given by

$$\bar{A}_{m,k} = \lim_{T \rightarrow \infty} \frac{1}{T} \sum_{i=1}^I \sum_{n=1}^N A_{m,k}^i(n). \quad (3.19)$$

While the system's average age of information is given by

$$\bar{A} = \frac{1}{M} \sum_{m=1}^M \bar{A}_{m,k}. \quad (3.20)$$

3.3 Partially Observable Markov Decision Process

Scheduling in large-scale, low-power IoT networks is inherently stochastic due to uncertain energy availability and dynamic channel conditions. These challenges make model-based solutions such as Markov Decision Processes (MDPs) difficult to apply, as exact transition

probabilities are hard to derive. Instead, we model the scheduling problem as a POMDP and solve it using PPO. POMDP is defined by the tuple

$$\mathcal{M} = (\mathcal{S}, \mathcal{A}, \mathcal{T}, \mathcal{R}, \gamma),$$

where \mathcal{S} is the set of states of the current pairs vector $\mathbf{U}_{i,k}^{\text{pair}}$ under consideration for the decision of slot assignment. The state contains AoI $\mathbf{A}_{j,k}^i$, the change in AoI $\Delta_{j,k}^i$ since the last time users were scheduled, distance $\mathbf{d}_{j,k}$, last known energy status $\mathbf{E}_{j,k}^*$, and slots passed since the last time scheduled $\ell_{j,k}^\dagger$ vectors of the considered pair. We also define the success probability of each user and an overall network success history window to provide the partial observability for each decision. Let $p_{m,k}^i \in [0, 1]$ denotes the per-user success-belief at frame i for user $u_{m,k}$. With a smoothing factor $\alpha_s \in (0, 1)$ and decoded indicator $\chi_u^{i-1} = \mathbb{1}\{\text{user } u_{m,k} \text{ decoded successfully at frame } i-1\}$. The belief is updated as

$$p_{m,k}^i = \alpha_s p_{m,k}^{i-1} + (1 - \alpha_s) \chi_{m,k}^{i-1}. \quad (3.21)$$

The global success-belief for frame i is the average across all M_{total} users:

$$\phi^i = \frac{1}{M} \sum_{m=1}^M b_{m,k}^i. \quad (3.22)$$

The state includes the H -length history window $\mathbf{W}_s^i = [\phi^{i-1}, \phi^{i-2}, \dots, \phi^{i-H}]$, which provides a partial observability context for the decision at frame i for the pair. A convenient shift form is

$$\mathbf{W}_s^i = [\phi^{i-1}, \phi^{i-1}, \dots, \phi^{i-H}]. \quad (3.23)$$

We define $\mathbf{W}_s \in \mathbb{R}^{1 \times H}$ as the probability of success history window of the previous H frames to provide the partial observability to the current action selection.

So the complete states for a pair are defined as

$$\mathbf{A}_{j,k}^i \triangleq (A_{j,k}^{i,\text{near}}(1), A_{j,k}^{i,\text{far}}(1)), \quad (3.24)$$

$$\Delta_{j,k}^i \triangleq (\Delta_{j,k}^{i,\text{near}}, \Delta_{j,k}^{i,\text{far}}), \quad (3.25)$$

$$\mathbf{d}_{j,k}^i \triangleq (d_{j,k}^{i,\text{near}}, d_{j,k}^{i,\text{far}}), \quad (3.26)$$

$$\mathbf{E}_{j,k} \triangleq (\omega_{j,k}^{\text{near}}, \omega_{j,k}^{\text{far}}), \quad (3.27)$$

$$\ell_{j,k} \triangleq (\ell_{j,k}^{\text{near}}, \ell_{j,k}^{\text{far}}), \quad (3.28)$$

$$\mathbf{p}_{j,k} \triangleq (p_{j,k}^{\text{near}}, p_{j,k}^{\text{far}}), \quad (3.29)$$

$$\mathbf{W}_s^i \triangleq [\phi_s^{i-1}, \phi_s^{i-2}, \dots, \phi_s^{i-H}] \in \subseteq [0, 1]^H. \quad (3.30)$$

The final state for the user pair at the beginning of frame $(i+1)$ is expressed as:

$$S_{j,k}^i = \{\mathbf{A}_{j,k}^i, \Delta_{j,k}^i, \mathbf{d}_{j,k}^i, \hat{\mathbf{E}}_{j,k}, \ell_{j,k}, \mathbf{p}_{j,k}, \mathbf{W}_s^i\}. \quad (3.31)$$

*More sophisticated models such as LSTM [80] can be adopted to estimate the energy of each device when the actual energy is impossible to observe. Nevertheless, the inclusion of previously observed energy does not directly affect the main objective of AoI minimization.

†The change in AoI and slots passed since the last time device was scheduled are different. For instance, a user can have change in AoI $50 - 10 = 40$ for 10 slots passed since the last time it was scheduled.

At the system level, the joint state at the end of frame i is represented as:

$$\mathbf{S}^i = [S_{1,k}^i, S_{2,k}^i, \dots, S_{j,k}^i, S_{N,k}^i]. \quad (3.32)$$

\mathcal{A} : action space, defined as all valid slot assignment vectors \mathbf{f}_k^i , \mathcal{T} is the transition probabilities $\mathcal{P}(s'|s, a)$, unknown to the agent, and R is the reward function.

Given this POMDP, we adopt **Proximal Policy Optimization (PPO)** to learn a policy

$$\pi : \mathcal{S}^i \rightarrow \mathbf{f}_k^i,$$

that maps the current observation \mathcal{O}^i in frame i to a slot assignment vector \mathbf{f}_k^i , which can maximize the over reward $\sum_{t=0}^{\infty} \gamma^{t-1} \mathcal{R}(t)$ over time horizon $t \in [0, T]$ with discount factor γ .

Finally, we design the reward as an incentive function that encourages the PPO to ensure each allowed pair of users is updated efficiently in every frame. The reward is given as negative AoI since we aim to minimize it; therefore, we have

$$r_{j,k}^i(n) = -j_s (w_n A_{j,k}^{i,near}(n) + w_f A_{j,k}^{i,far}(n)) \quad (3.33)$$

Here $n = s_{m_a,k}^i$ represents the pair's scheduled slot, and w_n, w_f are the weights for near and far users, respectively. $A_{j,k}^{i,near}$ and $A_{j,k}^{i,far}$ are the AoI of users scheduled for current slot, while the reward $j_s = -w_s s_{m_a,k}^i$ further shapes the slot assignment policy. The complete reward per frame is $\mathbf{R}^i \in \mathbb{R}^{N \times 1}$. So our problem can be defined as

$$\min_{\pi} \bar{A} \quad (3.34)$$

$$\text{s.t. } C_1 : \mathbf{U}_{j,k}^{\text{pair}} \in \mathbb{Z}^{N \times 2} \quad (3.35)$$

$$C_2 : \forall \mathcal{D}_{m,k}^A(i) = 1 \quad (3.36)$$

$$C_3 : N < M \quad (3.37)$$

$$(3.38)$$

where the constraint C_1 ensures devices are in-scheduled while C_2 , ensures battery, SINR threshold, and scheduling conditions are matched. While C_3 ensures short sleep cycles and regular updates of MTCDs, pushing for more efficient decisions.

3.3.1 Proximal Policy Optimization (PPO)

The PPO utilizes a clipped surrogate loss that constrains the policy update to prevent large deviations from the previous policy:

$$L^{\text{CLIP}}(\theta) = \mathbb{E}_t \left[\min \left(r_t(\theta) \hat{A}_t, \text{clip}(r_t(\theta), 1 - \epsilon, 1 + \epsilon) \hat{A}_t \right) \right], \quad (3.39)$$

where $r_t(\theta) = \frac{\pi_{\theta}(a_t|s_t)}{\pi_{\theta_{\text{old}}}(a_t|s_t)}$ is the probability ratio between the new and old policies, and ϵ is the clipping range constant. The policy parameters are updated by maximizing the total PPO objective:

$$L_{\text{total}}(\theta) = L^{\text{CLIP}}(\theta) - L^{\text{VF}}(\theta) + S[\pi_{\theta}], \quad (3.40)$$

Algorithm 3 Procedure of the proposed PPO-based Scheduling

```

1: Input:  $R, I, M, N, \pi, \gamma_{\text{th}}, \nu$ , PPO hyperparameters
2: Initialize: User states, PPO policy  $\pi$ , optimizer
3: for each episode  $o$  to  $O$  do
4:   Initialize rollout buffer  $\mathcal{B} \in \mathbb{R}$ 
5:   for each frame  $i = 1$  to  $I$  do
6:     Select  $\mathbb{U}_{a,k}^{i,\text{near}}$  and  $\mathbb{U}_{a,k}^{i,\text{far}}$  using Alg. 2
7:     Update user pair matrix  $\mathbf{U}_{i,k}^{\text{pair}} \in \mathbb{Z}^{N \times 2}$ 
8:     for each user pair  $\mathbf{u}_{j,k}^{\text{pair}} \in \mathbf{U}_{i,k}^{\text{pair}}$  do
9:       Observe  $\mathbf{S}_{j,k}^i$ 
10:      Select action & assign slot in  $\mathbf{f}_k^i$  with policy  $\pi$ 
11:      Update  $\mathbf{S}_{j,k}^i$  to  $\mathbf{S}^i$ 
12:    end for
13:     $\forall u_{m,k} \in \mathbb{U}_n^{i,\text{near}} \cup \mathbb{U}_n^{i,\text{far}}$  update  $\mathbf{f}_k^i$  with  $s_{m,k} = 0$ 
14:    Broadcast  $\mathbf{f}_k^i$ 
15:    Decode slots and update AoI for users  $u_{m,k} \in \mathbf{U}_k$ 
16:    Compute rewards using Eq. 3.33 and update  $\mathbf{R}^i \in \mathbb{R}^{N \times 1}$ 
17:    Update user pool via Algorithm 2
18:    Store  $\mathbf{S}^i, \mathbf{f}_k^i$ , and  $\mathbf{R}^i$  in buffer  $\mathcal{B}$ 
19:  end for
20:  Train PPO: Use GAE and clipped loss over multiple epochs
21: end for

```

where L^{VF} is the value function loss, $S[\pi_\theta]$ is the policy entropy encouraging exploration. Each policy update performs the following parameter changes

$$\theta \leftarrow \theta + \eta \nabla_{\theta} L_{\text{total}}(\theta), \quad (3.41)$$

where η is the learning rate. Our scheduling algorithm, along with training the PPO for efficient scheduling, is presented in Algorithm 3.

3.4 Numerical Results

For the numerical evaluation, we implement a neural network (NN) architecture within a customized PPO framework, described in Algorithm 3. Table 3.1 represents the key simulation parameters for PPO and physical characteristics that are simulated.

Figure 3.5 represents the convergence of our algorithm for 100 episodes through the sum of rewards in each episode. We can observe the efficiency of the algorithm through excellent convergence as the traffic load increases with the number of devices.

In Figure 3.6, a comparison with the different scheduling schemes, specifically the threshold-based scheme [35], shows a clear advantage of learning the stochastic nature of the channel, energy harvesting, and battery outage effects. The proposed PPO significantly reduces AoI. Our results demonstrate the importance of the combination of several key points of AAOI reduction. It utilizes a sleep-wake schedule cycle, placing the highest AoI devices at the start of frame, keeping frame length appropriate, and learning to incorporate environmental effects into scheduling decisions.

The significance of learning non-controllable interference and energy efficiency is further evident from Figure 3.7. We introduce variation in γ_{th} as it compositely represents the channel severity and energy efficiency. Results demonstrate that for $\gamma_{\text{th}} = -20\text{dB}$, the best strategy

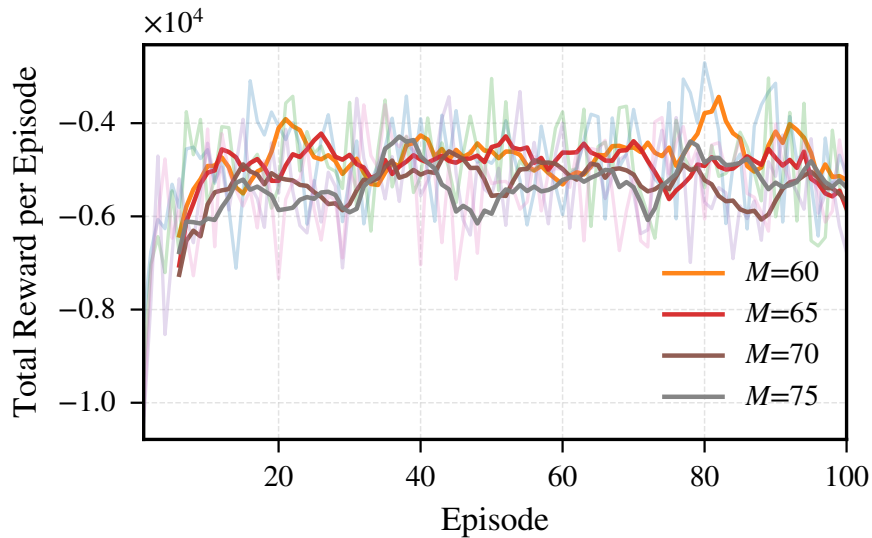
FIGURE 3.5: Reward convergence vs. episodes, $N = 15$, $\gamma_{\text{th}} = -5$ dB.

TABLE 3.1: Simulation and Training Parameters

Parameter	Value	Parameter	Value
D_{max}	20 meter	D_{min}	8 meter
ω_{max}	0.1 Joule	P_{HAP}	2 W
$\delta_{\text{WET}} = \delta_{\text{WIT}}$	$3\text{e-}4$ s	τ	12
Optimizer	Adam	γ	0.99
η	$3\text{e-}4$	Clip range (ϵ)	0.1
Initial Entropy coeff.	0.03	Batch size	200
Epochs	4	Frames/episode	200
Episodes	100	w_s	0.5
w_n	1	w_f	0.2
α_c	0.25	β_c	0.94
α_0	0.826	α_1	0.399
K	3	κ	12

proposed PPO learns is to schedule greedily. The optimal performance gap between all compared policies is not significant. However, as the conditions get tough with $\gamma_{\text{th}} = -5, 0\text{dB}$, the proposed PPO' superior performance becomes more evident and the gap between policies widens.

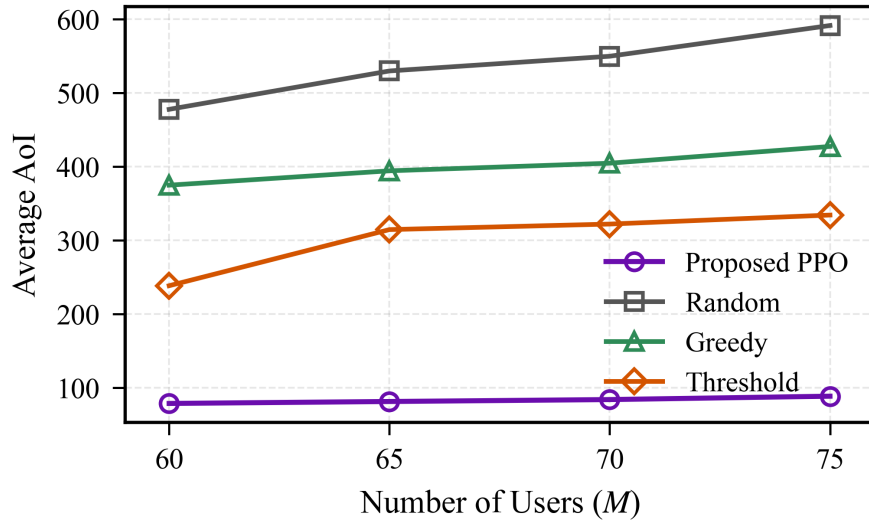


FIGURE 3.6: Average AoI vs. M , $N = 15$, $\gamma_{th} = -5$ dB.

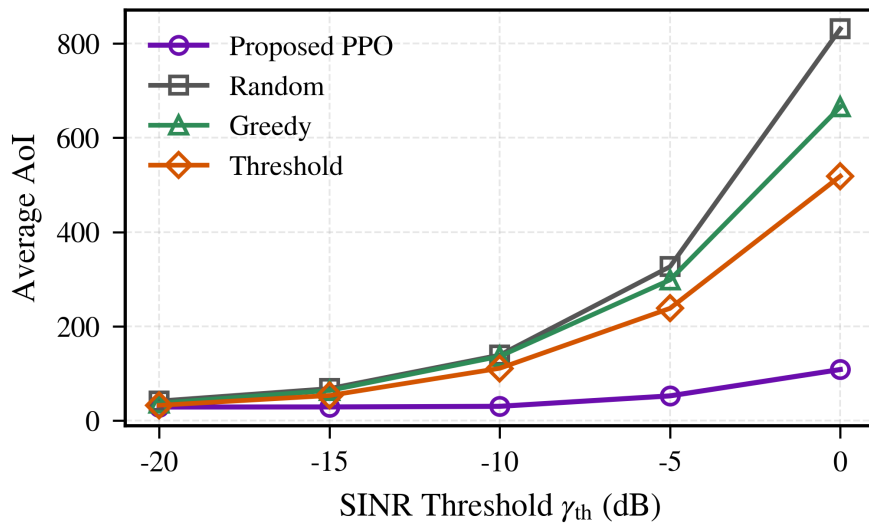


FIGURE 3.7: Average AoI vs. γ_{th} , $M = 60$, $N = 15$.

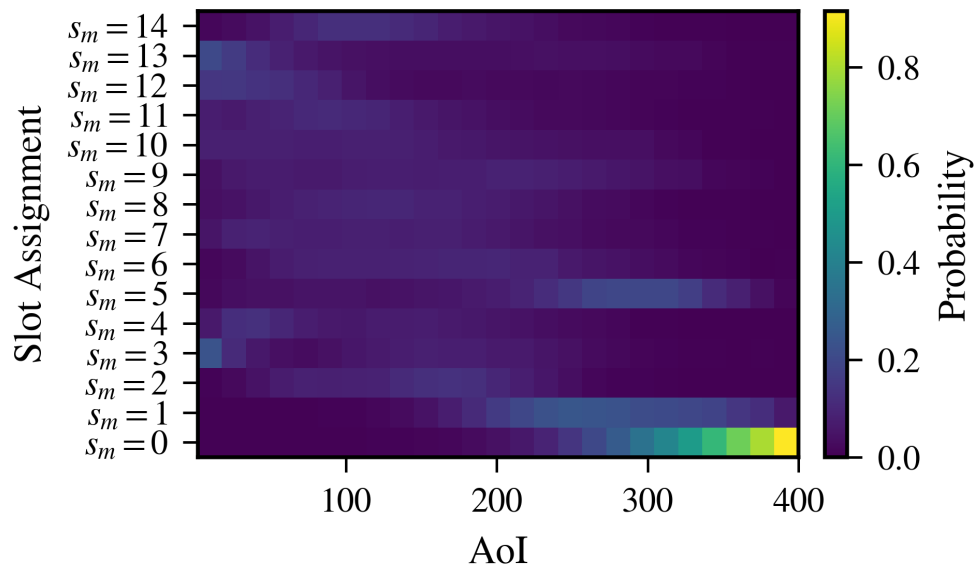


FIGURE 3.8: Example of policy converging to greedy strategy under good conditions with $\gamma_{\text{th}} = -20\text{dB}$

Chapter 4

Maximizing Entanglement Rate with Latency Constraint for Global Quantum Internet using LEO Satellites

4.1 Introduction

The advent of quantum communication technologies is building the way for the development of the quantum internet [57], a global quantum network that provides a promising platform for ground-breaking quantum applications, such as secure communication known for quantum key distribution [81], distributed quantum computing [82], and high-precision quantum sensing [83]. At the core of the quantum internet is the use of probabilistic quantum bits (qubits), which enable inherently secure data transmission by leveraging fundamental principles of quantum mechanics such as entanglement, teleportation, and swapping. These principles form the foundation for quantum communication, enabling nodes to interact across globally distributed subnetworks and supporting active quantum information exchange. Motivated by the limitations of ground-based quantum networks in achieving global scalability, the present work introduces an extended architecture of the quantum network referred to as the Hybrid Quantum Information Network (HQIN) which integrates satellite-based quantum communication to facilitate long-distance entanglement distribution and enhance the reliability of quantum connectivity [60], [61]. In the presented architecture, satellites act as intermediaries, connecting globally distributed quantum subnetworks by distributing entangled qubits (ebits) to their respective head nodes, responsible for establishing and maintaining entangled links with the satellites. Building on these considerations, the present work prioritizes operations based on the dominant resource requirements fidelity and latency of each active connection, addressing their inherent trade-off to improve overall network performance.

However, despite the promising potential of HQINs, achieving an effective balance between fidelity and latency remains a major challenge. Fidelity defined in terms of how well a quantum state is preserved in the presence of noise and other disturbances, serving as a key metric for quantifying the closeness of a mixed state to the intended pure state. On the other hand, latency refers to the time required to prepare users for quantum information exchange [84]. In networks comprising multiple quantum nodes, enhancing fidelity relies heavily on **entanglement purification**, primarily performed by quantum repeaters (QRs). Those play a crucial role in maintaining high-quality entanglement over long distances within ground-based subnetworks by mitigating the effects of noise and decoherence. Prior to executing entanglement swapping, QRs enhance the distributed entangled pairs by using other low-fidelity pairs as sacrificial pairs through entanglement purification, thereby improving the overall quality of entanglement across the network. This step is crucial, as entanglement

swapping alone degrades the fidelity due to the accumulation of operational errors. By performing both purification and swapping, quantum repeaters enable the extension of entangled links over distances [85] that would otherwise be infeasible, overcoming the limitations imposed by the no-cloning theorem, which prohibits the direct replication of quantum information. Moreover, managing latency instead remains a critical challenge in HQINs, as dynamic network conditions such as satellite visibility windows, queuing delays, and synchronization requirements can substantially hinder communication efficiency. These factors, coupled with the inherent delays from core operational processes, pose a significant barrier to achieving reliable, high-throughput quantum communication on a global scale.

The present work focuses on the trade-off between the maximum achievable fidelity and the minimal attainable latency in a quantum network with a diamond topology, incorporating satellite communication to extend entanglement distribution over long distances. In pursuit of this goal, we formulate an **optimization problem** for computing the maximum achievable fidelity while satisfying constraints on minimum latency between arbitrary pairs of communication users within the network. Our design specifically targets the first generation (1G) of quantum subnetworks, where quantum error correction (QEC) codes are not yet available. In this context, we consider a subnetwork architecture built with quantum repeaters [86], which enable entanglement distribution through the process of entanglement swapping. Therefore, communication relies on imperfectly entangled and purified photon pairs, ultimately introducing noise to the whole process. Notably, entanglement purification is not equivalent to quantum error correction (QEC), which involves the active detection and correction of quantum errors such as bit-flip, phase-flip, and depolarizing noise in quantum states. In contrast, entanglement purification is performed after the transmission of ebits to improve their fidelity. Furthermore, regarding the connection between different subnetworks, satellite-based quantum links provide a promising opportunity to establish high-fidelity connections over distances of hundreds of kilometers. This is particularly important because quantum communication over optical fibers faces significant technological constraints, notably exponential photon loss with distance, which severely limits the scalability of ground-based quantum networks.

As a result, satellite-based connections emerge as a crucial solution for extending the communication range since the photon losses in vacuum scale are only polynomial with the distance compared to the exponential losses in optical fibers, enabling end-to-end quantum communication between source and destination nodes. Furthermore, for the interconnection of different subnetworks, we consider satellite constellations, such as Low Earth Orbit (LEO) systems like Starlink, as a promising opportunity to establish high-fidelity quantum links between subnetworks separated by hundreds of kilometers. Unlike fiber-optic channels, which suffer from exponential photon loss over long distances due to attenuation, satellite-based links experience only polynomial scaling of photon losses with distance. This makes satellite communication a critical enabler for realizing end-to-end quantum communication across geographically dispersed nodes. To date, the scientific community has explored satellite-based quantum networks as a means to extend communication distances [87], [88]. In most of the aforementioned works, the satellite primarily serves as an ebit quantum source for the pair of subnetwork head nodes engaged in communication. However, this approach exhibits limitations in achievable distance, as demonstrated by the Micius satellite [60], which verified entanglement distribution over distances of up to approximately 1,200 km. Consequently, achieving greater distances between subnetwork head nodes using conventional methods becomes impractical.

We propose a model in which a satellite, functioning as a free-space quantum source, distributes entangled qubits by transmitting one qubit to the head node of each subnetwork while storing the entangled counterpart in onboard quantum memory. This architecture facilitates the establishment of entanglement among geographically distributed subnetworks. Entangled photon pairs are generated via Spontaneous Parametric Down-Conversion (SPDC) [89],

wherein a high-frequency laser interacts with a nonlinear crystal such as beta barium borate (BBO) to produce pairs suitable for quantum linking over long distances. We employ Low Earth Orbit (LEO) satellites due to their optimal trade-off between lower latency and broader ground coverage. However, their rapid orbits (approximately 120 minutes per revolution) limit continuous connectivity. To address this, we adopt a **satellite constellation approach**, inspired by large-scale networks such as Starlink, where multiple synchronized LEO satellites ensure uninterrupted global coverage and support consistent entanglement delivery across distributed subnetworks. A significant challenge in this setup is *differential latency* [90], where variations in photon transmission times from the satellite to different ground nodes can impede/hinder timely entanglement swapping. Successful entanglement swapping requires that entangled qubits arrive within a strict coherence window, accounting for delays introduced by both transmission and memory retrieval. To mitigate this, **precise synchronization** among subnetwork nodes is essential. Without coordinated timing, entanglement swapping cannot proceed, leading to the degradation of both fidelity and latency two core performance metrics in quantum communication. To maintain timing integrity across the network, our architecture employs Central Controllers that orchestrate node operations. The main adopted abbreviations of this paper are summarized in the following table 4.1.

TABLE 4.1: Abbreviations

Abbreviation	Full Name
APC	Auto Polarization Compensator
CPDC	Classical Path Discovery and Coordination
ebits	Entangled Qubits
EGL	Entanglement Generation Latency
EPR	Einstein-Podolsky-Rosen Pair (Entangled Qubits)
ESL	Entanglement Swapping Latency
HQIN	Hybrid Quantum Information Network
KPI	Key Performance Indicator
LEO	Low Earth Orbit
QBER	Quantum Bit Error Rate
Qbits	Quantum Bits
QEC	Quantum Error Correction
QKD	Quantum Key Distribution
QM	Quantum Memory
QR	Quantum Repeater
SPDC	Spontaneous Parametric Down-Conversion

4.2 BACKGROUND

This section first reviews the fundamental knowledge behind the modeling of the HQIN and subsequently presents the key assumptions adopted throughout the paper.

4.2.1 Entanglement Generation

The process of distributing entangled pairs between remote quantum nodes is known as entanglement generation. As in other quantum networking paradigms, efficient entanglement generation is essential for establishing reliable quantum links, which are fundamental for subsequent quantum information exchange. Multiple entanglement generation schemes have

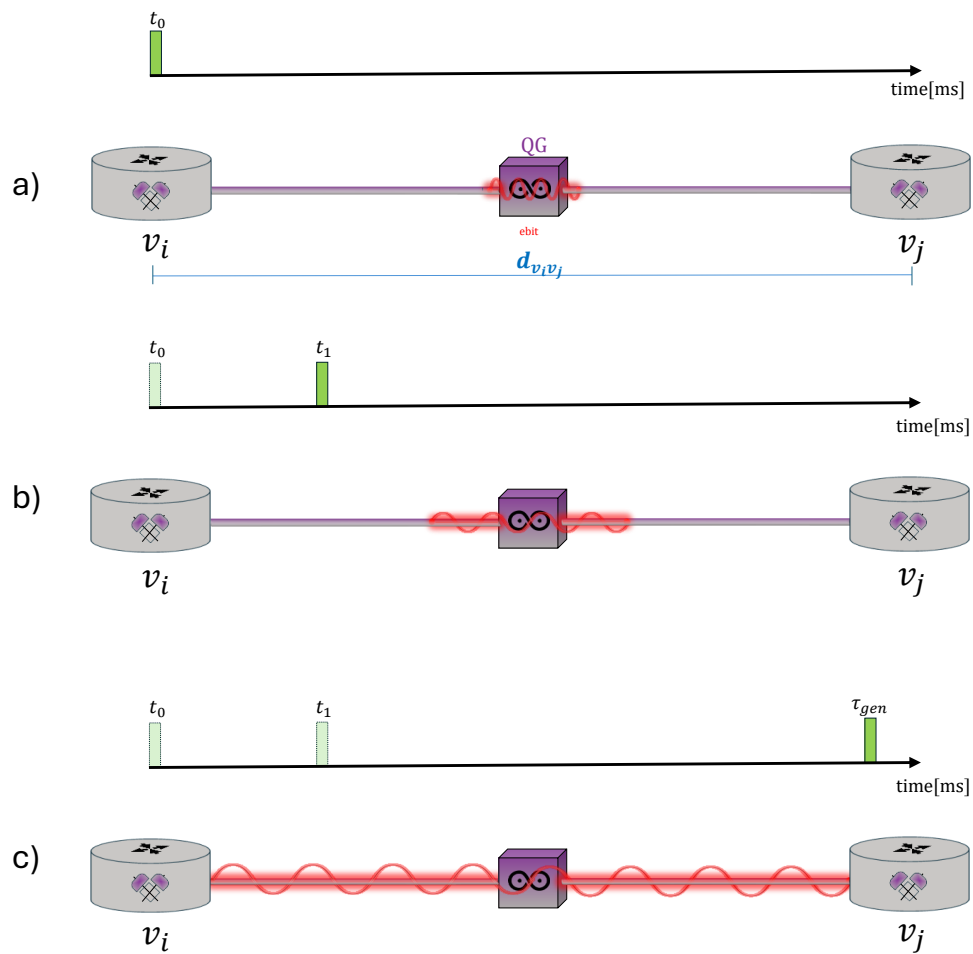


FIGURE 4.1: Schematic representation of the ebit distribution protocol.

been experimentally demonstrated in [91], [92], [93]. Entanglement generation in quantum networks can be broadly categorized as either bipartite or multipartite [94], depending on the number of participating subsystems. In this work, we focus exclusively on the former specifically, Bell states (a.k.a Einstein–Podolsky–Rosen or EPR pairs) which represent maximally entangled two-qubit states. These states constitute a foundational resource in quantum communication protocols, including entanglement purification, entanglement swapping, and quantum teleportation. The Fig. 4.1 shows the quantum distribution model adopted, a generation-at-midpoint approach/principle, wherein quantum sources are symmetrically placed between couples of quantum nodes (QNs), as detailed in [95], [96], [97]. The timeline depicts a sequence of packets, which correspond to the time consumed in successfully generating an entangled bit (ebit) between adjacent nodes ($v_{i,k}$ $v_{j,k}$). The generation of entangled photon pairs is experimentally realized through the well-known process, Spontaneous Parametric Down-Conversion (SPDC). The efficiency of this process is influenced by phase-matching conditions, spatial mode coupling, and transmission losses throughout the optical setup. As described in [89] the experimental configuration utilizes a pulsed laser source operating at a wavelength of 404 nm, with a repetition rate of 1 GHz (10^9 pulses per second). The pump power ranges from 2.6 mW to 15.5 mW, with optimal performance observed within the interval of 3.318 mW to 7.291 mW. Entangled photon pairs are produced in a nonlinear beta barium borate (BBO) crystal with a length of $L = 3$ mm and an aperture of 5×5 mm. So, the probability of generating an entangled photon pair per pulse is given by

$$p_{\text{gen}} = \frac{R_{\text{pairs}}}{R_{\text{pulse}}},$$

where p_{gen} denotes the probability of generating an entangled photon pair per laser pulse. The quantity R_{pairs} represents the rate of detected entangled photon pairs per second, which corresponds to the total number of registered coincidence counts $N_{\text{CC,total}}$. While, R_{pulse} refers to the laser pulse repetition rate, expressed in pulses per second. This expression characterizes the source efficiency by evaluating the ratio between successfully detected entangled pairs and the total number of pump pulses. While a higher p_{gen} indicates improved source performance, its value is fundamentally limited by physical and experimental factors such as imperfect phase matching, non-ideal mode coupling, and optical channel losses. However, in practical quantum communication systems, only a fraction of the generated entangled pairs are ultimately usable due to additional impairments, including decoherence, propagation losses, and detector inefficiencies. As a result, a post-selection mechanism is typically employed to filter and retain only high-fidelity entangled bits (ebits), which are essential for executing quantum teleportation and entanglement swapping protocols. To estimate the entangled photon yield within a given temporal acquisition window, we perform a probabilistic analysis. For a generation window of $W_{\text{gen}} = 1$ ms (0.001s), the number of pump pulses incident on the crystal is given by:

$$N_{\text{pulses}} = R_{\text{pulse}} \cdot W_{\text{gen}} = 10^9 \times 0.001 = 10^6 \text{ pulses.}$$

In addition to the probability of successful generation, we also consider the probability of successful entanglement transmission, which depends on the inter-node distance and the quality of the quantum communication channel. In fiber-optic links, attenuation is a major limiting factor and is typically modeled using an exponential decay function:

$$p_n = (1 - p_{\text{init}})e^{-\frac{\eta d_{v_i v_j}}{10}}, \quad (4.1)$$

where p_{init} represents the initial qubit loss probability due to hardware imperfections and coupling inefficiencies, empirically estimated to be approximately 0.2, as reported in [98].

The parameter η denotes the fiber attenuation coefficient, which is typically around 0.2 dB/km for standard telecom wavelengths. Finally, $d_{v_i v_j}$ denotes the physical distance between the entangled photon source and the receiving quantum node.

This exponential expression captures the probabilistic nature of photon survival as a function of both propagation distance and channel quality. As the transmission distance increases, the likelihood of an entangled photon arriving unabsorbed or unscattered decreases significantly. Consequently, the overall probability of generating and successfully delivering an entangled bit (ebit) is defined as

$$p_m = p_{\text{gen}} \cdot p_n,$$

where p_m encapsulates both the generation and transmission success probabilities. This provides a critical performance metric for evaluating the feasibility of entanglement-based communication over practical distances. The resulting expression serves as a foundational component in link-level modeling for quantum networks, particularly in the context of assessing throughput and fidelity under realistic physical constraints.

4.2.2 Entanglement Swapping

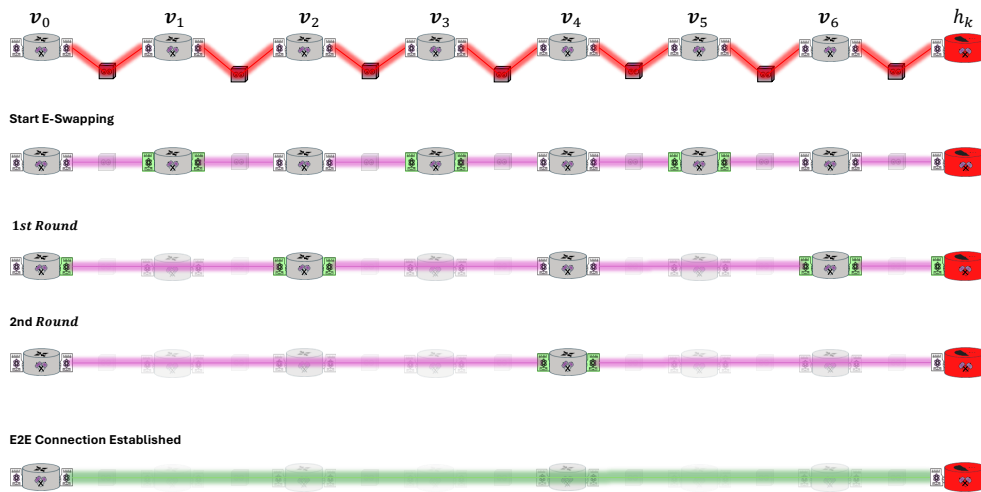


FIGURE 4.2: Schematic representation of the parallel swapping process.

Entanglement swapping is a fundamental mechanism for establishing long-distance entanglement links in quantum networks. Its importance arises from the critical challenge posed by the exponential decay in the success probability of entanglement generation over long distances, primarily due to photon loss and decoherence in quantum channels. This decay severely limits the feasibility of direct entanglement between distant nodes. To address this limitation, quantum repeaters are introduced between the source and destination nodes. These devices divide a long communication path into shorter, more manageable segments. Entanglement is first established between adjacent nodes and then extended across the network via successive entanglement swapping operations. This modular approach significantly improves the scalability and reach of entanglement distribution. Nevertheless, entanglement swapping is inherently probabilistic and affected by operational imperfections and hardware constraints. Consequently, failures in the swapping process may occur, potentially reducing the reliability gains offered by quantum repeaters. Entanglement swapping is a quantum operation that enables two previously unentangled nodes to become entangled by performing a joint Bell-state

measurement (BSM) on two particles, each of which is entangled with one of the nodes. If the BSM is successful, the two initially independent nodes are projected into an entangled state, thereby extending the entanglement reach of the network. The probabilistic nature of entanglement swapping highlights the need for designing efficient swapping protocols that maximize the likelihood of achieving end-to-end entanglement. Different strategies offer trade-offs between success probability, operational complexity, and resource consumption. Among these, two fundamental entanglement swapping protocols are commonly studied:

Sequential method: In a chain topology with n intermediate nodes, swapping operations are performed in sequence from the source to the destination. If the entanglement generation probability is p_{gen} and the success probability of a swapping operation is p_{swap} , then the overall success rate becomes $p_{\text{gen}} \cdot p_{\text{swap}}^n$, where n is the number of swapping stages. Moreover, the total latency accumulates as each stage must wait for the previous to succeed.

Parallel method: Alternatively, in the parallel (or nested) scheme, entanglement swapping is performed simultaneously across nonoverlapping segments of the network. As illustrated in Fig. 4.2, in the case of an even number of quantum repeaters (QRs), the first round may involve quantum nodes v_1, v_3 , and v_5 performing swapping operations in parallel. This occurs after quantum memories have been activated and synchronized via the central controller. In the second round, swapping is carried out by quantum nodes v_2 and v_6 , followed by a third round involving the central node v_4 . This hierarchical strategy reduces the number of sequential operations, thereby improving the overall success probability to $p \cdot p_{\text{swap}}^{\log n}$ and decreasing latency. As shown in [53], the choice of protocol significantly affects both the fidelity and the latency of remote entanglement. The proposed segment-based approach in that study, for example, minimizes stop-and-wait delays by enabling concurrent entanglement generation and segmented parallel swapping, effectively balancing these trade-offs. More generally, imperfect swapping operations due to hardware limitations (e.g., non-ideal joint measurements) and memory decoherence further degrade performance [99]. Hence, robust entanglement swapping protocols not only attempt to maximize success probability but also integrate failure detection, recovery mechanisms, and optimal path or segment selection strategies.

4.2.3 Noise

In a bipartite system typically composed of two qubits, entanglement manifests as strong non-classical correlations that cannot be explained by separable (unentangled) states. In an hypothetical scenario, these maximally entangled two-qubit states would maintain perfect non-classical correlations across long distances. However, in real-world implementations, environmental noise and quantum decoherence degrade entanglement quality, leading to mixed states. To model entanglement degradation, we incorporate the concept of *Werner states* [100], [101], which characterize a quantum system as a mixture of a maximally entangled Bell state and a completely mixed state. Specifically, the density matrix ρ represents the quantum system — in our case, the entangled pair initially prepared in the Bell state $|\Phi^+\rangle = \frac{1}{\sqrt{2}}(|00\rangle + |11\rangle)$. The initial pure state is described by the density matrix $\rho_0^+ = |\Phi^+\rangle\langle\Phi^+|$, which, after transmission through a noisy channel, evolves into a mixed Werner state.

An ebit shared between any two adjacent quantum nodes $v_{i,k}$ and $v_{j,k}$ within the same subnetwork k is represented as a Werner state $\rho(w_{(i,j)})$ [95], where ρ with an initial weight coefficient $w_{(i,j)} \in [0, 1]$ determining the entanglement strength which it can be associated to quantifying the degree of entanglement. Higher values of $w_{(i,j)}$ correspond to greater fidelity and improved resilience to decoherence. A Werner state is defined as follows

$$\rho(w_{(i,j)}) = w_{(i,j)}|\Phi^+\rangle\langle\Phi^+| + \frac{1}{4}(1 - w_{(i,j)})\mathbb{I}_4, \quad (4.2)$$

with $\mathbb{I}_4 = |00\rangle\langle 00| + |01\rangle\langle 01| + |10\rangle\langle 10| + |11\rangle\langle 11|$ the identity matrix on the space spanned by the Bell states, and $F = \frac{1+3w_{(i,j)}}{4}$.

This model allows us to quantify fidelity loss in entanglement distribution due to decoherence, which is a critical factor in designing entanglement purification protocols. When the operation of entanglement swapping is successfully performed on two Werner states $\rho(w_{(i,j)})$ and $\rho(w_{(j,k)})$ it will be generated a new Werner state expressed as

$$\rho(w_{(i,k)}) = \rho(w_{(i,j)} \cdot w_{(j,k)}), \quad (4.3)$$

where the fidelity of the resulting state depends on the Werner parameters of the input states. The degree of information concordance between a Werner state $\rho(w_{(u,v)})$ and the Bell state Φ^+ is given by the fidelity [91]

$$F = \langle \Phi^+ | \rho(w_{(i,j)}) | \Phi^+ \rangle = \frac{1 + 3w_{(i,j)}}{4}. \quad (4.4)$$

We assume that entangled pairs shared by the same pair of adjacent quantum nodes show identical fidelity after generation. However, entangled pairs shared between different pairs of nodes are not necessarily identical due to physical device imperfections [97]. In practical quantum networks, Werner states degrade over time due to interaction with a noisy environment, so does also the associated fidelity. After a storage time Δt in an imperfect quantum memory (QM), the Werner parameter $w_{(i,j)}$ evolves as [102]:

$$w'_{(i,j)} = w_{(i,j)} \cdot e^{-\Delta t/T_{coh}}, \quad (4.5)$$

where T_{coh} is the coherence time of two quantum memory units holding a pair of entangled photons and is a constant determined by the physical medium [95]. We justify the use of Werner states [103] to define a fidelity threshold for initiating entanglement purification and distillation. Considering that our entanglement source is based on SPDC, Werner states provide a useful abstraction to quantify fidelity loss and establish when purification or distillation is required. Werner states effectively describe the transition from a maximally entangled Bell state to a partially mixed state, allowing us to model the degradation of entanglement fidelity due to environmental noise. By setting a fidelity threshold based on the Werner state parameter $w_{(i,j)}$, we determine at what point purification or distillation must be applied to restore high-quality entangled pairs. By leveraging entanglement purification, we aim to extract high-fidelity Bell pairs from noisy Werner states, thereby improving overall network performance. The fidelity $F_{(i,j)}$ of a Werner state with respect to the ideal Bell state is given by (4.4). This allows us to establish several important thresholds. First, the **entanglement threshold** indicates that the state remains entangled if $w_{(i,j)} > \frac{1}{3}$; below this value, the state becomes separable and can no longer be purified. Second, the **distillability threshold** is defined by $w_{(i,j)} > \frac{2}{3}$, meaning that high-fidelity Bell pairs can be extracted directly. When $w_{(i,j)} \leq \frac{2}{3}$, purification is necessary to enhance the fidelity before distillation becomes feasible. Finally, the **fidelity condition** dictates that purification is triggered when the fidelity $F_{(i,j)}$ of the entangled pairs falls below an acceptable threshold, which is mathematically related to the Werner parameter $w_{(i,j)}$ through Eq. (4.4). Given our protocol assumptions, multiple entangled qubit pairs (ebits) must be available to enable successive purification rounds. In the best-case scenario, where all three purification rounds succeed this requirement naturally translates into a minimum resource threshold. Beyond this point, additional purification rounds yield minimal improvements, resulting in a fidelity saturation phase, as detailed in [104]. To model entanglement generation, we adopt a probabilistic framework grounded in the binomial distribution. Specifically, each entanglement generation attempt is modeled as a Bernoulli trial, where an ebit is successfully created with probability p_{gen} , leading to a stochastic number of

entangled pairs available in each time slot [101], [105]

$$P(\mathcal{E}_k=\alpha) = \binom{T}{\alpha} p_\varepsilon^\alpha (1 - p_\varepsilon)^{T-\alpha}, \quad (4.6)$$

given that T is the total number of trials, the Binomial distribution is expressed as follows. Let \mathcal{E}_k denote the probability that exactly α ebits are successfully generated on the k -th link. The variable α represents the number of successfully generated, swapped, or purified ebits, constrained within $\alpha \in [0, T]$. The probability of success for each individual attempt is given by p_ε , where $p_\varepsilon \in [0, 1]$, while $1 - p_\varepsilon$ denotes the probability of failure in a single trial. The term $\binom{T}{\alpha}$ is the Binomial coefficient, representing the number of ways to achieve exactly α successes in T independent trials.

4.2.4 Fidelity Management and Purification-Swapping Model

In HQINs, fidelity $F_{(i,j)}$ is a key performance metric that quantifies the similarity between an entangled pair and an ideal Bell state. Maintaining high-fidelity ebits is essential for preserving quantum coherence and ensuring the reliable execution of critical quantum operations, including teleportation and entanglement swapping. Due to the inevitable effects of noise, decoherence, and transmission losses, the fidelity of entangled states degrades over time and with increasing distance. To mitigate this, HQINs employ entanglement purification a technique that enhances the fidelity of a target entangled pair by consuming additional lower-quality distributed ebits, commonly referred to as "sacrificial" pairs. This process is conceptually analogous to denoising in classical communication systems, helping reduce noise introduced by imperfections in hardware and the transmission medium. To counteract fidelity degradation, various entanglement purification protocols have been proposed in the literature, each offering distinct trade-offs in terms of resource efficiency, fidelity improvement, and operational complexity [106], [107]. Among the most prominent strategies we have:

- **Symmetric purification** is a structured strategy in which entangled pairs are purified only with other pairs of the same fidelity and matching history. The process follows a recursive pattern, with each round consuming one sacrificial ebit to boost the fidelity of a target pair, alternating between base-level pair generation and purification steps. While this method enables steady fidelity improvement across rounds, it is inherently rigid. The requirement for fidelity-matched partners leads to idle waiting and inefficient resource usage. Moreover, due to the probabilistic nature of purification, many base-level pairs must be consumed to produce a single high-fidelity pair. Over time, memory decoherence further disrupts fidelity symmetry, making it increasingly impractical to maintain perfect pairing, especially in dynamic or large-scale quantum networks.
- **Pumping purification** is a strategy that increases the fidelity of a single Bell pair by repeatedly purifying it with freshly generated base-level pairs. It operates with minimal hardware requirements, only two qubits per station, making it highly memory efficient. However, it provides only incremental fidelity improvement with each round, especially when the starting fidelity is low. As a result, pumping becomes ineffective when the fidelity gap between the base-level pairs and the desired target is large. It performs best when base fidelities are already high (e.g., above 0.75), but scales poorly in high-loss or long-distance scenarios.
- **Greedy purification** is an approach that purifies all available Bell pairs immediately at each time step, without deferring any action in favor of potentially better pairings later. While this strategy maximizes short-term resource usage and minimizes idle time, it often leads to the combination of mismatched fidelities, e.g., high-fidelity pairs

with significantly lower quality ones. This results in a lower probability of success and minimal fidelity improvement, especially when the fidelity variance across pairs is high. Greedy purification is simple to implement but sacrifices long-term fidelity gain for immediate progress.

- **Banded purification** is designed to balance efficiency and fidelity gain; this strategy divides the fidelity space into discrete bands. Only Bell pairs within the same band are allowed to purify with each other, preventing the mixing of low- and high-fidelity pairs. This structure preserves high-fidelity resources for more meaningful improvements and avoids inefficient pairings. Although banded purification introduces scheduling complexity and potential deadlock if too many bands are used, it significantly improves fidelity scaling by allowing the system to wait for better matches. It is particularly suitable for dynamic environments where fidelity varies across links and time.

In our framework, we adopt a recursive purification model inspired by [104], [108], where the fidelity after the t -th purification round for a link $\varepsilon_{ij} \in \mathcal{E}_k$ is given by:

$$\mathcal{F}_{\varepsilon_{ij}}^{(t)} = \frac{\mathcal{F}_{\varepsilon_{ij}} \cdot \mathcal{F}_{\varepsilon_{ij}}^{(t-1)}}{\mathcal{F}_{\varepsilon_{ij}} \cdot \mathcal{F}_{\varepsilon_{ij}}^{(t-1)} + (1 - \mathcal{F}_{\varepsilon_{ij}}) \cdot (1 - \mathcal{F}_{\varepsilon_{ij}}^{(t-1)})}, \quad (4.7)$$

where $\mathcal{F}_{\varepsilon_{ij}}^{(0)} = \mathcal{F}_{\varepsilon_{ij}}$ is the initial fidelity of the entangled link. Each purification round consumes one sacrificial ebit to enhance the fidelity of the target link, assuming successful purification. The success probability for a given purification attempt is expressed as:

$$p_{\text{pur}}(\mathcal{F}_{\varepsilon_{ij}}) = \mathcal{F}_{\varepsilon_{ij}}^2 + (1 - \mathcal{F}_{\varepsilon_{ij}})^2. \quad (4.8)$$

Figure 4.3 illustrates the purification trade-offs: as purification rounds increase, fidelity improves, but the probability of success declines, especially for lower initial fidelities.

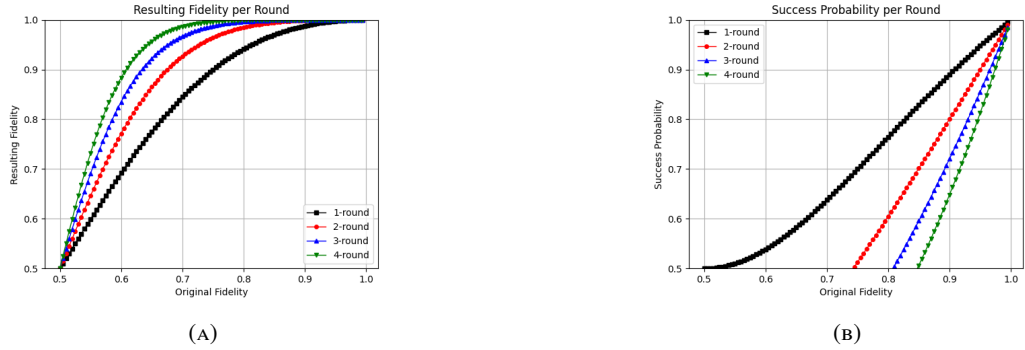


FIGURE 4.3: (a) Resulting fidelity vs. purification rounds. (b) Purification success probability vs. initial fidelity.

We employ a Banded Purification strategy, where purification is allowed only between entangled pairs ρ_{EB} with fidelities within the same predefined fidelity band. This prevents inefficient mixing of disparate-quality ebits and promotes resource efficiency. The protocol adapts to dynamic link quality fluctuations, a critical feature for HQINs operating under noise and decoherence. Maintaining high fidelity over long-distance entangled paths requires integrating purification with fidelity-aware entanglement swapping. Suppose nodes $v_{i,k}$ and $v_{j,k}$ share an ebit represented by the Werner parameter $\omega_{(i,j)}$, and nodes $v_{j,k}$ and $v_{l,k}$ share $\omega_{(j,l)}$. After entanglement swapping at $v_{j,k}$, the resulting Werner parameter $\omega_{(i,l)}$ is:

$$\omega_{(i,l)} = \omega_{(i,j)} \cdot \omega_{(j,l)}, \quad (4.9)$$

and the resulting fidelity $\mathcal{F}_{\varepsilon_{il}}$ is given by:

$$\mathcal{F}_{\varepsilon_{il}} = \frac{1 + 3\omega_{(i,l)}}{4}. \quad (4.10)$$

More generally, when accounting for imperfect local operations at nodes, the swapping fidelity is modified as:

$$\omega'_{(i,l)} = \omega_{(i,j)} \cdot \omega_{(j,l)} \cdot \omega_{v_{j,k}}, \quad (4.11)$$

where $\omega_{v_{j,k}}$ accounts for local operation imperfections and is given by:

$$\omega_{v_{j,k}} = \frac{o_{1,v} \cdot o_{2,v} (4\alpha_v^2 - 1)}{3}, \quad (4.12)$$

with $o_{1,v}$ and $o_{2,v}$ denoting the one- and two-qubit gate reliabilities, and α_v the Bell State Measurement (BSM) accuracy at node v .

However, in this work, we omit these explicit gate error models and assume ideal local operations (i.e., $\omega_{v_{j,k}} = 1$), focusing primarily on fidelity degradation due to channel noise and swapping.

The cumulative fidelity along an end-to-end path $\mathcal{P}_{\text{BestPath}}^{S,D}$ between source S and destination D can thus be expressed as:

$$\mathcal{F}_{e2e} = \frac{1}{4} \left(1 + 3 \prod_{\varepsilon_{ij} \in \mathcal{P}^{S,D}} \omega_{(i,j)} \prod_{v_{j,k} \in \mathcal{R} \cup S} \omega_{v_{j,k}} \right), \quad (4.13)$$

where:

- $\omega_{(i,j)}$ is the Werner parameter associated with link ε_{ij} ;
- $\omega_{v_{j,k}}$ would represent local gate and measurement imperfections, set to 1 under our ideal operations assumption.

This model reflects the exponential decay of fidelity as the number of hops increases and highlights the critical role of purification. In our architecture, all purification operations are executed within the coherence time of quantum memories, ensuring minimal storage-induced decoherence. The combination of recursive, banded purification with fidelity-aware entanglement swapping ensures scalable and robust high-fidelity quantum communication across both intra- and inter-subnetwork domains of the HQIN.

4.2.5 Assumptions

To focus on the fundamental performance limits of Hybrid Quantum Information Networks (HQINs) and enable tractable analytical modeling, the following idealized assumptions are adopted:

- **Quantum Memory:** Each quantum node is equipped with unlimited, perfect quantum memory capable of storing an arbitrary number of entangled pairs without decoherence or fidelity loss over time.
- **Classical Communication:** Heralding signals for successful entanglement generation and coordination are transmitted over idealized classical channels assumed to be lossless, noiseless, and delay-free.

- **Quantum Channel Noise:** Decoherence during photon propagation in both optical fiber and free-space links is neglected. Fidelity degradation is attributed solely to network operations such as imperfect entanglement generation, purification, and swapping.
- **Entanglement Sources:** Bell states are assumed to be generated without preparation errors. The entanglement generation process succeeds probabilistically, but successfully generated ebits are characterized by Werner states with associated fidelity parameters.
- **Quantum Operations:** All quantum operations (including measurements, gate operations, and Bell State Measurements) are considered perfect. Explicit modeling of operational errors, such as gate infidelities and imperfect BSM outcomes, is omitted for analytical clarity.
- **Purification and Swapping Timing:** All purification and swapping procedures are completed well within the coherence time of quantum memories, ensuring that temporal storage-induced fidelity decay is negligible.
- **Repeater and Satellite Capabilities:** Quantum repeaters and satellites are assumed to operate without hardware limitations other than the fidelity constraints already captured by Werner parameters associated with entangled links.

These assumptions isolate the intrinsic stochastic behavior of entanglement distribution processes while excluding secondary impairments such as storage decoherence, communication delays, and operational imperfections. This abstraction enables the derivation of clean analytical models to benchmark entanglement throughput, purification efficiency, and fidelity evolution across hybrid terrestrial-space quantum networks. Furthermore, it provides a tractable foundation for performance evaluation, serving as an upper-bound reference for future studies incorporating non-ideal, device-level noise sources and practical implementation constraints.

4.3 SYSTEM MODEL

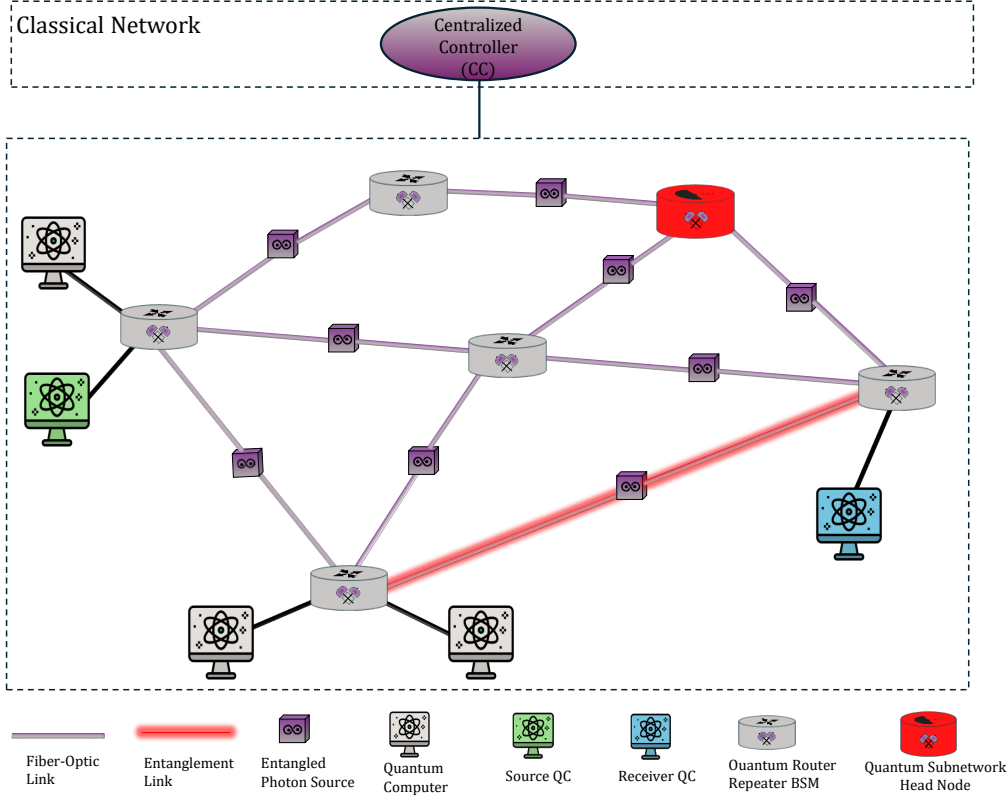


FIGURE 4.4: Quantum Intra-Subnetwork

To aid the clarity of the model, the notations and their definitions are summarized in Table 4.2. This work focuses on the coordinated management of quantum processes such as entanglement generation, purification, and swapping to establish end-to-end links between quantum nodes within the network. We envision a quantum network of multiple real subnetworks, interconnected via a constellation of Starlink satellites positioned in Low Earth Orbit (LEO). Each subnetwork is represented as an undirected graph $\mathcal{G}_k = (\mathcal{V}_k, \mathcal{E}_k)$, where $k \in \{0, 1, \dots, K\}$ denotes the subnetwork index within the overall system model. The vertex set \mathcal{V}_k is defined as

$$\mathcal{V}_k = \{\mathbf{h}_k, \mathbf{v}_{0,k}, \mathbf{v}_{1,k}, \dots, \mathbf{v}_{i,k}, \dots, \mathbf{v}_{n^k,k}\},$$

where each node $\mathbf{v}_{i,k} \in \mathbb{R}^3$ represents a quantum node(QN) such as a quantum computer, repeater, or relay positioned in three-dimensional space. The vector is given by

$$\mathbf{v}_{i,k} = \begin{bmatrix} \phi \\ \lambda \\ a \end{bmatrix},$$

where ϕ is longitude, λ is latitude and a is altitude. The parameter n^k denotes the total number of nodes in the k -th subnetwork. The superscript k on the expression n^k indicate that each subnetwork contains different number of nodes. We indicate with \mathbb{V} the set of all the quantum nodes within the network, such that $\mathbb{V} = \{\mathcal{V}_0, \mathcal{V}_1, \dots, \mathcal{V}_k, \dots, \mathcal{V}_K\}$. The set of optical communication links between two arbitrary nodes $\mathbf{v}_{i,k}, \mathbf{v}_{j,k}$ belonging to the same subnetwork k is given by

$$\mathcal{E}_k = \{\varepsilon_{ij,k} \mid i, j = \{0, 1, \dots, n^k\}; i \neq j\}.$$

TABLE 4.2: Notation Summary

Symbol	Description
\mathcal{G}_k	Undirected graph representing the k -th subnetwork
\mathcal{V}_k	Set of quantum nodes in the k -th subnetwork
n^k	Number of nodes in the k -th subnetwork
$\mathbf{v}_{n^k,k}$	Position of the n^k -th node in subnetwork k
\mathbb{V}	Global set of all quantum nodes in the network
\mathcal{E}_k	Set of optical links in the k -th subnetwork
$\varepsilon_{ij,k}$	Optical link between nodes $\mathbf{v}_{i,k}$ and $\mathbf{v}_{j,k}$
$q_{ij,k}$	Quantum source at the midpoint of edge $\varepsilon_{ij,k}$
\mathcal{H}	Set of head nodes from all subnetworks
h_k	Head node of the k -th subnetwork
\mathcal{S}	Set of satellites in the Starlink constellation
$s_m(t)$	Satellite m at time t , enabling inter-subnetwork communication
\mathcal{U}_k	Set of end-user quantum nodes in the k -th subnetwork
\mathcal{X}	Full node set: $\mathcal{U} \cup \mathcal{H} \cup \mathcal{S}$
ρ_{EB}	Density matrix of an entangled bit (ebit)
\mathcal{F}	Fidelity of an entangled quantum state
τ_{e2e}	End-to-end communication latency
p_{succ}	Probability of successful entanglement distribution
t_{gen}	Time required for entanglement generation
t_{swap}	Time required for entanglement swapping
t_{pur}	Time required for entanglement purification
t_{q}	Propagation delay of the quantum channel
p_{swap}	Probability of successful entanglement swapping
p_{pur}	Probability of successful purification
p_{gen}	Probability of successful entanglement generation
$L_{\text{sat-h}}$	Distance between satellite and ground station
η_{atm}	Atmospheric transmittance coefficient
c	Propagation speed in the fiber
η_{eff}	Effective quantum channel transmission efficiency
θ_{zenith}	Zenith angle of satellite transmission
$\alpha_{\text{elevation}}$	Elevation angle of satellite transmission
W_{gen}	Time window of the ebit generation

Each edge $\varepsilon_{ij,k}$ equidistant from both adjacent nodes has a quantum source (QS) $q_{ij,k}$. This generation strategy is referred to as mid-point entanglement generation, as detailed in [95]. The QS is responsible for generating Einstein-Podolsky-Rosen (EPR) pairs along the edge, which we refer to as link-level entanglement. These entangled qubits are denoted as *ebits* or *virtual links*. Each subnetwork contains a designated head node $h_k \in \mathcal{V}_k$, which serves

as a central coordination point. The head node in each subnetwork maintains direct connections with a limited subset of quantum nodes (QNs) within the same subnetwork, rather than forming links with all nodes in \mathcal{V}_k . The set of all head nodes across the k -subnetworks is denoted by $\mathcal{H} = \{\mathbf{h}_0, \mathbf{h}_1, \dots, \mathbf{h}_k, \dots, \mathbf{h}_K\} \subset \mathbb{V}$, and represents the union of node sets from all subnetworks in the global network. Which is responsible for establishing communication with other subnetworks located in different cities via a backbone network composed of a constellation of satellites $\mathcal{S} = \{s_0(t), s_1(t), \dots, s_m(t), \dots, s_M(t)\}$ where M denotes the total number of satellites present in the constellation. A satellite $s_m \in \mathcal{S}$ responsible for establishing entangled links between pairs of head nodes $\{h_l, h_r \mid l, r=0,1,\dots,K; l \neq r\}$. Each satellite functions both as an entanglement generator and as a quantum repeater, performing entanglement swapping operations to enable long-distance quantum communication. Within each subnetwork, nodes serve different roles: some are end-user nodes responsible for quantum processing and communication, while others act solely as repeaters to extend communication range, as shown in Fig. 4.4. We denote the set of available entangled states on link $\varepsilon_{ij,k}$ as $\mathcal{R}_{\varepsilon_{ij}}^k$, also referred to as the resource set of d -dimensional maximally entangled states shared between nodes $(v_{i,k}, v_{j,k})$ through the physical link $\varepsilon_{ij,k}$. This set is defined as

$$\mathcal{R}_{\varepsilon_{ij}}^k = \{|\psi_0\rangle, |\psi_1\rangle, |\psi_2\rangle, \dots, |\psi_{g-1}\rangle\},$$

where g denotes the total number of distributed entangled pairs on link $\varepsilon_{ij,k}$ following the entanglement distribution phase. Each link in the network maintains its own collection of entangled pairs, and purification is subsequently applied to enhance their fidelity.

In the first round of symmetric purification, entangled pairs are grouped in pairs within a certain range of initial fidelity (e.g., $|\psi_0\rangle$ with $|\psi_1\rangle$, $|\psi_2\rangle$ with $|\psi_3\rangle$, etc) to produce a new purified set

$$\mathbf{r}_{\varepsilon_{ij}}^1 = \{|\psi_{0,1}\rangle, |\psi_{2,3}\rangle, |\psi_{4,5}\rangle, \dots, |\psi_{g-2,g-1}\rangle\},$$

where $|\psi_{i,j}\rangle$ denotes the purified state resulting from the pair $(|\psi_i\rangle, |\psi_j\rangle)$, conditioned on the success of the purification process. Purification is inherently a probabilistic operation and succeeds with a probability p_{pur} , which typically depends on the fidelity F of the input states. For many standard protocols (e.g., DEJMPS or BBPSSW), the success probability can be expressed as $p_{\text{pur}} = F^2 + (1 - F)^2$, assuming identical fidelity for both input pairs. This probabilistic nature leads to a progressive reduction in the number of available states across rounds. In the second purification round, the output of the first round is again grouped into pairs to further enhance fidelity:

$$\mathbf{r}_{\varepsilon_{ij}}^2 = \{|\psi_{0,1,2,3}\rangle, |\psi_{4,5,6,7}\rangle, \dots\},$$

where $|\psi_{i,j,k,l}\rangle$ represents the purified result from combining the previously purified states $|\psi_{i,j}\rangle$ and $|\psi_{k,l}\rangle$, again conditioned on successful purification. This iterative process continues until the desired fidelity threshold is reached or the available resource pool becomes insufficient to support further purification. The set of end-user nodes is denoted by $\mathcal{U}_k \subset \mathcal{X}$, where the overall node set is given by $\mathcal{X} = \mathcal{U} \cup \mathcal{H} \cup \mathcal{S}$. The edges in the graph represent physical quantum channels, which may be implemented as optical fibers in the wired segment of the network or as free-space optical links in the wireless segment. We assume that when a repeater is deployed at a node with degree greater than two, it operates as a quantum switch; however, for consistency we refer to all such devices as Quantum Repeaters (QRs).

Coordinating quantum operations requires a significant amount of classical information exchange between quantum nodes. This is primarily due to the need for precise synchronization, as quantum operations such as entanglement swapping and purification depend on time-sensitive measurements and classical feedback. To reduce the complexity of establishing

end-to-end entangled connections between source and destination nodes, we adopt a centralized controller (CC). This controller is responsible for managing synchronization across the network, ensuring that all quantum operations proceed in a coordinated and timely manner.

4.3.1 Latency Considerations

In HQINs latency quantifies the total time required to establish end-to-end entanglement between a source node S and a destination node D . To maintain consistency with the system-wide notation, latency is decomposed into modular components reflecting distinct quantum and classical operations including quantum state preparation, classical coordination, and satellite-mediated distribution. We define the following latency components:

- τ_{find} : Time required to compute the optimal entanglement path $\mathcal{P}_{\text{BestPath}}^{S,D}$.
- τ_{gen} : Aggregate time spent on link-level entanglement generation, accounting for photon transmission, source alignment, and initialization delays.
- τ_{pur} : Cumulative time associated with local purification rounds to boost entanglement fidelity.
- τ_{swap} : Latency introduced by entanglement swapping operations, including Bell state measurements and associated control logic.
- τ_{dist} : Time required for satellite-assisted free-space distribution of entanglement across subnetworks.
- τ_{comm} : Classical communication delay for coordination, signaling, and acknowledgment exchange.

The per-link entanglement generation time depends on the underlying physical medium. For fiber-based links, the generation delay is modeled as $t_{\text{gen}}(\varepsilon_{ij}) = t_{\text{proc}} + \frac{d_{v_i v_j} \cdot n_{\text{fiber}}}{c}$, where $d_{v_i v_j}$ is the fiber length in kilometers, $n_{\text{fiber}} \approx 1.44$ is the refractive index of the fiber medium, and $c = 3 \times 10^8$ m/s is the speed of light in vacuum. The term $t_{\text{proc}} = 0.1 \times 10^{-6}$ s denotes the processing delay introduced by the quantum source for generating an entangled photon pair. In contrast, for satellite-based free-space links, the entanglement generation delay is affected by the geometric path and atmospheric conditions. It is expressed as $t_{\text{gen}}^{\text{free}}(\theta(t)) = t_{\text{proc}} + \frac{d(\theta(t)) \cdot \eta_{\text{atm}}}{c}$, where $d(\theta(t))$ is the slant distance from the satellite to the ground station as a function of the zenith angle $\theta(t)$, and η_{atm} is the atmospheric transmission factor accounting for signal delay due to air density and turbulence. These models capture both the constant setup overhead such as entangled photon pair initialization and the variable propagation delay, enabling accurate latency estimation across heterogeneous link types within HQINs.

We distinguish two primary network configurations for latency evaluation, beginning with the intra-subnetwork case.

(1) Intra-Subnet Latency: When both the source node S and destination node D reside within the same subnetwork \mathcal{G}_k , the total end-to-end latency is given by:

$$\mathcal{L}_{e2e}^{\text{intra}} = \tau_{\text{find}} + \tau_{\text{gen}} + \tau_{\text{pur}} + \tau_{\text{swap}} + \tau_{\text{comm}}, \quad (4.14)$$

where each term corresponds to a distinct quantum operation class along the selected path $\mathcal{P}_{\text{BestPath}}^{S,D}$.

As previously discussed, entanglement generation is modeled as a binomial process occurring within a fixed time window W_{gen} , driven by a high-repetition-rate pulsed laser source based on SPDC mechanisms operating at the GHz scale. Each trial succeeds with probability $p_{\text{gen}}^{(ij)}$, and

a successful pair introduces a propagation delay based on the physical medium. The expected entanglement generation latency in the worst-case scenario is:

$$\tau^{\text{gen}} = t_{\text{proc}} + W_{\text{gen}} + \mathbf{max}(t_{\text{prop}}(\varepsilon_{ij})), \quad (4.15)$$

where $t_{\text{prop}}(\varepsilon_{ij})$ is time need to distribute the entangled pairs generated a the last instance of the W_{gen} and is computed as:

$$t_{\text{prop}}(\varepsilon_{ij}) = \begin{cases} \frac{d_{v_i v_j} \cdot \eta_{\text{fiber}}}{c} & \text{(fiber link)} \\ \frac{d(\theta(t)) \cdot \eta_{\text{atm}}}{c} & \text{(free-space link)} \end{cases}$$

and t_{proc} is the entangled pair processing time at the quantum source.

The purification latency is modeled under the assumption of a banded purification strategy, where entangled pairs are purified only if their fidelities lie within the same predefined band. Sacrificial ebits may incur additional waiting time until a compatible partner becomes available. As each purification round succeeds with a certain probability, the overall delay accumulates across permitted rounds according to the fidelity–latency trade-off.

$$\tau^{\text{pur}} = \max_{\varepsilon_{ij} \in \mathcal{P}_{\text{BestPath}}^{S,D}} \sum_{r=1}^{R^{ij}} \left(\frac{t_{\text{pur}}^{(r)}(\varepsilon_{ij})}{p_{\text{pur}}^{(r)}(\varepsilon_{ij})} \cdot \delta_r \right), \quad (4.16)$$

where $r_{\text{max}}^{(ij)}$ denotes the maximum number of purification rounds allowed on link ε_{ij} based on the number of ebits previously distributed, and $\delta_r \in \{0, 1\}$ is an activation indicator determined by fidelity-latency trade-off constraints. The term $t_{\text{pur}}^{(r)}(\varepsilon_{ij})$ represents the time required for a single purification attempt at round r , and $p_{\text{pur}}^{(r)}(\varepsilon_{ij})$ is the success probability of that attempt, typically modeled as $F^2 + (1 - F)^2$ based on the input fidelity. This formulation accounts for both the probabilistic nature of purification and its recursive structure under a banded strategy.

Entanglement swapping latency introduces additional latency due to the execution of Bell-state measurements and the associated classical coordination overhead. In our model, swapping proceeds through $\lceil \log_2(p_k - 1) \rceil$ recursive rounds, where p_k is the number of quantum repeater nodes along the intra-subnet path $\mathcal{P}_{\text{BestPath}}^{S,D}$. During each round r , adjacent node pairs attempt Bell-state measurements to extend the entangled link. Due to the probabilistic nature of quantum operations, each swap may require multiple attempts to succeed. The expected latency for entanglement swapping is thus expressed as:

$$\tau^{\text{swap}} = \sum_{r=1}^{\lceil \log_2(p_k - 1) \rceil} \left(\frac{t_{\text{swap}}^{(r)}}{p_{\text{swap}}^{(r)}} \right), \quad (4.17)$$

where $t_{\text{swap}}^{(r)}$ denotes the time to perform a Bell-state measurement and transmit classical results during round r , and $p_{\text{swap}}^{(r)}$ is the corresponding success probability. This formulation captures both the hierarchical structure of swapping and the delay incurred by probabilistic retries, enabling realistic latency estimation in practical quantum repeater chains.

CPDC: The latency components τ_{find} and τ_{comm} account for classical pathfinding $\mathcal{P}_{\text{BestPath}}^{S,D}$ used to compute optimal entanglement routes, acknowledgment signaling between nodes, and the classical communication delays required for coordinating purification and entanglement swapping operations.

All quantum operations are assumed to be executed within the coherence time of quantum memory, ensuring that storage-induced decoherence is negligible. This modular latency framework enables accurate timing analysis of intra-subnet quantum communication in HQINs.

(2) Inter-Subnet Latency: For cross-subnetwork communication, where the source and destination nodes belong to distinct subnetworks ($S \in \mathcal{G}_S, D \in \mathcal{G}_D$), the total end-to-end latency is composed of two main parts: the maximum intra-subnet delay and the inter-subnet satellite distribution latency. This is formally defined as:

$$\tau_{e2e}^{\text{inter}} = \max(\tau_{\text{subnet}_S}, \tau_{\text{subnet}_D}) + \tau_{\text{dist}}, \quad (4.18)$$

where the intra-subnetwork latency τ_{subnet_x} for each $x \in \{S, D\}$ is given by:

$$\tau_{\text{subnet}_x} = \tau_{\text{find}}^{(x)} + \tau_{\text{gen}}^{(x)} + \tau_{\text{pur}}^{(x)} + \tau_{\text{swap}}^{(x)} + \tau_{\text{comm}}^{(x)}. \quad (4.19)$$

The entanglement generation process relies on a probabilistic SPDC source, driven by a pulsed laser operating at a repetition rate R_{pulse} (e.g., 1 GHz). Within a fixed generation window W_{gen} , a total of $T = W_{\text{gen}} \cdot R_{\text{pulse}}$ Bernoulli trials are conducted, each with a pair-generation probability $p_{\text{gen}}^{(ij)}$ for the optical link ε_{ij} . Once a pair is successfully generated, a photon propagation delay follows, determined by the physical properties of the transmission medium. Therefore, the expected entanglement generation latency for subnetwork x is given by eq.4.15 indicated with $\tau_{\text{gen}}^{(x)}$, where $t_{\text{prop}}(\varepsilon_{ij})$ denotes the propagation delay across the link whether fiber-based or free-space and t_{proc} accounts for local ebit processing time at the receiver (typically on the order of 0.1 microseconds).

The purification latency reflects bounded, probabilistic purification modeled as a recursive process and is expressed as eq.4.16 indicated as $\tau_{\text{pur}}^{(x)}$.

Entanglement swapping latency is structured in $\lceil \log_2(n_x) \rceil$ recursive rounds, where each round attempts Bell-state measurements between adjacent nodes. The probabilistic delay per round is presented in eq.4.17 and is indicated as $\tau_{\text{swap}}^{(x)}$.

The inter-subnet distribution latency τ_{dist} models the satellite-based entanglement delivery between the head nodes $h_S \in \mathcal{V}_S$ and $h_D \in \mathcal{V}_D$:

$$\tau_{\text{dist}} = \frac{d(h_S, s^*(t)) + d(h_D, s^*(t))}{c \cdot P_{\text{succ}}} + 2t_{\text{retrieval}} + \tau_{\text{sync}}, \quad (4.20)$$

where $s^*(t) \in \mathcal{S}$ is the selected satellite at time t , $d(h, s)$ is the slant range from head node to satellite, P_{succ} is the probability of successful satellite entanglement delivery, $t_{\text{retrieval}}$ denotes memory readout time, and τ_{sync} represents classical synchronization latency.

This latency formulation captures the full probabilistic behavior of entanglement operations in HQINs, combining parallel binomially-modeled generation, bounded recursive purification, iterative entanglement swapping, and satellite-ground transfer dynamics.

This latency formulation supports fidelity-aware protocol design in HQINs by accounting for the interplay between entanglement distribution over mixed media (fiber and free space), quantum memory coherence constraints, and classical coordination delays. As such, it provides a modular and scalable foundation for performance optimization under realistic operating conditions.

4.4 Segment-Aware Entanglement Distribution Protocol

This section presents a segment-aware entanglement generation protocol designed to enable scalable and high-fidelity remote entanglement distribution in Hybrid Quantum Information Networks (HQINs). The protocol explicitly integrates system-level latency τ , fidelity degradation dynamics, and satellite-ground transmission constraints, ensuring efficient orchestration across intra- and inter-subnet paths.

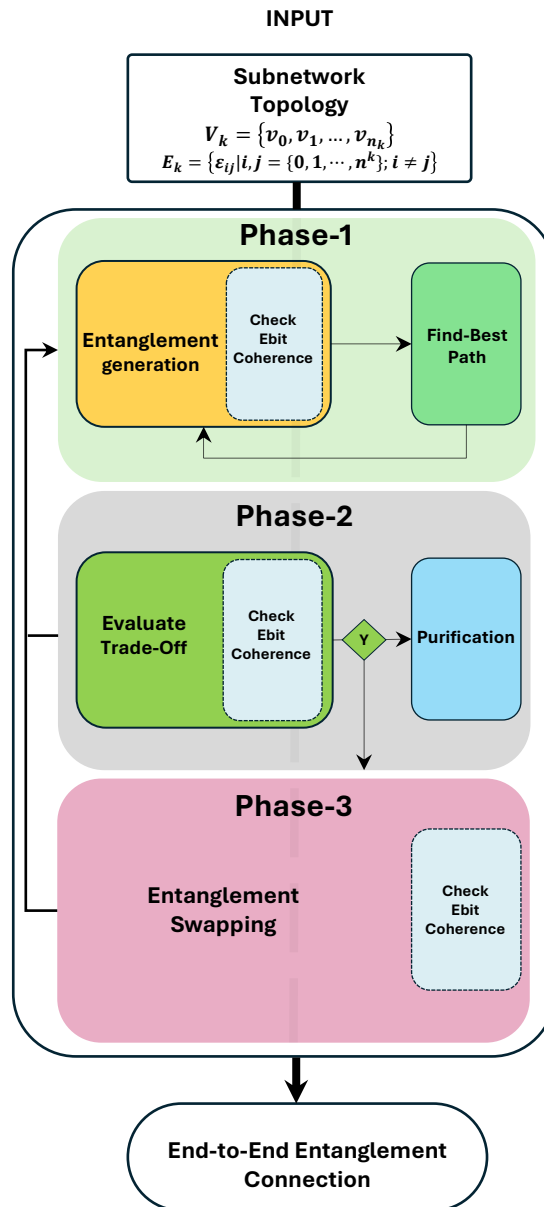


FIGURE 4.5: Segment-aware HQIN protocol. Phase 1: entanglement generation and path selection. Phase 2: fidelity–latency trade-off evaluation and purification. Phase 3: entanglement swapping to establish end-to-end entanglement.

4.4.1 Segment-Aware Method Description

We adopt a segment-based strategy [53], wherein each subnetwork \mathcal{G}_k is partitioned into logical segments to support concurrent entanglement generation and purification. A centralized controller (CC) coordinates quantum operations—including generation, fidelity estimation, banded purification, and entanglement swapping—across these segments. This parallelized orchestration improves throughput and bounds end-to-end latency τ_{e2e} , which encapsulates both quantum and classical delays.

Model Overview: The ebit generation model is based on bipartite entanglement distribution via photon-pair sources [94]. Entangled photons are generated at midpoint sources and distributed to endpoint nodes over either fiber or free-space links. Fidelity degrades due to noise, decoherence, and optical losses. As such, banded purification [107] is applied to restore high-fidelity ebits prior to entanglement swapping.

The full protocol is organized into the following phases:

1. **Entanglement Generation and Path Selection:** Each segment initiates local ebit generation using Type-II SPDC [109], where a GHz-rate laser is pumped through a BBO crystal. For a generation window of $W_{\text{gen}} = 1$ ms, approximately 10^6 pulses are emitted. The number of successful entangled pairs follows a binomial distribution with success probability p_{gen} , and resulting ebits are stored in quantum memory.
2. **Latency Modeling:** Segment-level latency is modeled using the modular framework:

$$\tau_{e2e} = \tau_{\text{find}} + \tau_{\text{gen}} + \tau_{\text{pur}} + \tau_{\text{swap}} + \tau_{\text{dist}} + \tau_{\text{comm}}, \quad (4.21)$$

where each term quantifies the time for path computation, entanglement generation, purification, swapping, inter-subnet distribution, and classical coordination. Per-link entanglement generation is given by:

$$t_{\text{gen}}(\varepsilon_{ij}) = t_{\text{proc}} + \frac{d_{ij} \cdot n_{\text{fiber}}}{c}, \quad (4.22)$$

for fiber links, and

$$t_{\text{gen}}^{\text{free}}(\theta(t)) = t_{\text{proc}} + \frac{d(\theta(t)) \cdot \eta_{\text{atm}}}{c}, \quad (4.23)$$

for satellite-ground free-space links, where $t_{\text{proc}} = 0.1 \mu\text{s}$ is the photon generation and initialization delay.

3. **Memory Allocation and Routing:** The CC identifies the optimal fidelity-aware path $\mathcal{P}_{\text{BestPath}}^{S,D}$ and allocates quantum memory resources along intermediate repeater nodes and head nodes to support subsequent operations.
4. **Fidelity–Latency Trade-off Evaluation (Phase 2):** For each request $\{v_m, v_n, \mathcal{F}_{\text{target}}, \tau_{\text{max}}\}$, the CC checks whether direct fidelity is sufficient. If the fidelity $\mathcal{F}_{\varepsilon_{ij}}$ for any link falls below the threshold, purification is invoked within allowed latency bounds.
5. **Banded Purification:** Fidelity enhancement is performed using a recursive purification model [104], [108]. The banded strategy permits purification only between ebits of comparable fidelity, reducing waste and improving success probability. Each round consumes a sacrificial ebit and incurs latency t_{pur} , contributing to total purification time $\tau_{\text{pur}} = \sum r_{\text{pur}}^{(ij)} \cdot t_{\text{pur}}(\varepsilon_{ij})$.
6. **Entanglement Swapping (Phase 3):** Once high-fidelity links are established, the CC triggers entanglement swapping at repeater and satellite nodes. Bell state measurements

are performed, extending the entangled path across segments. This final phase completes the E2E entanglement link, ready for quantum communication or teleportation.

4.5 Protocol Design Insights

To fulfill a request of the form $d(v_m, v_n, \mathcal{F}, l, \delta)$, the network must establish an entangled connection between nodes v_m and v_n while meeting a minimum fidelity \mathcal{F} , a latency threshold l , and additional constraints δ (e.g., reliability, visibility, or path length). We adopt an advance entanglement generation model [110], where ebits are produced prior to path confirmation to reduce on-demand delays.

Entangled photon pairs are generated using Type-II SPDC [109], in which a GHz-rate laser interacts with a nonlinear BBO crystal. These photons are distributed across fiber or free-space links, depending on the segment topology. At the receiving quantum nodes, transducers convert photonic qubits into long-lived matter qubits for memory storage [57], [111]. Due to the inherently low probability of pair generation via SPDC [112], only a small subset of trials yields usable ebits. Fidelity further degrades due to environmental factors such as noise, photon loss, and channel imperfections. To maintain high-quality links, fidelity is evaluated at regular intervals. If the fidelity of a link drops below an operational threshold, purification is performed using sacrificial ebits, following the banded strategy described earlier. Builder links intermediate connections with known fidelity are maintained as reusable quantum resources to support routing decisions and reduce repeated generation costs. The centralized controller (CC) evaluates viable routing paths from the source to destination, identifying satellite-visible head nodes when inter-subnet entanglement is required. If a line-of-sight to a satellite is available, half of the entangled pair is transmitted via free-space to the remote head node, while the other half is stored locally in quantum memory [90]. If no viable end-to-end route exists (due to lack of satellite alignment or insufficient fidelity), the system restarts the entanglement generation process for the affected links. Stored ebits degrade over time, following an exponential decay model $\mathcal{F}(t) = \mathcal{F}_0 \cdot e^{-t/\tau_{\text{coh}}}$, where τ_{coh} is the coherence time of the quantum memory. To minimize fidelity loss, routing decisions prioritize paths that maximize coherence longevity and minimize operational delay [113].

LEO satellites function as both entanglement distributors and quantum repeaters, enabling long-distance connectivity between subnetworks. The CC dynamically adapts routing to accommodate satellite motion, evolving link quality, and entanglement expiration [114]. The distribution latency τ_{dist} depends on the slant range between satellite and ground node, success probability of photon transmission, and memory synchronization constraints. Additional physical constraints such as atmospheric attenuation caused by scattering, turbulence, or beam misalignment further influence entanglement viability and latency [112], [115]. Once a high-fidelity link is successfully formed via satellite-mediated transmission, quantum teleportation is executed to complete secure end-to-end communication.

The proposed protocol supports fidelity–latency trade-offs through dynamic purification depth tuning. While deeper purification improves end-to-end fidelity, it also increases the overall latency τ_{e2e} , especially for segments involving satellite-based communication [108]. The segment-aware structure and centralized orchestration ensure that these trade-offs are optimized on a per-request basis, balancing resource usage and quality of service.

- $F_{\varepsilon_{ij}}$: Initial fidelity of the entangled pair over link (i, j)
- r_{ij} : Number of purification rounds executed on the active link (i, j) where $r < \frac{c_{ij}}{2}$ where c_{ij} indicates the capacity of the links meaning how many ebits has been distributed

- p_{gen} : Probability of successfully generating an entangled pair on link (i, j) per pulse is equal for all the links once we have established the type of source and its parameters
- W_{gen} : Global generation window valid for all the subnetworks k
- R_{pulse} : Pulse rate of the entanglement source (e.g., 10^9 pulses/s)
- L : Number of entanglement swapping levels required along the path \mathcal{P}_{sd}
- λ : Trade-off parameter to balance latency and fidelity
- γ : Weight for the optional penalty based on overall success probability

This formulation inherently penalizes paths that incur high latency per unit of fidelity and rewards those that deliver high fidelity with minimal time. The Central Controller (CC) dynamically adapts λ based on application requirements:

- High-fidelity services: lower λ , emphasis on improving $\mathcal{F}^{(t)}$,
- Delay-sensitive tasks: higher λ , favoring low τ_{e2e} .

4.5.1 Link-Level Fidelity After Purification

The fidelity of a link (i, j) after r_{ij} purification rounds is given recursively by

$$F_{ij}^{(r)} = \frac{F_{ij}^{(r-1)} \cdot F_{ij}}{F_{ij}^{(r-1)} \cdot F_{ij} + (1 - F_{ij}^{(r-1)})(1 - F_{ij})}, \quad F_{ij}^{(0)} = F_{ij} \quad (4.24)$$

The corresponding Werner parameter is then calculated as:

$$w_{ij} = \frac{4f_{ij}^{(r)} - 1}{3} \quad (4.25)$$

4.5.2 Purification Success Probability and Generation Requirements

The probability that a purification round succeeds at fidelity f is:

$$p_{\text{pur}}(F) = F^2 + (1 - F)^2 \quad (4.26)$$

Then, the number of ebits required to perform r_{ij} purification rounds is:

$$N_{ij}^{\text{min}} = \frac{2^{r_{ij}}}{P_{\text{pur}}(F_{\varepsilon_{ij}})^{r_{ij}}} \quad (4.27)$$

Thus, the minimum required generation window must satisfy:

$$W_{\text{gen}} \geq \max_{(i,j) \in \mathcal{P}} \left(\frac{N_{ij}^{\text{min}}}{R_{\text{pulse}} \cdot p_{\text{gen}}^{ij} \cdot p_{\text{dist}}^{ij}(\theta)} \right) \quad (4.28)$$

4.5.3 Cumulative End-to-End Success Probability

The total success probability of establishing a high-fidelity end-to-end link is:

$$P_{\text{succ}} = \left(\prod_{(i,j) \in \mathcal{P}} p_{\text{gen}}^{ij} \cdot p_{\text{dist}}^{ij}(\theta) \cdot P_{\text{pur}}(F_{\varepsilon_{ij}})^{r_{ij}} \right) \cdot (P_{\text{swap}})^L \quad (4.29)$$

4.6 System Model and Problem Formulation

This section presents the physical and mathematical framework of the satellite-based quantum communication network and its coupling with the Proximal Policy Optimization (PPO) agent. The aim is to maximize long-term entanglement generation while respecting communication, energy, and time constraints. We also ensure that the learning framework satisfies the Markov property by restricting each training episode to a consistent satellite-visibility window.

4.6.1 Geometric and Channel Model

Consider a low Earth orbit (LEO) satellite at altitude H communicating simultaneously with two quantum ground stations (QGSs), denoted as QGS_S and QGS_T. The geometric configuration of the link is defined by the *slant range*, which represents the line-of-sight distance between the satellite and a ground terminal as a function of its elevation angle θ :

$$L(\theta) = \sqrt{H^2 + 2HR_E + R_E^2 - 2R_E(H + R_E) \cos(\pi - \theta)}, \quad (4.30)$$

where R_E is the Earth's radius. The elevation angle θ varies dynamically with satellite motion and determines both the atmospheric attenuation and free-space loss of the link.

The probability of successful photon transmission from the satellite to each ground station is modeled as:

$$P_{\text{link}}(\theta) = \eta_{\text{tx}} \eta_{\text{rx}} T_{\text{atm}}(\theta) \exp(-\alpha L(\theta)), \quad (4.31)$$

where η_{tx} and η_{rx} denote the transmitter and receiver efficiencies, $T_{\text{atm}}(\theta)$ captures atmospheric transmittance, and α is the attenuation coefficient.

4.6.2 Entanglement Generation and Swapping

The satellite simultaneously generates entangled photon pairs directed toward both ground stations. The individual link success probabilities s_A and s_B correspond to QGS_S and QGS_T, respectively:

$$s_A = P_{\text{link}}(\theta_A), \quad s_B = P_{\text{link}}(\theta_B). \quad (4.32)$$

The end-to-end probability of producing an entangled pair is governed by the joint success of both links and the Bell-state measurement (BSM) efficiency:

$$P_{\text{ent}} = s_A s_B P_{\text{BSM}} \eta_{\text{mem}} F_{\text{pair}}, \quad (4.33)$$

where P_{BSM} is the BSM success probability, η_{mem} is the quantum memory survival factor, and F_{pair} is the fidelity of the generated pair. The memory efficiency term is computed as:

$$\eta_{\text{mem}} = \exp\left(-\frac{2 \max(L_A, L_B)}{c\tau_{\text{coh}}}\right) \eta_{\text{ret}}, \quad (4.34)$$

where c is the speed of light, τ_{coh} is the coherence lifetime of the quantum memory, and η_{ret} denotes its retrieval efficiency.

Each successful end-to-end BSM swap contributes one entangled pair to the communication network. The PPO agent's goal is to schedule satellite-ground link selections to maximize this rate under realistic constraints.

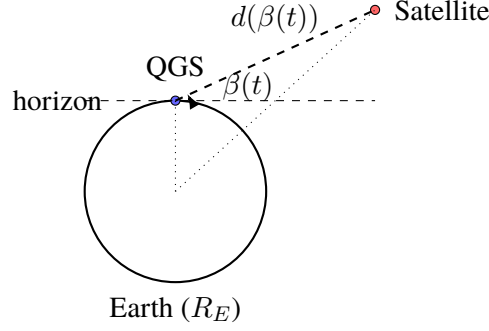


FIGURE 4.6: Slant range $d(\beta(t))$ with respect to the elevation angle, zenith angle $\theta(t)$, and local horizon at a Quantum Ground Station (QGS) for satellite-based entanglement distribution.

4.6.3 Markov Decision Process Definition

The satellite network and the agent form a Markov Decision Process (MDP) defined by the tuple

$$\mathcal{M} = (\mathcal{S}, \mathcal{A}, P, R, \gamma),$$

where each element is defined as follows:

State s_t : The observable environment variables at time t are represented as:

$$s_t = [L_A(t), L_B(t), \theta_A(t), \theta_B(t), P_{\text{link}}(\theta_A), P_{\text{link}}(\theta_B), E_{\text{bat}}, t_{\text{step}}], \quad (4.35)$$

where E_{bat} denotes the residual energy of the satellite, and t_{step} is the local time index. To ensure the **Markov property**, each training episode is constrained to a consistent visibility window where orbital dynamics evolve smoothly and previous state histories are not required.

Action a_t : The PPO agent selects one satellite-pair combination from the visible set, i.e.,

$$a_t \in \{\text{available satellite-pair links at time } t\}.$$

This action defines which satellite will be used to perform the next BSM swap operation.

Normalized reward. For a target of N_{target} pairs in a time window of duration T_w , if the target is achieved after Δt seconds, then the reward is

$$r_t = \alpha \frac{N_{\text{success}}}{N_{\text{target}}} + \beta \left(1 - \frac{\Delta t}{T_w} \right), \quad (4.36)$$

where (α, β) balance the accuracy and timeliness of success. If only poor satellites are visible (e.g., low elevation), the reward is normalized by the expected achievable rate under those conditions.

4.6.4 Optimization Objective

The PPO agent aims to maximize the long-term cumulative reward under time and energy constraints:

$$\begin{aligned} \max_{\pi_\theta} \quad & J(\pi_\theta) = \mathbb{E}_{\pi_\theta} \left[\sum_{t=0}^T \gamma^t r_t \right] \\ \text{s.t.} \quad & T_{\text{achieved}} \leq T_{\text{max}}, \\ & E_{\text{used}} \leq E_{\text{max}}. \end{aligned} \quad (4.37)$$

The PPO algorithm optimizes the following clipped surrogate objective:

$$L^{\text{PPO}}(\theta) = \mathbb{E}_t \left[\min(r_t(\theta) \hat{A}_t, \text{clip}(r_t(\theta), 1 - \epsilon, 1 + \epsilon) \hat{A}_t) \right], \quad (4.38)$$

where \hat{A}_t is the estimated advantage function derived from the Generalized Advantage Estimation (GAE) and ϵ controls the policy update trust region.

4.6.5 Discussion

The proposed formulation integrates the physical dynamics of quantum satellite communication with reinforcement learning. Each episode corresponds to a fixed-duration satellite visibility window, ensuring that the state transitions obey the Markov property. The PPO agent continuously observes physical states (e.g., elevation, range, memory decay) and learns to maximize entanglement yield within the available time and energy budget, effectively bridging the physics-based model with adaptive decision-making under uncertainty.

4.7 Scheduling Implications

Because $R_{\text{ent}}(\theta)$ grows sharply with elevation, passes near zenith yield the highest entanglement rates. Below roughly 15° – 20° elevation, link losses (atmospheric + turbulence) become prohibitive. This model thus provides the quantitative basis for satellite–GS scheduling, adaptive power allocation, and entanglement-rate prediction in quantum network simulations.

Time and Horizon. We discretize time with step Δt (e.g., $\Delta t = 1$ ms). Each episode is a *consistent visibility window* of duration $T = H\Delta t$, ensuring Markovian dynamics within the window.

4.8 Flow of PPO-Based Entanglement Scheduling

Figure shows the fundamentals of PPO algorithm, where for each window of communication, PPO receives a request to connect two ground stations. PPO initializes the protocol and selects the best currently available satellite among all available satellites which are visible to both ground stations. The selected satellite produces entangled photons and simultaneously transmits them toward both ground stations. The entanglement is achieved probabilistically at both ends. The process repeats until the window of communication, and for each discrete time, a decision is made with the aim to maximize entangled photons at both ground stations during the complete communication window. PPO stores each interaction. Once the buffer is full, the training starts to optimize the selection policy. For each communication window, different ground station pair requests are handled.

4.9 Results and Discussion

Figure 4.8, and 4.9 show the reward convergence for a single pair request, i.e., when the PPO has to make decisions for satellite selection for one ground station pair for the whole training time. The total available satellite varies during the training time since the movement of the satellite changes the number of available satellites during the communication window. This creates fluctuation in the reward.

Figures 4.10 and 4.11 show the reward convergence as the PPO scheduling deals with multiple requests coming from multiple ground station pairs. The variation in available satellites, angles, slant range, and probabilistic nature of entanglement pair generation play a huge role in reward convergence. Nevertheless, the algorithm learns and aims to maximize the objective.

Finally, Figure 4.12 shows the reward maximization from a physical point of view, as it is known that the maximum engagement is produced when zenith is maximized. The algorithm learns and aims to choose satellites with maximum zenith angle, which ultimately maximizes the reward.

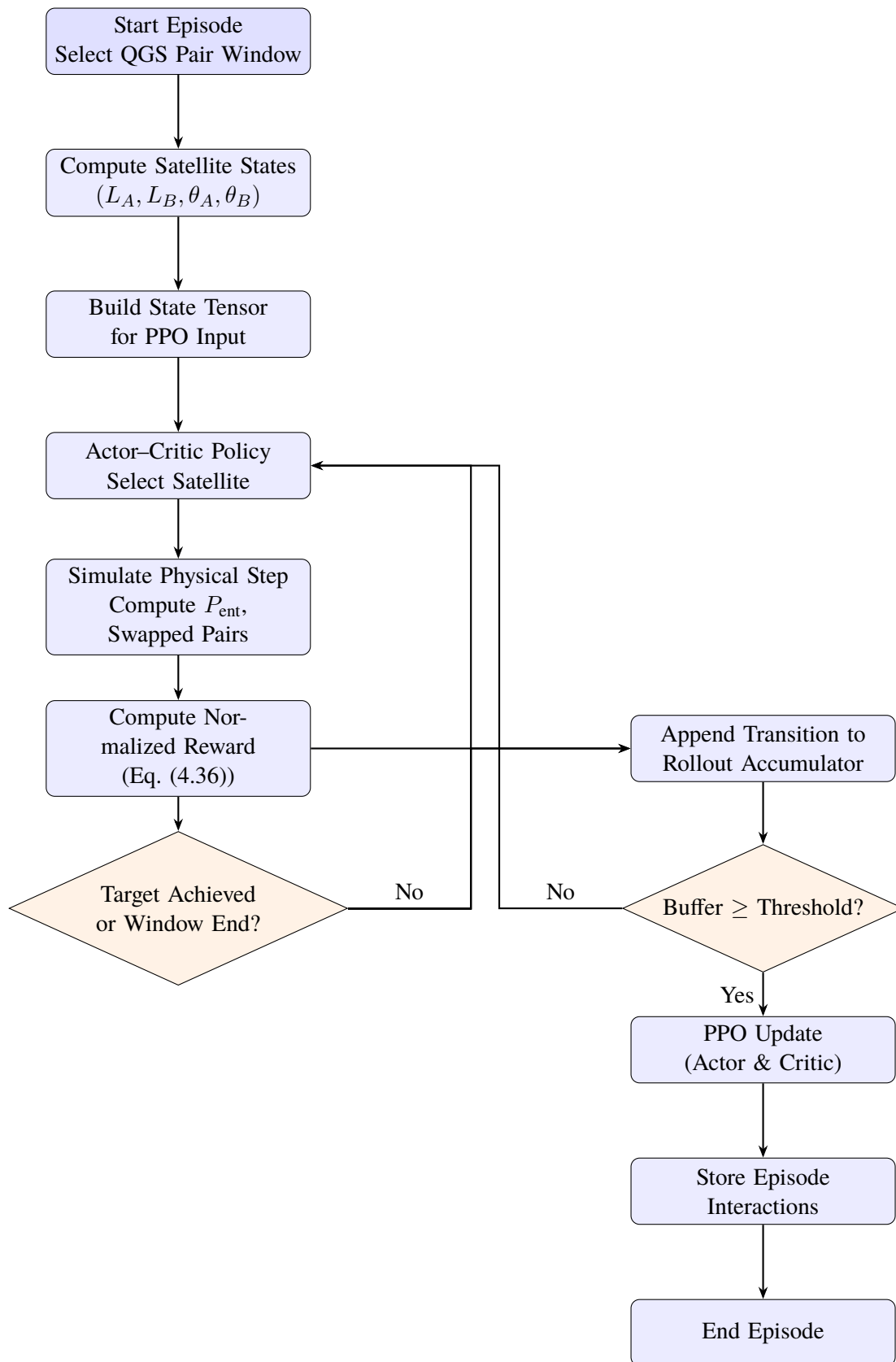


FIGURE 4.7: PPO update is triggered *only* when the rollout buffer reaches a threshold; per-step Experience is always accumulated, independent of the target/window condition.

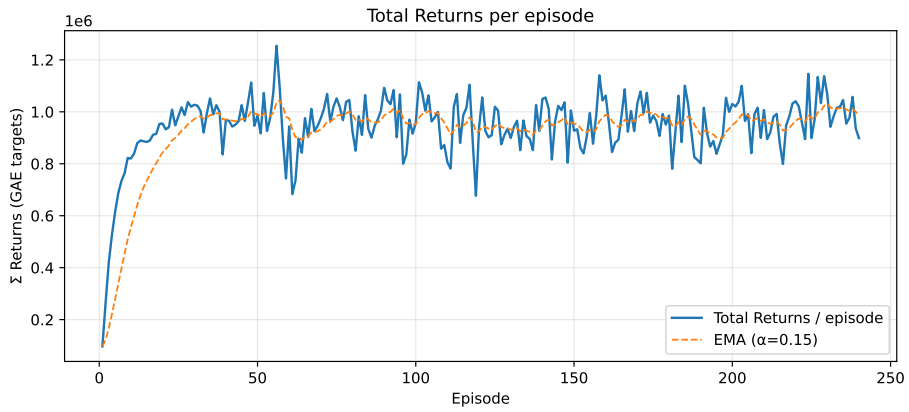


FIGURE 4.8: Sum of Rewards when a single source target pair request



FIGURE 4.9: Sum of Rewards when a single source target pair request

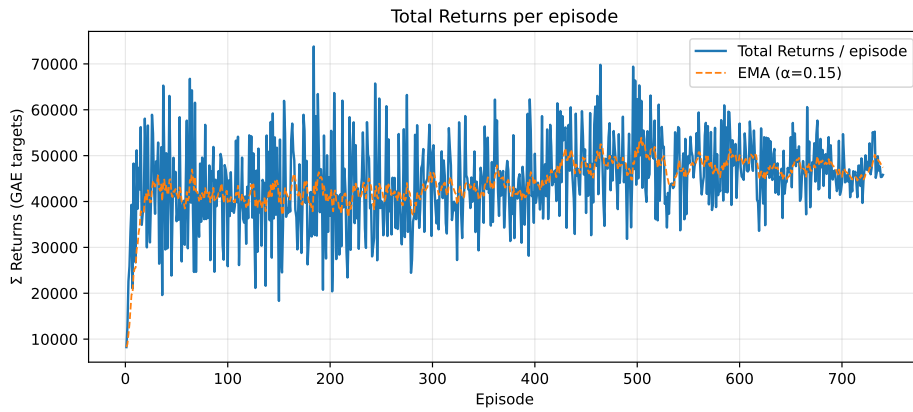


FIGURE 4.10: Sum of Rewards for multiple source pair requests for the schedule

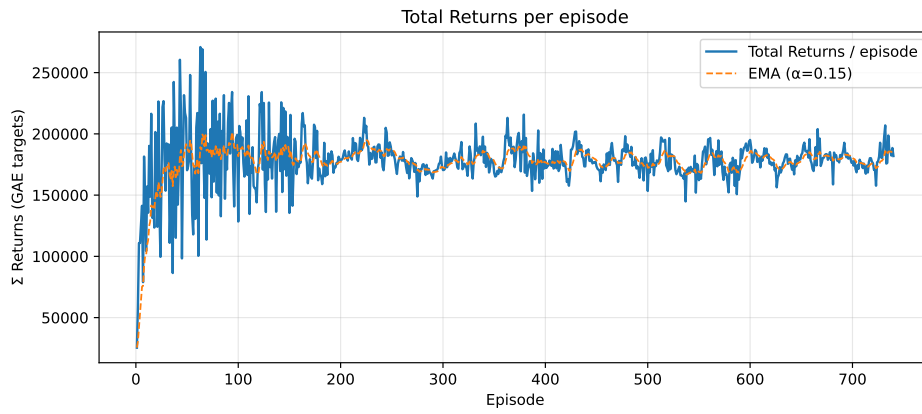


FIGURE 4.11: Sum of Rewards for multiple source pair requests for the schedule

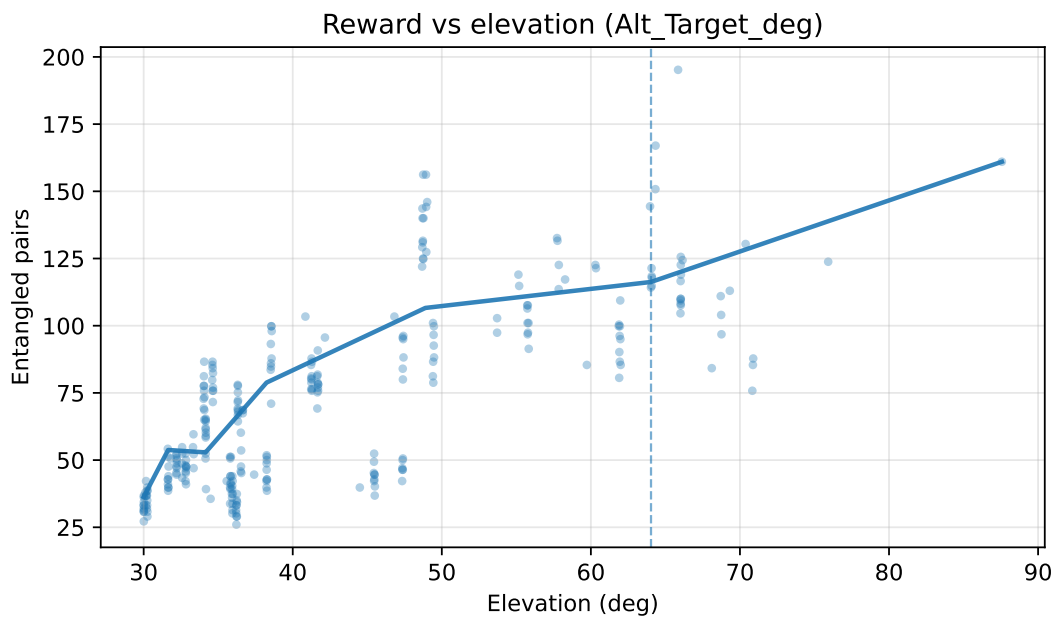


FIGURE 4.12: Reward for scheduled satellite's angles

Conclusions and Future Works

The thesis establishes a comprehensive framework for designing efficient, data-driven scheduling and random access policies across two distinct communication paradigms: low-energy sensor networks and highly dynamic quantum satellite networks. The research demonstrates that providing sufficient information for decision-making is vital for system adaptability and performance. It further establishes that adopting adaptive, data-informed strategies—rather than static or fixed policies—is fundamentally important to cope with the dynamic and heterogeneous nature of modern communication environments.

Chapter 1 contributes by presenting a decentralized random access mechanism that significantly reduces energy consumption without compromising data freshness. This design represents a crucial advancement toward achieving massive connectivity among energy-constrained sensor nodes while maintaining timely information updates.

Chapter 3 extends this analysis to centralized decision-making, showing that global network awareness can further optimize system performance. The findings reveal that even limited feedback is sufficient to preserve information freshness in low-energy devices. Moreover, the division of users into near and far groups enhances energy efficiency, particularly when devices rely on wireless energy harvesting, thereby maximizing network lifetime and sustainability.

Finally, Chapter 4 demonstrates that the proposed adaptive scheduling approach is equally effective in managing highly volatile quantum satellite networks. The results indicate that, when additional resources are available, dynamically selecting the optimal configuration at each scheduling instance—rather than adhering to a fixed selection—leads to improved stability, resource utilization, and overall network performance.

Bibliography

- [1] T. Park and W. Saad, “Distributed learning for low latency machine type communication in a massive internet of things,” *IEEE Internet of Things Journal*, vol. 6, no. 3, pp. 5562–5576, Jun. 2019. DOI: [10.1109/JIOT.2019.2903832](https://doi.org/10.1109/JIOT.2019.2903832).
- [2] M. H. C. Garcia and et al., “A tutorial on 5g nr v2x communications,” *IEEE Communications Surveys & Tutorials*, vol. 23, no. 3, pp. 1972–2026, 2021. DOI: [10.1109/COMST.2021.3057017](https://doi.org/10.1109/COMST.2021.3057017).
- [3] E. C. Strinati and et al., “Goal-oriented and semantic communication in 6g ai-native networks: The 6g-goals approach,” in *2024 Joint European Conference on Networks and Communications & 6G Summit (EuCNC/6G Summit)*, Antwerp, Belgium, 2024, pp. 1–6. DOI: [10.1109/EuCNC/6GSummit60053.2024.10597087](https://doi.org/10.1109/EuCNC/6GSummit60053.2024.10597087).
- [4] G. Liva, “Graph-based analysis and optimization of contention resolution diversity slotted aloha,” *IEEE Transactions on Communications*, vol. 59, no. 2, pp. 477–487, 2011. DOI: [10.1109/TCOMM.2010.120710.100054](https://doi.org/10.1109/TCOMM.2010.120710.100054).
- [5] J. Holm, F. Chiariotti, A. E. Kalør, B. Soret, T. B. Pedersen, and P. Popovski, “Goal-oriented scheduling in sensor networks with application timing awareness,” *IEEE Transactions on Communications*, vol. 71, no. 8, pp. 4513–4527, Aug. 2023. DOI: [10.1109/TCOMM.2023.3282256](https://doi.org/10.1109/TCOMM.2023.3282256).
- [6] Y. Liu, B. Clerckx, and P. Popovski, “Network slicing for embb, urllc, and mmhc: An uplink rate-splitting multiple access approach,” *IEEE Transactions on Wireless Communications*, vol. 23, no. 3, pp. 2140–2152, Mar. 2024. DOI: [10.1109/TWC.2023.3295804](https://doi.org/10.1109/TWC.2023.3295804).
- [7] J. Haghghat and T. M. Duman, “Analysis of coded slotted aloha with energy harvesting nodes for perfect and imperfect packet recovery scenarios,” *IEEE Transactions on Wireless Communications*, vol. 22, no. 11, pp. 7424–7437, Nov. 2023. DOI: [10.1109/TWC.2023.3250550](https://doi.org/10.1109/TWC.2023.3250550).
- [8] J. Haghghat and T. M. Duman, “An energy-efficient feedback-aided irregular repetition slotted aloha scheme and its asymptotic performance analysis,” *IEEE Transactions on Wireless Communications*, vol. 22, no. 12, pp. 9808–9820, 2023. DOI: [10.1109/TWC.2023.3273616](https://doi.org/10.1109/TWC.2023.3273616).
- [9] Z. Chen, Y. Feng, Z. Tian, Y. Jia, M. Wang, and T. Q. S. Quek, “Energy efficiency optimization for irregular repetition slotted aloha-based massive access,” *IEEE Wireless Communications Letters*, vol. 11, no. 5, pp. 982–986, May 2022. DOI: [10.1109/LWC.2022.3151931](https://doi.org/10.1109/LWC.2022.3151931).
- [10] N. A. Mitsiou, P. N. Gavriilidis, P. D. Diamantoulakis, and G. K. Karagiannidis, “Wireless powered multiaccess edge computing with slotted aloha,” *IEEE Communications Letters*, vol. 27, no. 1, pp. 273–277, Jan. 2023. DOI: [10.1109/LCOMM.2022.3211190](https://doi.org/10.1109/LCOMM.2022.3211190).
- [11] K.-H. Ngo, G. Durisi, and P. Popovski, “Information age and correctness for energy harvesting devices with random access,” *arXiv preprint*, vol. arXiv:2501.14522, 2025.

- [12] I. Hmedoush, P. Gu, C. Adjih, P. Mühlethaler, and A. Serhrouchni, “Ds-irsa: A deep reinforcement learning and sensing based irsa,” in *GLOBECOM 2023 – 2023 IEEE Global Communications Conference*, Kuala Lumpur, Malaysia, 2023, pp. 2790–2795. doi: [10.1109/GLOBECOM54140.2023.10437376](https://doi.org/10.1109/GLOBECOM54140.2023.10437376).
- [13] Y. Feng et al., “Irregular repetition slotted aloha scheme with short packets under rayleigh fading channels,” *IEEE Transactions on Vehicular Technology*, vol. 73, no. 5, pp. 6700–6713, 2024. doi: [10.1109/TVT.2023.3341449](https://doi.org/10.1109/TVT.2023.3341449).
- [14] C. R. Srivatsa and C. R. Murthy, “Channel state information based user censoring in irregular repetition slotted aloha,” in *ICC 2023 – IEEE International Conference on Communications*, Rome, Italy, 2023, pp. 698–703. doi: [10.1109/ICC45041.2023.10278965](https://doi.org/10.1109/ICC45041.2023.10278965).
- [15] J. Choi, “Noma-based random access with multichannel aloha,” *IEEE Journal on Selected Areas in Communications*, vol. 35, no. 12, pp. 2736–2743, 2017. doi: [10.1109/JSAC.2017.2766778](https://doi.org/10.1109/JSAC.2017.2766778).
- [16] Y. Liu, L. X. Cai, Q. Chen, H. Zhang, F. Hou, and T. H. Luan, “Minimizing age of information in nonorthogonal random access networks,” *IEEE Internet of Things Journal*, vol. 11, no. 14, pp. 24 886–24 902, Jul. 2024. doi: [10.1109/JIOT.2024.3388019](https://doi.org/10.1109/JIOT.2024.3388019).
- [17] W. Yu, C. H. Foh, A. U. Quddus, Y. Liu, and R. Tafazolli, “Throughput analysis and user barring design for uplink noma-enabled random access,” *IEEE Transactions on Wireless Communications*, vol. 20, no. 10, pp. 6298–6314, 2021. doi: [10.1109/TWC.2021.3073326](https://doi.org/10.1109/TWC.2021.3073326).
- [18] I. N. A. Ramatryana and S. Y. Shin, “Priority access in noma-based slotted aloha for overload 6g massive iot,” *IEEE Communications Letters*, vol. 26, no. 12, pp. 3064–3068, Dec. 2022. doi: [10.1109/LCOMM.2022.3208900](https://doi.org/10.1109/LCOMM.2022.3208900).
- [19] Y. Ko and J. Choi, “Reinforcement learning for noma-aloha under fading,” *IEEE Transactions on Communications*, vol. 70, no. 10, pp. 6861–6873, Oct. 2022. doi: [10.1109/TCOMM.2022.3198125](https://doi.org/10.1109/TCOMM.2022.3198125).
- [20] Y. Li and K.-W. Chin, “Energy-aware irregular slotted aloha methods for wireless-powered iot networks,” *IEEE Internet of Things Journal*, vol. 9, no. 14, pp. 11 784–11 795, 2022. doi: [10.1109/JIOT.2021.3132006](https://doi.org/10.1109/JIOT.2021.3132006).
- [21] E. Nisioti and N. Thomos, “Fast q-learning for improved finite length performance of irregular repetition slotted aloha,” *IEEE Transactions on Cognitive Communications and Networking*, vol. 6, no. 2, pp. 844–857, 2020. doi: [10.1109/TCCN.2019.2957224](https://doi.org/10.1109/TCCN.2019.2957224).
- [22] J. Hribar and I. Dusparic, “Enabling deep reinforcement learning on energy constrained devices at the edge of the network,” in *2022 IEEE Wireless Communications and Networking Conference (WCNC)*, Austin, TX, USA, 2022, pp. 2547–2552. doi: [10.1109/WCNC51071.2022.9771901](https://doi.org/10.1109/WCNC51071.2022.9771901).
- [23] E. Delfani and N. Pappas, “Optimizing information freshness in constrained iot systems: A token-based approach,” *IEEE Transactions on Communications*, pp. 1–1, 2024. doi: [10.1109/TCOMM.2024.3524026](https://doi.org/10.1109/TCOMM.2024.3524026).
- [24] S. Saha, V. B. Sukumaran, and C. R. Murthy, “On the minimum average age of information in irsa for grant-free mmfc,” *IEEE Journal on Selected Areas in Communications*, vol. 39, no. 5, pp. 1441–1455, 2021. doi: [10.1109/JSAC.2021.3065065](https://doi.org/10.1109/JSAC.2021.3065065).

- [25] F. Chiariotti, A. Munari, L. Badia, and P. Popovski, "Peak age of incorrect information of reactive aloha reporting under imperfect feedback," *arXiv preprint*, vol. arXiv:2411.08487, 2024.
- [26] E. Delfani and N. Pappas, "Semantics-aware status updates with energy harvesting devices: Query version age of information," in *2024 22nd International Symposium on Modeling and Optimization in Mobile, Ad Hoc, and Wireless Networks (WiOpt)*, 2024, pp. 177–184.
- [27] K.-H. Ngo, D. N. Nguyen, and T.-M. D. Thi, "Protocol design for irregular repetition slotted aloha with energy harvesting to maintain information freshness," in *2025 IEEE Wireless Communications and Networking Conference (WCNC)*, Milan, Italy, 2025, pp. 1–6. doi: [10.1109/WCNC61545.2025.10978698](https://doi.org/10.1109/WCNC61545.2025.10978698).
- [28] K.-H. Ngo, G. Durisi, A. Munari, F. Lázaro, and A. G. i. Amat, "Timely status updates in slotted aloha networks with energy harvesting," *IEEE Transactions on Communications*, pp. 1–1, 2025. doi: [10.1109/TCOMM.2025.3548035](https://doi.org/10.1109/TCOMM.2025.3548035).
- [29] K. Lee and H.-H. Choi, "Energy-efficient resource allocation for bidirectional wireless power and information transfer over interference channels," *Journal of Network and Computer Applications*, vol. 227, p. 103 887, 2024, ISSN: 1084-8045. doi: <https://doi.org/10.1016/j.jnca.2024.103887>. [Online]. Available: <https://www.sciencedirect.com/science/article/pii/S108480452400064X>.
- [30] Y. Huang, J. Jiao, Y. Wang, S. Wu, R. Lu, and Q. Zhang, "G-sc-irsa: Graph-based spatially coupled irsa for age-critical grant-free massive access," *IEEE Internet of Things Journal*, vol. 10, no. 10, pp. 9007–9021, May 2023. doi: [10.1109/JIOT.2022.3232568](https://doi.org/10.1109/JIOT.2022.3232568).
- [31] H.-H. Choi, W. Shin, M. Levorato, and H. V. Poor, "Harvest-or-access: Slotted aloha for wireless powered communication networks," *IEEE Transactions on Vehicular Technology*, vol. 68, no. 11, pp. 11 394–11 398, 2019. doi: [10.1109/TVT.2019.2934439](https://doi.org/10.1109/TVT.2019.2934439).
- [32] Y. Huang et al., "Age of information minimization for frameless aloha in grant-free massive access," *IEEE Transactions on Wireless Communications*, vol. 22, no. 12, pp. 9778–9792, 2023. doi: [10.1109/TWC.2023.3273531](https://doi.org/10.1109/TWC.2023.3273531).
- [33] Y. Emami, K. Li, Y. Niu, and E. Tovar, "Aoi minimization using multi-agent proximal policy optimization in uavs-assisted sensor networks," in *ICC 2023 - IEEE International Conference on Communications*, Rome, Italy, 2023, pp. 228–233. doi: [10.1109/ICC45041.2023.10278748](https://doi.org/10.1109/ICC45041.2023.10278748).
- [34] Y. Huang et al., "Age of information minimization for frameless aloha in grant-free massive access," *IEEE Transactions on Wireless Communications*, vol. 22, no. 12, pp. 9778–9792, 2023. doi: [10.1109/TWC.2023.3273531](https://doi.org/10.1109/TWC.2023.3273531).
- [35] M. Klügel, M. H. Mamduhi, S. Hirche, and W. Kellerer, "Aoi-penalty minimization for networked control systems with packet loss," in *IEEE INFOCOM 2019 - IEEE Conference on Computer Communications Workshops (INFOCOM WKSHPS)*, 2019, pp. 189–196. doi: [10.1109/INFCOMW.2019.8845106](https://doi.org/10.1109/INFCOMW.2019.8845106).
- [36] G. Iacovelli, G. Grieco, A. Petrosino, L. A. Grieco, and G. Boggia, "Fair energy and data rate maximization in uav-powered iot-satellite integrated networks," *IEEE Transactions on Communications*, vol. 72, no. 4, pp. 2457–2469, 2024. doi: [10.1109/TCOMM.2023.3343417](https://doi.org/10.1109/TCOMM.2023.3343417).

- [37] F. Guo, F. R. Yu, H. Zhang, H. Ji, M. Liu, and V. C. M. Leung, "Adaptive resource allocation in future wireless networks with blockchain and mobile edge computing," *IEEE Transactions on Wireless Communications*, vol. 19, no. 3, pp. 1689–1703, 2019. DOI: [10.1109/TWC.2019.2951403](https://doi.org/10.1109/TWC.2019.2951403).
- [38] X. Mu and Y. Liu, "Exploiting semantic communication for non-orthogonal multiple access," *IEEE Journal on Selected Areas in Communications*, vol. 41, no. 8, pp. 2563–2576, 2023. DOI: [10.1109/JSAC.2023.3288242](https://doi.org/10.1109/JSAC.2023.3288242).
- [39] S. Li, H.-C. Yang, and F. Hu, "Joint transmission mode selection and scheduling for aoi minimization in noma-capable wp-iot networks: A deep transfer learning solution," *IEEE Transactions on Communications*, vol. 73, no. 8, pp. 5805–5816, 2025. DOI: [10.1109/TCOMM.2025.3538825](https://doi.org/10.1109/TCOMM.2025.3538825).
- [40] J. Youn et al., "Marl-based access control for grant-free nonorthogonal random access in udn," *IEEE Internet of Things Journal*, vol. 11, no. 17, pp. 28 421–28 436, 2024. DOI: [10.1109/JIOT.2024.3404418](https://doi.org/10.1109/JIOT.2024.3404418).
- [41] X. Chen, K. Gatsis, H. Hassani, and S. S. Bidokhti, "Age of information in random access channels," *IEEE Transactions on Information Theory*, vol. 68, no. 10, pp. 6548–6568, 2022. DOI: [10.1109/TIT.2022.3180965](https://doi.org/10.1109/TIT.2022.3180965).
- [42] O. T. Yavascan and E. Uysal, "Analysis of slotted aloha with an age threshold," *IEEE Journal on Selected Areas in Communications*, vol. 39, no. 5, pp. 1456–1470, 2021. DOI: [10.1109/JSAC.2021.3065043](https://doi.org/10.1109/JSAC.2021.3065043).
- [43] J. Choi, "Noma-based random access with multichannel aloha," *IEEE Journal on Selected Areas in Communications*, vol. 35, no. 12, pp. 2736–2743, 2017. DOI: [10.1109/JSAC.2017.2766778](https://doi.org/10.1109/JSAC.2017.2766778).
- [44] Y. Ko and J. Choi, "Reinforcement learning for noma-aloah under fading," *IEEE Transactions on Communications*, vol. 70, no. 10, pp. 6861–6873, 2022. DOI: [10.1109/TCOMM.2022.3198125](https://doi.org/10.1109/TCOMM.2022.3198125).
- [45] Y. Liu, L. X. Cai, Q. Chen, H. Zhang, F. Hou, and T. H. Luan, "Minimizing age of information in nonorthogonal random access networks," *IEEE Internet of Things Journal*, vol. 11, no. 14, pp. 24 886–24 902, 2024. DOI: [10.1109/JIOT.2024.3388019](https://doi.org/10.1109/JIOT.2024.3388019).
- [46] Z. Shi, X. Xie, H. Lu, H. Yang, J. Cai, and Z. Ding, "Deep reinforcement learning-based multidimensional resource management for energy harvesting cognitive noma communications," *IEEE Transactions on Communications*, vol. 70, no. 5, pp. 3110–3125, 2022. DOI: [10.1109/TCOMM.2021.3126626](https://doi.org/10.1109/TCOMM.2021.3126626).
- [47] F. Song et al., "Aoi and energy tradeoff for aerial-ground collaborative mec: A multi-objective learning approach," *IEEE Transactions on Mobile Computing*, vol. 23, no. 12, pp. 11 278–11 294, 2024. DOI: [10.1109/TMC.2024.3394568](https://doi.org/10.1109/TMC.2024.3394568).
- [48] E. C. Strinati et al., "Goal-oriented and semantic communication in 6g ai-native networks: The 6g-goals approach," in *2024 Joint European Conference on Networks and Communications & 6G Summit (EuCNC/6G Summit)*, Antwerp, Belgium, 2024, pp. 1–6. DOI: [10.1109/EuCNC/6GSummit60053.2024.10597087](https://doi.org/10.1109/EuCNC/6GSummit60053.2024.10597087).
- [49] Z. Utkovski et al., "Semantic communication for edge intelligence: Theoretical foundations and implications on protocols," *IEEE Internet of Things Magazine*, vol. 6, no. 4, pp. 48–53, 2023. DOI: [10.1109/IOTM.001.2300167](https://doi.org/10.1109/IOTM.001.2300167).
- [50] F. Guo, F. R. Yu, H. Zhang, X. Li, H. Ji, and V. C. M. Leung, "Enabling massive iot toward 6g: A comprehensive survey," *IEEE Internet of Things Journal*, vol. 8, no. 15, pp. 11 891–11 915, 2021. DOI: [10.1109/JIOT.2021.3063684](https://doi.org/10.1109/JIOT.2021.3063684).

- [51] N. Cordeschi, W. Zhuang, R. Tafazolli, and Y. Gao, "Optimal random access strategies for trigger-based multiple-packet reception channels," *IEEE Transactions on Mobile Computing*, vol. 23, no. 3, pp. 2303–2320, 2024. doi: [10.1109/TMC.2023.3258750](https://doi.org/10.1109/TMC.2023.3258750).
- [52] W. Dai, T. Peng, and M. Z. Win, "Optimal Remote Entanglement Distribution," en, *IEEE J. Select. Areas Commun.*, vol. 38, no. 3, pp. 540–556, Mar. 2020, issn: 0733-8716, 1558-0008. doi: [10.1109/JSAC.2020.2969005](https://doi.org/10.1109/JSAC.2020.2969005). Accessed: Mar. 20, 2025. [Online]. Available: <https://ieeexplore.ieee.org/document/8967073/>.
- [53] Z. Li et al., "Efficient Remote Entanglement Distribution in Quantum Networks: A Segment-Based Method," en, *IEEE Trans. Netw. Serv. Manage.*, vol. 21, no. 1, pp. 249–265, Feb. 2024, issn: 1932-4537, 2373-7379. doi: [10.1109/TNSM.2023.3296672](https://doi.org/10.1109/TNSM.2023.3296672). Accessed: Mar. 4, 2025. [Online]. Available: <https://ieeexplore.ieee.org/document/10185987/>.
- [54] K. Chakraborty, D. Elkouss, B. Rijsman, and S. Wehner, "Entanglement Distribution in a Quantum Network, a Multi-Commodity Flow-Based Approach," en, *IEEE Trans. Quantum Eng.*, vol. 1, pp. 1–21, 2020, arXiv:2005.14304 [quant-ph], issn: 2689-1808. doi: [10.1109/TQE.2020.3028172](https://doi.org/10.1109/TQE.2020.3028172). Accessed: Mar. 8, 2025. [Online]. Available: <http://arxiv.org/abs/2005.14304>.
- [55] A. Chang, Y. Wan, G. Xue, and A. Sen, *Entanglement Distribution in Satellite-based Dynamic Quantum Networks*, en, arXiv:2306.08894 [cs], Jun. 2023. doi: [10.48550/arXiv.2306.08894](https://doi.org/10.48550/arXiv.2306.08894). Accessed: Mar. 8, 2025. [Online]. Available: <http://arxiv.org/abs/2306.08894>.
- [56] H. J. Kimble, "The Quantum Internet," *Nature*, vol. 453, no. 7198, pp. 1023–1030, Jun. 2008, arXiv:0806.4195 [quant-ph], issn: 0028-0836, 1476-4687. doi: [10.1038/nature07127](https://doi.org/10.1038/nature07127). Accessed: Mar. 2, 2025. [Online]. Available: <http://arxiv.org/abs/0806.4195>.
- [57] A. S. Cacciapuoti, M. Caleffi, F. Tafuri, F. S. Cataliotti, S. Gherardini, and G. Bianchi, "Quantum Internet: Networking Challenges in Distributed Quantum Computing," *IEEE Network*, vol. 34, no. 1, pp. 137–143, Jan. 2020, arXiv:1810.08421 [quant-ph], issn: 0890-8044, 1558-156X. doi: [10.1109/MNET.001.1900092](https://doi.org/10.1109/MNET.001.1900092). Accessed: Mar. 17, 2025. [Online]. Available: <http://arxiv.org/abs/1810.08421>.
- [58] L. Bacciottini et al., *Leveraging Internet Principles to Build a Quantum Network*, arXiv:2410.08980 [quant-ph], Oct. 2024. doi: [10.48550/arXiv.2410.08980](https://doi.org/10.48550/arXiv.2410.08980). Accessed: Apr. 23, 2025. [Online]. Available: <http://arxiv.org/abs/2410.08980>.
- [59] R. Satoh et al., "QuISP: A Quantum Internet Simulation Package," en, in *2022 IEEE International Conference on Quantum Computing and Engineering (QCE)*, arXiv:2112.07093 [quant-ph], Sep. 2022, pp. 353–364. doi: [10.1109/QCE53715.2022.00056](https://doi.org/10.1109/QCE53715.2022.00056). Accessed: Mar. 9, 2025. [Online]. Available: <http://arxiv.org/abs/2112.07093>.
- [60] J. Yin et al., *Satellite-Based Entanglement Distribution Over 1200 kilometers*, arXiv:1707.01339 [quant-ph], Jul. 2017. doi: [10.48550/arXiv.1707.01339](https://doi.org/10.48550/arXiv.1707.01339). Accessed: Mar. 2, 2025. [Online]. Available: <http://arxiv.org/abs/1707.01339>.
- [61] C.-Y. Lu, Y. Cao, C.-Z. Peng, and J.-W. Pan, "Micius quantum experiments in space," en, *Rev. Mod. Phys.*, vol. 94, no. 3, p. 035 001, Jul. 2022, arXiv:2208.10236 [quant-ph], issn: 0034-6861, 1539-0756. doi: [10.1103/RevModPhys.94.035001](https://doi.org/10.1103/RevModPhys.94.035001). Accessed: Mar. 9, 2025. [Online]. Available: <http://arxiv.org/abs/2208.10236>.
- [62] M. Schlosshauer, *The quantum-to-classical transition and decoherence*, arXiv:1404.2635 [quant-ph], Nov. 2019. doi: [10.48550/arXiv.1404.2635](https://doi.org/10.48550/arXiv.1404.2635). Accessed: Mar. 3, 2025. [Online]. Available: <http://arxiv.org/abs/1404.2635>.

- [63] W.-Y. Sun et al., *Quantum coherence and entanglement under the influence of decoherence*, en, arXiv:2402.19055 [quant-ph], Feb. 2024. DOI: [10.48550/arXiv.2402.19055](https://doi.org/10.48550/arXiv.2402.19055). Accessed: Mar. 8, 2025. [Online]. Available: <http://arxiv.org/abs/2402.19055>.
- [64] A. S. Cacciapuoti, J. Illiano, M. Viscardi, and M. Caleffi, “Multipartite Entanglement Distribution in the Quantum Internet: Knowing When to Stop!” en, *IEEE Trans. Netw. Serv. Manage.*, vol. 21, no. 6, pp. 6041–6058, Dec. 2024, ISSN: 1932-4537, 2373-7379. DOI: [10.1109/TNSM.2024.3452326](https://doi.org/10.1109/TNSM.2024.3452326). Accessed: Mar. 11, 2025. [Online]. Available: <https://ieeexplore.ieee.org/document/10660502/>.
- [65] J. S. Sidhu, S. K. Joshi, M. Gundogan, T. Brougham, F. Basset, and D. K. Oi, “Advances in space quantum communications,” *Progress in Quantum Electronics*, vol. 73, p. 100 274, 2021.
- [66] P. Fittipaldi, A. Giovanidis, and F. Grosshans, “A linear algebraic framework for quantum internet dynamic scheduling,” in *2022 IEEE International Conference on Quantum Computing and Engineering (QCE)*, IEEE, 2022, pp. 447–453.
- [67] A. Williams, N. K. Panigrahy, A. McGregor, and D. Towsley, “Scalable scheduling policies for quantum satellite networks,” *arXiv preprint arXiv:2405.09464*, 2024.
- [68] A. Chang, Y. Wan, G. Xue, and A. Sen, “Entanglement distribution in satellite-based dynamic quantum networks,” *IEEE Network*, 2023.
- [69] A. Mukhopadhyay et al., *Study of different performance measures and their relations in satellite-based and terrestrial quantum communication. iet quan. commun.* 2 (4), 230–245 (2021).
- [70] G. Ni, L. Ho, and H. Claussen, “Adaptive optimization of latency and throughput with fidelity constraints in quantum networks using deep neural networks,” *arXiv preprint arXiv:2505.12459*, 2025.
- [71] H. Gu et al., *FENDI: Toward High-Fidelity Entanglement Distribution in the Quantum Internet*, arXiv:2301.08269 [cs], Oct. 2023. DOI: [10.48550/arXiv.2301.08269](https://doi.org/10.48550/arXiv.2301.08269). Accessed: Feb. 13, 2025. [Online]. Available: <http://arxiv.org/abs/2301.08269>.
- [72] L. Gyongyosi and S. Imre, “Topology adaption for the quantum internet,” *Quantum Information Processing*, vol. 17, no. 11, 2018.
- [73] T. Hu, J. Wu, and Q. Li, “Dynamic routing in space-ground integrated quantum networks,” in *MILCOM 2024-2024 IEEE Military Communications Conference (MILCOM)*, IEEE, 2024, pp. 1138–1143.
- [74] A. Sen, C. Sumnicht, S. Choudhuri, A. Chang, G. Xue, and Y. Want, “Quantum communication in 6g satellite networks: Entanglement distribution across changing topologies,” in *ICC 2024-IEEE International Conference on Communications*, IEEE, 2024, pp. 2446–2451.
- [75] M. U. A. Siddiqui, H. Abumarshoud, L. Bariah, S. Muhaidat, M. A. Imran, and L. Mohjazi, “Urllc in beyond 5g and 6g networks: An interference management perspective,” *IEEE Access*, vol. 11, pp. 54 639–54 663, 2023. DOI: [10.1109/ACCESS.2023.3282363](https://doi.org/10.1109/ACCESS.2023.3282363).
- [76] E. Paolini, G. Liva, and M. Chiani, “Coded slotted aloha: A graph-based method for uncoordinated multiple access,” *IEEE Transactions on Information Theory*, vol. 61, no. 12, pp. 6815–6832, Dec. 2015. DOI: [10.1109/TIT.2015.2492579](https://doi.org/10.1109/TIT.2015.2492579).

- [77] P. Raut, K. Singh, C.-P. Li, M.-S. Alouini, and W.-J. Huang, "Nonlinear eh-based uav-assisted fd iot networks: Infinite and finite blocklength analysis," *IEEE Internet of Things Journal*, vol. 8, no. 24, pp. 17 655–17 668, 2021. doi: [10.1109/JIOT.2021.3082102](https://doi.org/10.1109/JIOT.2021.3082102).
- [78] X. Shao, Z. Sun, M. Yang, S. Gu, and Q. Guo, "Noma-based irregular repetition slotted aloha for satellite networks," *IEEE Communications Letters*, vol. 23, no. 4, pp. 624–627, 2019. doi: [10.1109/LCOMM.2019.2900319](https://doi.org/10.1109/LCOMM.2019.2900319).
- [79] M. Kamel, W. Hamouda, and A. Youssef, "Uplink performance of noma-based combined htc and mtc in ultradense networks," *IEEE Internet of Things Journal*, vol. 7, no. 8, pp. 7319–7333, 2020. doi: [10.1109/JIOT.2020.2984805](https://doi.org/10.1109/JIOT.2020.2984805).
- [80] C. Xu et al., "Optimal status updates for minimizing age of correlated information in iot networks with energy harvesting sensors," *IEEE Transactions on Mobile Computing*, vol. 23, no. 6, pp. 6848–6864, 2024. doi: [10.1109/TMC.2023.3329170](https://doi.org/10.1109/TMC.2023.3329170).
- [81] C. H. Bennett and G. Brassard, "Quantum cryptography: Public key distribution and coin tossing," *Theoretical Computer Science*, vol. 560, pp. 7–11, Dec. 2014, arXiv:2003.06557 [quant-ph], issn: 03043975. doi: [10.1016/j.tcs.2014.05.025](https://doi.org/10.1016/j.tcs.2014.05.025). Accessed: Apr. 23, 2025. [Online]. Available: <http://arxiv.org/abs/2003.06557>.
- [82] C. Cicconetti, M. Conti, and A. Passarella, "Resource Allocation in Quantum Networks for Distributed Quantum Computing," in *2022 IEEE International Conference on Smart Computing (SMARTCOMP)*, arXiv:2203.05844 [quant-ph], Jun. 2022, pp. 124–132. doi: [10.1109/SMARTCOMP55677.2022.00032](https://doi.org/10.1109/SMARTCOMP55677.2022.00032). Accessed: Apr. 23, 2025. [Online]. Available: <http://arxiv.org/abs/2203.05844>.
- [83] Y. Xia, W. Li, W. Clark, D. Hart, Q. Zhuang, and Z. Zhang, "Demonstration of a Reconfigurable Entangled Radiofrequency-Photonic Sensor Network," *Phys. Rev. Lett.*, vol. 124, no. 15, p. 150 502, Apr. 2020, arXiv:1910.08825 [quant-ph], issn: 0031-9007, 1079-7114. doi: [10.1103/PhysRevLett.124.150502](https://doi.org/10.1103/PhysRevLett.124.150502). Accessed: Apr. 23, 2025. [Online]. Available: <http://arxiv.org/abs/1910.08825>.
- [84] L. d. F. d. Parny et al., "Satellite-based Quantum Information Networks: Use cases, Architecture, and Roadmap," *Commun Phys*, vol. 6, no. 1, p. 12, Jan. 2023, arXiv:2202.01817 [quant-ph], issn: 2399-3650. doi: [10.1038/s42005-022-01123-7](https://doi.org/10.1038/s42005-022-01123-7). Accessed: Feb. 12, 2025. [Online]. Available: <http://arxiv.org/abs/2202.01817>.
- [85] H.-J. Briegel, W. Dür, J. I. Cirac, and P. Zoller, *Quantum repeaters for communication*, arXiv:quant-ph/9803056, Mar. 1998. doi: [10.48550/arXiv.quant-ph/9803056](https://doi.org/10.48550/arXiv.quant-ph/9803056). Accessed: Mar. 20, 2025. [Online]. Available: <http://arxiv.org/abs/quant-ph/9803056>.
- [86] S. Muralidharan, L. Li, J. Kim, N. Lütkenhaus, M. D. Lukin, and L. Jiang, "Optimal architectures for long distance quantum communication," en, *Sci Rep*, vol. 6, no. 1, p. 20 463, Feb. 2016, issn: 2045-2322. doi: [10.1038/srep20463](https://doi.org/10.1038/srep20463). Accessed: Apr. 22, 2025. [Online]. Available: <https://www.nature.com/articles/srep20463>.
- [87] S.-K. Liao et al., "Satellite-to-ground quantum key distribution," *Nature*, vol. 549, no. 7670, pp. 43–47, Sep. 2017, arXiv:1707.00542 [quant-ph], issn: 0028-0836, 1476-4687. doi: [10.1038/nature23655](https://doi.org/10.1038/nature23655). Accessed: Mar. 2, 2025. [Online]. Available: <http://arxiv.org/abs/1707.00542>.
- [88] C. Erven et al., "Studying free-space transmission statistics and improving free-space quantum key distribution in the turbulent atmosphere," en, *New J. Phys.*, vol. 14, no. 12, p. 123 018, Dec. 2012, issn: 1367-2630. doi: [10.1088/1367-2630/14/12/123018](https://doi.org/10.1088/1367-2630/14/12/123018). Accessed: Mar. 8, 2025. [Online]. Available: <https://iopscience.iop.org/article/10.1088/1367-2630/14/12/123018>.

- [89] N. Schwaller, G. Park, R. Okamoto, and S. Takeuchi, “Optimizing the coupling efficiency of spontaneous parametric down-conversion photon pairs into single-mode fibers,” en, *Phys. Rev. A*, vol. 106, no. 4, p. 043 719, Oct. 2022, Number: 4, ISSN: 2469-9926, 2469-9934. DOI: [10.1103/PhysRevA.106.043719](https://doi.org/10.1103/PhysRevA.106.043719). Accessed: Feb. 8, 2025. [Online]. Available: <https://link.aps.org/doi/10.1103/PhysRevA.106.043719>.
- [90] P. Fittipaldi, K. Teramoto, N. Benchasattabuse, M. Hajdušek, R. V. Meter, and F. Grosshans, “Entanglement Swapping in Orbit: A Satellite Quantum Link Case Study,” en, in *2024 IEEE International Conference on Quantum Computing and Engineering (QCE)*, arXiv:2405.07589 [quant-ph], Sep. 2024, pp. 1924–1930. DOI: [10.1109/QCE60285.2024.00222](https://doi.org/10.1109/QCE60285.2024.00222). Accessed: Mar. 9, 2025. [Online]. Available: <http://arxiv.org/abs/2405.07589>.
- [91] C. Cabrillo, J. I. Cirac, P. Garcia-Fernandez, and P. Zoller, “Creation of entangled states of distant atoms by interference,” *Phys. Rev. A*, vol. 59, no. 2, pp. 1025–1033, Feb. 1999, arXiv:quant-ph/9810013, ISSN: 1050-2947, 1094-1622. DOI: [10.1103/PhysRevA.59.1025](https://doi.org/10.1103/PhysRevA.59.1025). Accessed: Mar. 17, 2025. [Online]. Available: <http://arxiv.org/abs/quant-ph/9810013>.
- [92] C. Ferrari and B. Braunecker, “Entanglement, which-way measurements, and a quantum erasure,” *American Journal of Physics*, vol. 78, no. 8, pp. 792–795, Aug. 2010, arXiv:0911.2072 [quant-ph], ISSN: 0002-9505, 1943-2909. DOI: [10.1119/1.3369921](https://doi.org/10.1119/1.3369921). Accessed: Mar. 17, 2025. [Online]. Available: <http://arxiv.org/abs/0911.2072>.
- [93] S. Welte, B. Hacker, S. Daiss, S. Ritter, and G. Rempe, “Photon-Mediated Quantum Gate between Two Trapped Neutral Atoms in an Optical Cavity,” *Phys. Rev. X*, vol. 8, no. 1, p. 011 018, Feb. 2018, arXiv:1801.05980 [quant-ph], ISSN: 2160-3308. DOI: [10.1103/PhysRevX.8.011018](https://doi.org/10.1103/PhysRevX.8.011018). Accessed: Mar. 17, 2025. [Online]. Available: <http://arxiv.org/abs/1801.05980>.
- [94] J. Illiano, M. Caleffi, A. Manzalini, and A. S. Cacciapuoti, “Quantum Internet protocol stack: A comprehensive survey,” en, *Computer Networks*, vol. 213, p. 109 092, Aug. 2022, ISSN: 13891286. DOI: [10.1016/j.comnet.2022.109092](https://doi.org/10.1016/j.comnet.2022.109092). Accessed: Mar. 9, 2025. [Online]. Available: <https://linkinghub.elsevier.com/retrieve/pii/S1389128622002250>.
- [95] C. Jones, D. Kim, M. T. Rakher, P. G. Kwiat, and T. D. Ladd, “Design and Analysis of Communication Protocols for Quantum Repeater Networks,” *New J. Phys.*, vol. 18, no. 8, p. 083 015, Aug. 2016, arXiv:1505.01536 [quant-ph], ISSN: 1367-2630. DOI: [10.1088/1367-2630/18/8/083015](https://doi.org/10.1088/1367-2630/18/8/083015). Accessed: Mar. 17, 2025. [Online]. Available: <http://arxiv.org/abs/1505.01536>.
- [96] A. S. Cacciapuoti, M. Caleffi, R. Van Meter, and L. Hanzo, “When Entanglement Meets Classical Communications: Quantum Teleportation for the Quantum Internet,” en, *IEEE Trans. Commun.*, vol. 68, no. 6, pp. 3808–3833, Jun. 2020, ISSN: 0090-6778, 1558-0857. DOI: [10.1109/TCOMM.2020.2978071](https://doi.org/10.1109/TCOMM.2020.2978071). Accessed: Mar. 17, 2025. [Online]. Available: <https://ieeexplore.ieee.org/document/9023997/>.
- [97] C. Qiao, Y. Zhao, G. Zhao, and H. Xu, “Quantum Data Networking for Distributed Quantum Computing: Opportunities and Challenges,” in *IEEE INFOCOM 2022 - IEEE Conference on Computer Communications Workshops (INFOCOM WKSHPS)*, May 2022, pp. 1–6. DOI: [10.1109/INFOCOMWKSHPS54753.2022.9798138](https://doi.org/10.1109/INFOCOMWKSHPS54753.2022.9798138). Accessed: Feb. 7, 2025. [Online]. Available: <https://ieeexplore.ieee.org/document/9798138/?arnumber=9798138>.

- [98] G. Iacovelli, F. Vista, N. Cordeschi, and L. A. Grieco, “A Probability-Based Optimization Approach for Entanglement Distribution and Source Position in Quantum Networks,” en, *IEEE J. Select. Areas Commun.*, vol. 42, no. 7, pp. 1738–1748, Jul. 2024, Number: 7, ISSN: 0733-8716, 1558-0008. DOI: [10.1109/JSAC.2024.3380084](https://doi.org/10.1109/JSAC.2024.3380084). Accessed: Feb. 7, 2025. [Online]. Available: <https://ieeexplore.ieee.org/document/10477494/>.
- [99] Z. Ji, P. Fan, and H. Zhang, *Entanglement swapping theory and beyond*, arXiv:2009.02555 [quant-ph], Feb. 2025. DOI: [10.48550/arXiv.2009.02555](https://doi.org/10.48550/arXiv.2009.02555). Accessed: Mar. 20, 2025. [Online]. Available: <http://arxiv.org/abs/2009.02555>.
- [100] P. Fittipaldi, A. Giovanidis, and F. Grosshans, *A Linear Algebraic Framework for Quantum Internet Dynamic Scheduling*, en, arXiv:2205.10000 [cs], Sep. 2022. DOI: [10.48550/arXiv.2205.10000](https://doi.org/10.48550/arXiv.2205.10000). Accessed: Mar. 10, 2025. [Online]. Available: <http://arxiv.org/abs/2205.10000>.
- [101] F. Dupuy, C. Goursaud, and F. Guillemin, “A Survey of Quantum Entanglement Routing Protocols—Challenges for Wide-Area Networks,” en, *Adv Quantum Tech*, vol. 6, no. 5, p. 2 200 180, May 2023, ISSN: 2511-9044, 2511-9044. DOI: [10.1002/qute.202200180](https://doi.org/10.1002/qute.202200180). Accessed: Mar. 15, 2025. [Online]. Available: <https://onlinelibrary.wiley.com/doi/10.1002/qute.202200180>.
- [102] S. Brand, T. Coopmans, and D. Elkouss, “Efficient computation of the waiting time and fidelity in quantum repeater chains,” *IEEE J. Select. Areas Commun.*, vol. 38, no. 3, pp. 619–639, Mar. 2020, arXiv:1912.07688 [quant-ph], ISSN: 0733-8716, 1558-0008. DOI: [10.1109/JSAC.2020.2969037](https://doi.org/10.1109/JSAC.2020.2969037). Accessed: Apr. 6, 2025. [Online]. Available: <http://arxiv.org/abs/1912.07688>.
- [103] R. Werner, *Quantum states with Einstein-Podolsky-Rosen correlations admitting a hidden-variable model* | *Phys. Rev. A*, May 1989. Accessed: Mar. 17, 2025. [Online]. Available: <https://journals.aps.org/pra/abstract/10.1103/PhysRevA.40.4277>.
- [104] J. Li et al., *Fidelity-Guarantee Entanglement Routing in Quantum Networks*, arXiv:2111.07764 [quant-ph], Jun. 2022. DOI: [10.48550/arXiv.2111.07764](https://doi.org/10.48550/arXiv.2111.07764). Accessed: Apr. 6, 2025. [Online]. Available: <http://arxiv.org/abs/2111.07764>.
- [105] S. Pouryousef, H. Shapourian, A. Shabani, R. Kompella, and D. Towsley, *Resource Allocation for Rate and Fidelity Maximization in Quantum Networks*, arXiv:2308.16264 [quant-ph] version: 2, Feb. 2024. DOI: [10.48550/arXiv.2308.16264](https://doi.org/10.48550/arXiv.2308.16264). Accessed: Mar. 16, 2025. [Online]. Available: <http://arxiv.org/abs/2308.16264>.
- [106] W. Dür, H.-J. Briegel, J. I. Cirac, and P. Zoller, “Quantum repeaters based on entanglement purification,” *Phys. Rev. A*, vol. 59, no. 1, pp. 169–181, Jan. 1999, arXiv:quant-ph/9808065, ISSN: 1050-2947, 1094-1622. DOI: [10.1103/PhysRevA.59.169](https://doi.org/10.1103/PhysRevA.59.169). Accessed: Mar. 5, 2025. [Online]. Available: <http://arxiv.org/abs/quant-ph/9808065>.
- [107] R. Van Meter, T. Ladd, W. Munro, and K. Nemoto, “System Design for a Long-Line Quantum Repeater,” en, *IEEE/ACM Trans. Networking*, vol. 17, no. 3, pp. 1002–1013, Jun. 2009, ISSN: 1063-6692, 1558-2566. DOI: [10.1109/TNET.2008.927260](https://doi.org/10.1109/TNET.2008.927260). Accessed: Mar. 10, 2025. [Online]. Available: <http://ieeexplore.ieee.org/document/4695947/>.

- [108] Y. Zhao, G. Zhao, and C. Qiao, “E2E Fidelity Aware Routing and Purification for Throughput Maximization in Quantum Networks,” en, in *IEEE INFOCOM 2022 - IEEE Conference on Computer Communications*, London, United Kingdom: IEEE, May 2022, pp. 480–489, ISBN: 978-1-6654-5822-1. DOI: [10.1109/INFOCOM48880.2022.9796814](https://doi.org/10.1109/INFOCOM48880.2022.9796814). Accessed: Feb. 13, 2025. [Online]. Available: <https://ieeexplore.ieee.org/document/9796814/>.
- [109] P. G. Kwiat, K. Mattle, H. Weinfurter, A. Zeilinger, A. V. Sergienko, and Y. Shih, “New High-Intensity Source of Polarization-Entangled Photon Pairs,” en, *Phys. Rev. Lett.*, vol. 75, no. 24, pp. 4337–4341, Dec. 1995, ISSN: 0031-9007, 1079-7114. DOI: [10.1103/PhysRevLett.75.4337](https://doi.org/10.1103/PhysRevLett.75.4337). Accessed: Mar. 17, 2025. [Online]. Available: <https://link.aps.org/doi/10.1103/PhysRevLett.75.4337>.
- [110] K. Chakraborty, F. Rozpedek, A. Dahlberg, and S. Wehner, *Distributed Routing in a Quantum Internet*, arXiv:1907.11630 [quant-ph], Jul. 2019. DOI: [10.48550/arXiv.1907.11630](https://doi.org/10.48550/arXiv.1907.11630). Accessed: Mar. 5, 2025. [Online]. Available: <http://arxiv.org/abs/1907.11630>.
- [111] M. Afzelius, N. Gisin, and H. de Riedmatten, “Quantum memory for photons,” *Physics Today*, vol. 68, no. 12, pp. 42–47, Dec. 2015, eprint: https://pubs.aip.org/physicstoday/article-pdf/68/12/42/10100606/42_1_online.pdf, ISSN: 0031-9228. DOI: [10.1063/PT.3.3021](https://doi.org/10.1063/PT.3.3021). [Online]. Available: <https://doi.org/10.1063/PT.3.3021>.
- [112] J.-P. Bourgoin et al., “A comprehensive design and performance analysis of LEO satellite quantum communication,” en, *New J. Phys.*, vol. 15, no. 2, p. 023 006, Feb. 2013, arXiv:1211.2733 [quant-ph], ISSN: 1367-2630. DOI: [10.1088/1367-2630/15/2/023006](https://doi.org/10.1088/1367-2630/15/2/023006). Accessed: Mar. 8, 2025. [Online]. Available: <http://arxiv.org/abs/1211.2733>.
- [113] M. Victora, S. Tserkis, S. Krastanov, A. S. De La Cerda, S. Willis, and P. Narang, “Entanglement purification on quantum networks,” en, *Phys. Rev. Research*, vol. 5, no. 3, p. 033 171, Sep. 2023, ISSN: 2643-1564. DOI: [10.1103/PhysRevResearch.5.033171](https://doi.org/10.1103/PhysRevResearch.5.033171). Accessed: Mar. 8, 2025. [Online]. Available: <https://link.aps.org/doi/10.1103/PhysRevResearch.5.033171>.
- [114] C. Wu, S. Han, Q. Chen, Y. Wang, W. Meng, and A. Benslimane, *Enhancing LEO Mega-Constellations with Inter-Satellite Links: Vision and Challenges*, en, arXiv:2406.05078 [cs], Jun. 2024. DOI: [10.48550/arXiv.2406.05078](https://doi.org/10.48550/arXiv.2406.05078). Accessed: Mar. 8, 2025. [Online]. Available: <http://arxiv.org/abs/2406.05078>.
- [115] J. A. Slater et al., “A microstructured fiber source of photon pairs at widely separated wavelengths,” *Opt. Lett.*, vol. 35, no. 4, p. 499, Feb. 2010, arXiv:0908.3516 [quant-ph], ISSN: 0146-9592, 1539-4794. DOI: [10.1364/OL.35.000499](https://doi.org/10.1364/OL.35.000499). Accessed: Mar. 5, 2025. [Online]. Available: <http://arxiv.org/abs/0908.3516>.